# Combined Impact and Fatigue Loading in CFRP

## Effects of the timing of an impact event during cyclic loading of composite aircraft structures

C.C.J. van Diën

Technische Universiteit Delft

TU Delft

# Combined Impact and Fatigue Loading in CFRP

## Effects of the timing of an impact event during cyclic loading of composite aircraft structures

by

C.C.J. van Diën

to obtain the degree of Master of Science

at the Delft University of Technology,

to be defended on Wednesday September 30, 2020 at 9:30 AM.

| | | |
|---|---|---|
| Student number: | 4217667 | |
| Project duration: | May 2019 – September 2020 | |
| Thesis committee: | Dr. C.D. Rans, | TU Delft, Chairholder |
| | Dr. D. Zarouchas, | TU Delft, Supervisor |
| | Prof. Dr. C. Kassapoglou | TU Delft |
| | Dr. J.A. Pascoe, | TU Delft |

An electronic version of this thesis is available at http://repository.tudelft.nl/.

TU Delft

# Acknowledgements

This thesis concludes my time at the faculty of Aerospace Engineering at Delft University of Technology. The individual work style that a master's thesis requires does not come naturally to me, and without the help of the following people I would never have arrived at this point.

First and foremost, I would like to thank my supervisor Dimitrios Zarouchas who enthused me to investigate the 'impact of impact'. The frequent meetings in combination with his down to earth personality were often instrumental in pointing me in the right direction whenever I wavered off.

I would like to extend my thanks to the rest of the research group, in particular Nikos Eleftheroglou for laying the groundwork for my test setup, Agnes Broer-Reinoso Rondinel for explaining the acoustic emission equipment and Milad Saeedifar for assisting me with C-scanning and interpreting the acoustic emission data.

Furthermore, I am thankful to the technicians of the DASML lab, nearly all of whom have helped me at some point. Especially Gertjan and Dave could see me coming from a mile away when I inevitably ran into yet another 'small' problem. Without their help, I would undoubtedly still be in the lab by now.

On a more personal note, I am grateful to my parents and brother, without whose unconditional support this would have been a much more difficult endeavour. In addition, I would like to thank my friends and office buddies that have helped me to stay motivated with interesting discussions, some well-needed venting and coffee breaks that could undeniably have been shorter. Due to the unfortunate circumstances surrounding covid-19, this function has shifted towards my housemates, whom I must thank as well.

*C.C.J. van Diën*
*Delft, September 2020*

# Summary

There has been a consistent and growing trend in the aviation industry over the past decades to increase the use of fibre-reinforced composite materials in aircraft structures. While providing great benefits in terms of weight reduction, their complex damage mechanisms require a shift in design philosophy with respect to metals. Learning more about the effects of combined loading scenarios on such structures is invaluable for effective design, testing and certification practices. Moreover, such knowledge helps the design and implementation of structural health monitoring (SHM) systems that show great potential for streamlining maintenance work on aircraft.

The aim of this thesis is to investigate the effects of an impact event during cyclic loading of a carbon fibre reinforced polymer (CFRP) structure. A literature study was performed first to provide the necessary background knowledge on the mechanical behaviour of composite materials, as well as to show the wider context within SHM applications. The main work consisted of an experimental testing campaign where open-hole CFRP specimens were tested in tension-tension fatigue with constant amplitude loading. Specimens were impacted in-situ during a short interruption of the fatigue program. A combination of digital image correlation (DIC) and acoustic emission (AE) measurement setups were used to accurately measure the material response and damage patterns. In addition, ultrasonic C-scanning was used on specific samples to inspect any delaminated areas.

The results indicate that while an impact causes the total amount of damage to increase as one would expect, it does not necessarily increase the damage level in the critical area where final fracture occurs. A dependence on the moment of impact was found, where an impact before fatigue initiated damage which then grew under cyclic loading until final failure. In contrast, impacting specimens after various amounts of fatigue damage were already present in the material had no effect on this critical damage accumulation. In these cases, the fatigue damage along the critical path increased steadily as if no impact had occurred.

It should be pointed out that due to the high scatter observed, it would be wise to solidify some of the conclusions with further, similar testing. In addition, the conclusions are only directly applicable to the tested structure and loading scenario. Testing a wider range of structures and loading scenarios with different measurement techniques will provide more generalised conclusions on the effects of combined loading on composite materials.

# Contents

# Nomenclature

## Abbreviations

| | |
|---|---|
| ANOVA | Analysis of variance |
| BVID | Barely visible impact damage |
| CAI | Compression after impact |
| CBM | Condition based maintenance |
| CFRP | Carbon fibre reinforced polymer |
| DIC | Digital Image Correlation |
| FAI | Fatigue after impact |
| FBG | Fibre Bragg grating |
| GFRP | Glass fibre reinforced polymer |
| LVI | Low velocity impact |
| NDI | Non destructive inspection |
| PW | Plain weave |
| PZT | Piezoelectric |
| UD | Unidirectional |
| UTS | Ultimate tensile strength |
| QI | Quasi-isotropic |

## Symbols

| | | |
|---|---|---|
| a | Crack length | $m$ |
| E | Energy | $J$ |
| E | Young's modulus | $N/m^2$ |
| m | Mass | $kg$ |
| N | Number of fatigue cycles | - |
| v | Velocity | $m/s$ |
| $\epsilon$ | Strain | - |
| $\nu$ | Poisson's ratio | - |
| $\sigma$ | Stress | $N/m^2$ |

# List of Figures

# List of Tables

# 1

# Introduction

In the world of aviation, regular scheduled inspections of load-carrying systems are one of the key facets that keep aircraft operations safe throughout the life of an aircraft without the need for overly conservative and heavy structures. Current structural damage inspection methods are labour intensive and account for a significant fraction of the operating cost of commercial aircraft. Structural health monitoring (SHM) during aircraft operations shows potential for reducing these costs significantly, mainly by optimising maintenance scheduling. Designing reliable SHM systems is difficult, especially for use with fibre-reinforced materials. Their high strength-to-weight and stiffness-to-weight ratios make for a lightweight alternative to traditional metallic structures. Because of this, the use of these materials has increased steadily, with some of the newest generations of passenger aircraft having over half of their structural weight made from carbon fibre reinforced polymers (CFRP) and glass fibre reinforced polymers (GFRP). Their anisotropic behaviour and variety of failure mechanisms foster complex and stochastic damage patterns. Due to their distinct nature, a different design and damage tolerance philosophy has to be taken into account when replacing traditional aerospace aluminium alloys.

While metals are typically more prone to fatigue, one should avoid the dangerous assumption that fibre-reinforced composite materials do not suffer from fatigue at all. The response to cyclic loading is very different, where metallic materials are typically prone to large numbers of low-stress cycles that cause consistent crack growth. A few high-stress cycles may even retard damage growth due to local yielding at the crack tip, causing some residual compressive stress. Composite materials are not so susceptible to such low-stress loads, but instead show more stochastic damage formation under higher stresses [1]. Instead of the formation of a macro-level crack, several different damage mechanisms make up the total damage state. Another structural health concern for any aircraft is foreign object impact events. Impacts can range from a local and high-energy event such as a bird strike to distributed low-energy events, for instance during a hail storm. Unlike metallic structures however, composites often do not reveal any damage present. Incidents such as accidental tool drops during maintenance can create delaminations and cracks that are invisible to the naked eye from the outside of the structure. In order to deal with this, a limit case is often taken into account, where a structure is designed to be able to sustain its loads with the presence of barely visible impact damage (BVID). During operation of any aircraft, a structure will need to be able to cope with a combination circumstances that can reduce its structural integrity: static or fatigue loads, impact events, corrosion or thermal stresses to name a few.

The importance of investigating the effects of such detrimental phenomena is evident. In addition, combinations of these phenomena can amplify the structural degradation. Extensive research has therefore been performed on for example compression after impact or fatigue after impact situations on composite materials. No literature however was found on the effects of impact events during fatigue loading. The current research focuses on one type of loading discretely after another. This neglects for example the effects that any prior fatigue damage has on the damage response of an impact event. A projectile with a certain energy that would normally create BVID may create a different damage state

with other damage already present. By learning more about combined loading scenarios, a part of this knowledge gap is filled and better structural designs and maintenance practices may be developed. Moreover, these insights are useful for the progression towards integrated SHM systems.

## 1.1. Research Purpose

Narrowing down the broad problem description above, the purpose of this thesis project is to experimentally investigate the effects of combined impact and fatigue loading on carbon fibre reinforced polymer structures. The main research question is as follows:

**What are the effects of the timing of an impact event on the fatigue life and damage patterns in a CFRP structure?**

The following subquestions are defined to help answer the main question:

1. How does the structure respond to pure cyclic loading?
2. How does the structure respond to pure impact?
3. What is the effect of interrupting a fatigue test?
4. What is the effect of pre-existing fatigue damage on the damage caused by impact?
5. How does the structure respond differently with and without impact damage?

In order to answer the main question and its subquestions, an experimental testing campaign was set up. A mechanical testing machine was used for cyclic loading, with a gas gun positioned next to it so that specimens could be impacted in-situ. Digital image correlation (DIC) was used to track the strain response of each sample during testing, which was also used as a criterion to decide the moment of impact. In addition, acoustic emission (AE) measurements were performed to gain additional knowledge on damage accumulation during testing. Acoustic emission analysis has been shown to be a powerful tool with potential to be applied in SHM applications in aircraft. Some tests were not run until failure in order to be inspected using ultrasonic C-scanning to see any delaminated areas.

## 1.2. Document Structure

In order to provide the theoretical background necessary for designing the test campaign and answering the research questions, a literature study was performed. Chapter 2 presents literature on fibre reinforced polymers. Specifically, cyclic loading, impact, combined loading and the corresponding damage mechanisms are explored. To provide a broader context for this research, some background on SHM is provided in chapter 3. Various measurement techniques are presented there as well. The methodology of the experimental campaign is described in chapter 4, after which the gathered results are shown and discussed in chapter 5. Finally, the conclusions and recommendations are presented in chapters 6 and 7 respectively.

# 2

# Damage in Fibre Reinforced Composites

Structures made from fibre-reinforced composite materials have very different damage mechanisms than those made from traditional metals. A large disadvantage of these materials is that any damage may not be as visible as in metals, in the form of e.g. dents or cracks. Overdesigning a structure to the point that no damage is reasonably expected to occur would negate the potential weight benefit that composite materials have to offer. Much research has therefore been performed towards understanding the damage response of composite materials to various loading scenarios. Airworthiness regulations state that a structure containing barely visible impact damage (BVID) must still be able to sustain the loads seen during the rest of the aircraft life [2]. By definition, BVID is hard to detect visually and therefore must be expected to stay unrepaired.

Vlot has researched repair procedures on the primary structures of Boeing 747 fuselages [3]. In total, 71 fuselages with an average life of 29500 flying hours were documented. Figure 2.1 shows the repair locations of damages due to fatigue and impact, respectively. It can be seen that repairs are not uncommon, with a total number of 396 repairs on fatigue cracks, and 90 repairs on impact damage. Some locations, especially around doors and hatches, are especially prone to both types of damage, highlighting the importance of knowing what happens during combined damage scenarios.

AMC 20-29 (acceptable means of compliance) is a document by the European Union Aviation Safety Agency (EASA) covering compliance guidelines to aircraft certification specifications [2]. It specifically advises on compliance to CS-23, CS-25, CS-27 and CS-29 regarding composite aircraft structures. It specifies five different types of damage in aircraft structures:

- Category 1 damage includes BVID, and it should be proven that a structure is able to sustain its ultimate load capability throughout its life.
- Category 2 damage includes VID (visible impact damage) and should be detectable during scheduled inspections. It should be proven that a structure containing such a damage is able to sustain limit load throughout an inspection interval.
- Category 3 damage is visible enough to be detected within a few flights, and should be repaired immediately. A structure with category 3 damage should be able to sustain limit load until spotted.
- Category 4 damage is obvious and discrete by nature, such as a tyre burst, rotor burst or bird strike. It should be proven that structures containing this kind of serious damage shall be able to sustain flight loads for the remainder of the flight, after which an immediate repair should be carried out.

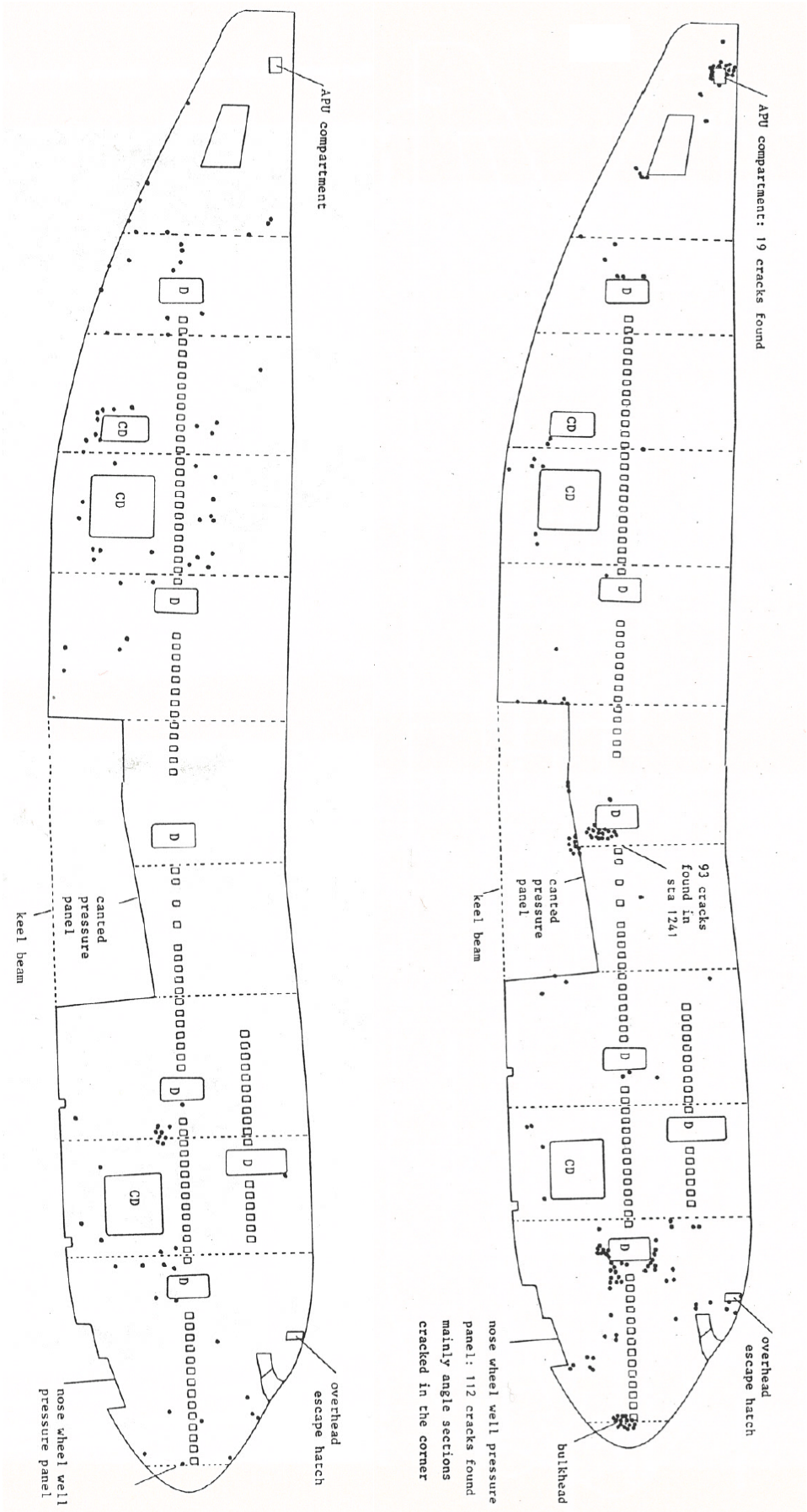


Figure 2.1: Fatigue (top) and impact (bottom) locations on a Boeing 747 fuselage [3]

- Category 5 damage covers severe damages that are not accounted for in design. Such a damage requires immediate reporting and damage characterization before repair.

In order to show that structures can sustain their required loads after damage, fatigue tests should be performed. Such fatigue tests are especially important for category 1 and 2 types of damage, since they need to sustain their loads for a prolonged period of time. Aside from the static and fatigue loads, the AMC document states that stiffness properties should not change significantly during fatigue testing. Since crack growth in composites is less predictable than in metals, a threshold approach is often adopted instead of a 'slow-growth' approach as typically used with metals [4]. This means that the regulations put emphasis on a structure being able to sustain loads after damage, without looking into how the damage increases over time. In addition to this, AMC 20-29 covers fatigue loading a structure with discrete impact damage, but it does not discuss other combined loading scenarios, for example an impact occurrence when fatigue damage is already present.

It is clear that there is a lack of knowledge of damage progression in composites in general, and damage under combined loading in specific. With more understanding of the effect of combined loadings on composite materials and structures, it is likely that the regulations can be made safer and more effective. In an attempt to start filling a part of this knowledge gap, this research focuses on tension-tension fatigue in combination with a single impact. Many areas on an aircraft that are primarily loaded in tension are also susceptible to impacts. For example, a wing's lower skin panel can be hit by runway debris during take-off or landing, or a tension-loaded fuselage section can be hit by hailstones or ground handling equipment.

## 2.1. Fatigue in Composites

Fatigue in metals is well researched. Several aircraft disasters in the second half of the 20th century highlighted the need for better understanding of this phenomenon [5]. After the introduction of composite materials, it was quickly evident that these materials had the potential to make aircraft much lighter and therefore cheaper to operate. The large downside - aside from their high cost - was that their damage mechanisms were largely unknown. Up to this day there is still much to learn on fatigue in fibre-reinforced polymers and fibre-metal laminates [6], [7].

Due to the highly anisotropic nature of fibre reinforced polymers (FRPs), their damage mechanisms are complex. Damage accumulation and failure are highly dependent on factors like the constituent materials, fibre directions, fibre volume fraction, stacking order and curing process. Hashin and Rotem already started researching fatigue effects in FRPs in the 1970s [8]. Their tension-tension fatigue tests proved the strong sensitivity of unidirectional FRPs to fibre alignment. A misalignment of only 5 degrees from the direction of applied load lead to a factor 3 decrease in both static and fatigue strength.

Open-hole specimens are often used for several reasons. First of all, some level of realism is added, since structures in real life are never uninterrupted. To put it differently, an aircraft is full of holes for rivets, bolts and cutouts. Secondly, having a hole or notch enforces a probable damage initiation location, making it easier to set up the measuring equipment. Kortschot and Beaumont [9], [10] were early in their research towards the effect of notches in composite specimens. They set up a model that is able to predict the strength and damage growth rate of cross-ply CFRP specimens with two sharp notches, without the need for empirical parameters. Spearing and Beaumont [11] specifically studied damage due to cyclic fatigue in notched specimens. Both cross-ply and quasi-isotropic (QI) CFRP specimens were tested in tension-tension fatigue with a frequency of 10 Hz and a stress ratio of 0.1. It was observed that the split length in the 0°plies provided a key damage parameter. As could be expected, a higher peak stress and lower stress ratio lead to faster damage growth. Moreover, stacking multiple plies with the same fibre orientation next to each other decreased fatigue performance as damage coalescence becomes easier. Finally, residual tensile strength increased while the stiffness decreased as the number of fatigue cycles increased. The stiffness decrease was dependent on the peak stress level, as shown in figure 2.2.

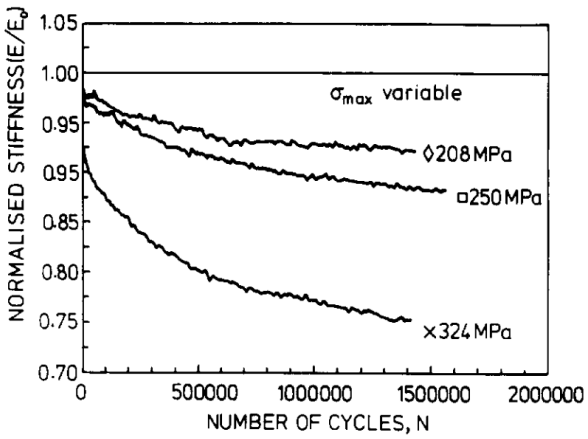


Figure 2.2: Stiffness decrease during fatigue of $(90/0)_s$ specimens [11]

Quasi-static tensile testing sheds some light on the various damage mechanisms and how they interact and propagate. Green and Hallet et al. have studied the effect of scaling and ply stacking sequence on tensile failure of open-hole CFRP specimens with a quasi-isotropic layup [12] [13]. Large differences in ultimate strength have been found along with three distinct failure modes: brittle, pull-out or delamination failure. See Figure 2.3 for an example of each mode. Failure was defined as a minimum load drop of 5% in the load-displacement curve. Despite the differences in catastrophic failure, the sub-critical damage preceding it was very similar. Damage initiates at the hole edge in the form of delaminations and splitting of the off-axis plies, then starts to coalesce and spread towards the sides of the specimen, until finally the damage propagates along the full specimen length.

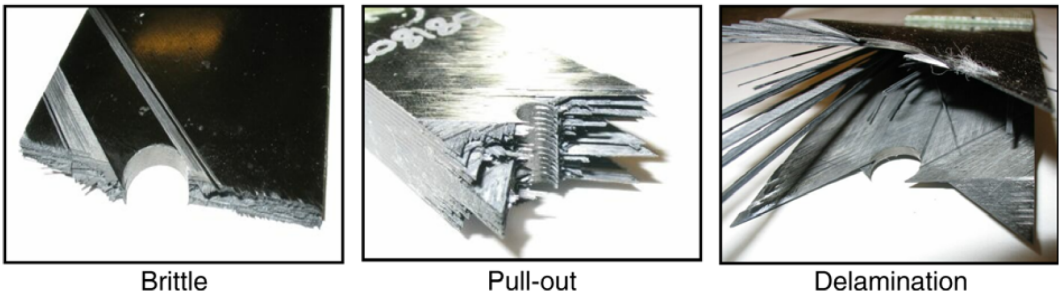


Figure 2.3: Three different failure modes of open-hole CFRP specimens in tension [13]

Broughton et al. have studied open-hole tension-tension fatigue on GFRP laminates [14]. A QI layup of E-glass epoxy prepreg plies has been tested with a frequency of 5 Hz at different fatigue loading spectra. With maximum amplitudes at 40%, 55% and 70% of the ultimate tensile strength (UTS) and the stress ratio R = 0.1, the damage sequences are largely similar to that of the quasi-static tests discussed above. Digital Image Correlation (DIC) is used as the main technique to measure strain response, with some other methods used to correlate the measurements. Chapter 3 elaborates further on the DIC technique. With strain values measured at several points near the hole, a certain stiffness response can be seen. It is noted that such a local stiffness is much more sensitive to damage growth than the global stiffness. During testing, fast initial stiffness loss caused by matrix cracking in the 90°and 45°plies was seen, followed by a more gradual loss in stiffness due to further cracking in plies (including splitting of the 0°plies) and delaminations between the 45°and 90°layers. Finally, catastrophic failure is preceded by a rapid final decrease in stiffness caused by damage coalescence, fibre fracture and pull-out. The final stiffness before ultimate failure agrees very well with the theoretical stiffness value as calculated using classical laminate theory, assuming all but the 0°plies have failed. Research by the same authors on specimens without a hole showed the same agreement. They also found an empirical relation that seems to work surprisingly well in predicting the final strain based on initial strains, or applied stresses

and initial stiffness (equation 2.1). Apparently, the axial strain right before failure is roughly equal to the mean initial strain plus the maximum initial strain. It can be concluded that the stiffness response of the fatigue specimens reflect certain damage events well, and the normalised measured stiffness values exhibit less scatter than the fatigue lives. It is therefore of vital importance to accurately track the strain response during testing, which can then be converted to stiffness. Note that glass fibre was used in this research, so the phenomena observed will not necessarily be the same as when a carbon fibre composite is tested.

$$\varepsilon^f_{max} \approx \varepsilon^i_{max} + \varepsilon^i_{mean} \approx \frac{\sigma_{max} + \sigma_{mean}}{E_0} \tag{2.1}$$

Fatigue testing work on open-hole CFRP specimens with a QI layup performed by Nixon-Pearson et al. has shown similar trends [6]. The tests were performed at 40%, 50%, 60%, 70% and 80% of the failure load. Failure in static testing was defined as the point where a sudden, sharp load drop of at least 5% occurred. This happened due to extensive delamination between the -45°and 0°layers, and even though the 0°fibres were able to continue carrying load, the structural integrity is deemed to be lost. Failure during fatigue testing was defined as 15% loss in stiffness. In order to calculate this stiffness, the strain was measured over a length of 50 mm symmetric about the hole using an extensometer. Figure 2.4 shows the normalised stiffness degradation at different maximum amplitudes as percentage of the static failure load, which is referred to as severity. In this testing campaign, defining failure as a 15% stiffness loss makes sense as the stiffness drop was very sudden after that point, after which only the 0°fibres were intact. Some specimens were stopped after various losses in stiffness in order to make X-ray CT scans. This sheds light on the damage mechanisms and their order of occurrence. Initially, isolated splits in the off-axis plies occur around the hole edge. Then, splits join up to form triangular delamination areas between the 90°and 45°layers. These delaminations step down through the matrix splits until reaching the 0°plies. The damages in this case start at the outer surfaces and move inwards, as the stacking sequence is $[45_2/90_2/-45_2/0_2]_s$. After the damages have reached the 0°layers, the delamination between the -45°and 0°plies run longitudinally towards the end tabs, at which point the large drop in stiffness occurs. At this point there is also longitudinal splitting in the 0°ply, but the fibres still sustain load and can be load cycled for quite a while before complete separation (fibre fracture) occurs.

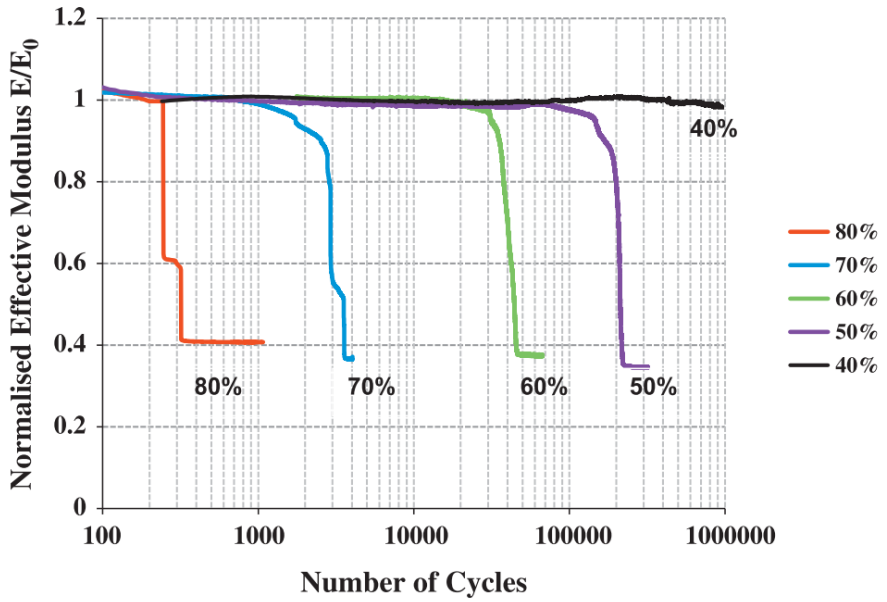


Figure 2.4: Normalised stiffness degradation at different severity percentages [6]

Research by Kalyanasundaram on tension-tension fatigue in CFRP with a fiber laser machined hole provided similar conclusions to stiffness loss and damage modes [15]. It was also concluded that the damage growth in specimens that have been fibre laser machined was similar to that in conventionally machined specimens, the paper is therefore deemed relevant in comparison to the other literature discussed. The specimens had a quasi-isotropic layup and several severities were tested, all with a stress ratio of R = 0.1. Tests were conducted with peak stresses of 70%, 50% and 30% of UTS (ultimate tensile strength), and failure was considered as either complete separation of a specimen, or a loss in stiffness of at least 15%. The coupons tested at 70% severity were able to sustain between 4000 and 7500 cycles before 15% stiffness loss occurred, and the tests at 50% severity were stopped between 70'000 and 80'000 cycles. The 30% severity tests however were all stopped at $10^6$ cycles because hardly any loss in stiffness was observed. The graph showing stiffness versus number of cycles shows very similar trends as in Figure 2.4. The main failure modes were similar to that in other research, with off-axis matrix cracking occurring first, followed by delaminations and longitudinal splitting.

Similar open-hole tension-tension fatigue testing work was performed by Aidi et al [16]. With a stress ratio of R=0.1 and a frequency of f=10Hz, carbon fibre/epoxy specimens were tested with maximum amplitude values of 65%, 70%, 75% and 80% of the nominal static failure load. The tests were stopped either upon complete failure (separation) of the samples or after $10^6$ cycles. On a linear scale, the stiffness reduction was linear with number of cycles, until very close to failure (Figure 2.5. Stiffness was measured using DIC, as well as with an extensometer with a gauge length of 25 mm, placed symmetrically across the hole. The samples tested at 80% severity had a typical fatigue life of about 25'000 cycles, and fatigue life steadily increased with decreasing severity as expected, with all the 65% severity specimens being runouts. Significant stiffness reduction had occurred by then, indicating the presence of serious damage in the material. Less scatter would be observed if the 15% failure loss criterion would have been used to define failure, but the authors deem this an arbitrary threshold, as the specimens at this point still exhibit significant load carrying capability. As a matter of fact, the specimens show an increase in static tensile strength through much of their fatigue lifetime. Failure in the specimens started as transverse matrix cracking in the 90°plies, sometimes in combination with some 45°cracking. After this, (hole) edge delaminations initiate in combination with axial splitting in the 0°layers. The strain measurements were performed using DIC and an extensometer, and it was concluded that DIC is a good tool to assess and track the damage accumulation in fatigue testing. In addition, X-ray CT (computed tomography) scans were able to accurately assess matrix cracking and delaminations per ply in a given specimen. Frequency response measurements were taken as well, which were able to provide some quantitative indication of the damage state through changing natural frequencies throughout testing. No qualitative conclusions can be drawn though, as the frequency response does not say anything about the type or location of damage present.

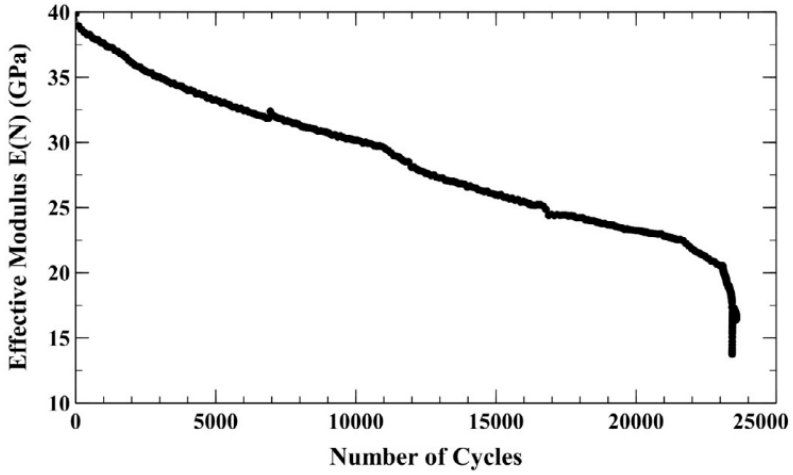


Figure 2.5: Typical reduction in effective modulus over fatigue lifetime [16]

Research was performed by Amaral et al. into strain energy release rates (SERR) of UD carbon fibre composite specimens tested in mode I fracture. Double cantilevered beams were used for this. They have shown that the faster the crack growth per fatigue cycle ($da/dN$), the higher the energy dissipation per cycle ($dU/dN$). This increase in energy released per cycle is reflected in the damage mechanisms at small scale; from cohesive fracture creating smooth fracture surfaces towards damage mechanisms such as fibre breakage that release more energy and leave behind a rougher surface. Figure 2.6 shows a clear representation of this. What this shows is that in high cycle fatigue at low loads, less energy is required for the same amount of crack growth than in high load fatigue or even quasi-static loading. This may be explained by the constant change in delamination or crack fronts under high cycle fatigue loading, so that it always follows the path of least resistance.

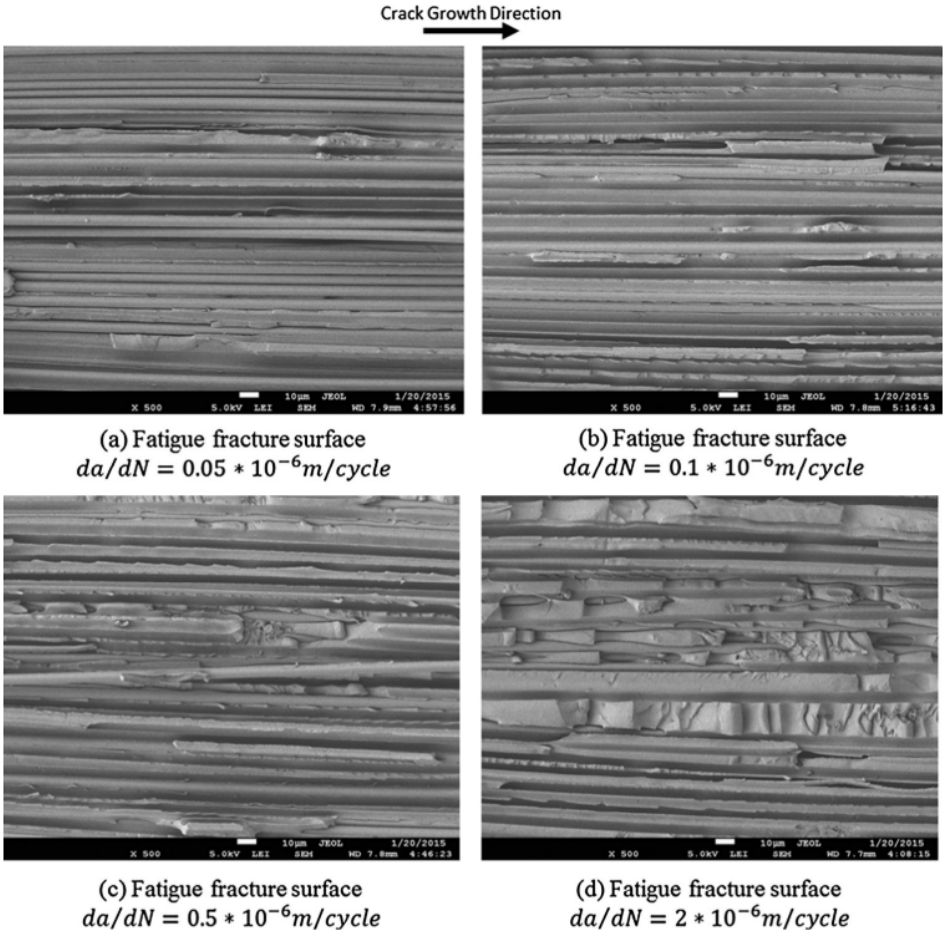


Figure 2.6: Fracture surfaces for various crack growth rates [17]

The nature of fatigue testing, especially when using composite materials, can make it difficult to obtain good data. For example, Alderliesten et al. discuss intrinsic and extrinsic scatter and the detrimental effect on high quality test data due to the latter [7]. Examples of intrinsic scatter are slight production process variability and inhomogeneous material morphology. These should not be overlooked, and effort should be taken to have them reflect a real-life manufacturing quality, not to exclude them completely. Extrinsic scatter however are a result of variations in for example the measurement set-up, operator experience and specimen cutting quality. Such factors should be excluded as much as possible, since they introduce variation and stochasticity in the test data without truly reflecting the structure or material tested. The effect of testing frequency is also an important consideration. Fatigue testing can be a time consuming process, so using a higher cyclic frequency can be helpful to make more efficient use of machine and operator time. However, a high frequency causes heating in the material, which is usually unwanted. Heating is caused by a combination of viscoelastic effects of the matrix in

combination with friction effects between damages. Alderliesten [7] recommends using a frequency between 1 and 10 Hz and monitoring the surface temperature during testing. A frequency of 5 Hz is often used, for example by Broughton [14] and Nixon-pearson [6]. Some researchers opt to test with 10 Hz, such as Aidi [16] and Eleftheroglou [18]. A third challenge is the choice of testing parameters. Aside from testing frequency discussed above, a stress ratio and peak stress value should be chosen such that the testing time stays within reasonable limits. A low stress ratio in tension-tension fatigue is found to cause faster damage growth. However, a value of R=0 may create unwanted compression effects at the valleys of the loading cycle. This is why R=0.1 is often chosen. A peak stress is usually chosen to be more than 50% of the UTS. Using a high value such as 90% of the UTS, as used by Eleftheroglou [18], causes damage in the form of matrix cracking to occur very quickly, after which it still takes a long time for the specimens to fail completely. It is likely that after only several cycles, all but the 0°plies will be seriously damaged and hardly carry any load anymore. When looking into the damage mechanisms during fatigue testing, it is likely that using a severity of betwen 60% and 90% creates the optimum balance between gradual damage accumulation and testing time.

## 2.2. Impact in Composites

Impact damage can have many different causes, including tool drops during maintenance work, hail, runway debris hitting the aircraft during take off or landing, collision with handling equipment on the ground and bird strikes. Four properties relating to impact damage can be distinguished [3].

- Damage resistance: the ability of a material to resist damage
- Damage tolerance: the ability of a material to function with damage present
- Inspectability: the ease of observing damage
- Repairability: the ease of repairing a structure after damage

The damage tolerance of a material is defined as the ability of a structure to still perform its function - usually strength or stiffness wise - after for example an impact occurrence. A schematic visualisation of the relation between the damage size and residual strength over time is shown in Figure 2.7. Damage due to impact is one of of the main limitations on the use of composite materials in aviation [19], [20]. Different severities of impact can be discerned, often based on the velocity of the impactor. Low velocity impact (LVI) is typically in the order of 10 m/s, with energies of up to several tens of joules [3], [20]. Medium velocities occur for example in case of a bird strike, with velocities of around 100-150 m/s. Ballistic or high velocity can be important for military aircraft, where projectiles have a low weight but velocities of 300-2000 m/s, thus having energy levels of 10-20 kJ [4]. Incidents such as bird strikes and ballistic impacts pose an immediate danger due to their relatively high mass and/or high speeds, thus having a high impact energy. However, the damage that such an impact creates is easily visible once the aircraft is on the ground, so it can be repaired quickly. The most frequent impacts occur at low speeds, during which BVID can develop. The danger here is not that a large amount of damage is created during the event, but the fact that it will go unnoticed because the damage state is hidden. The mechanical properties of the structures can be severely impaired at this point, both in terms of static and fatigue strength.

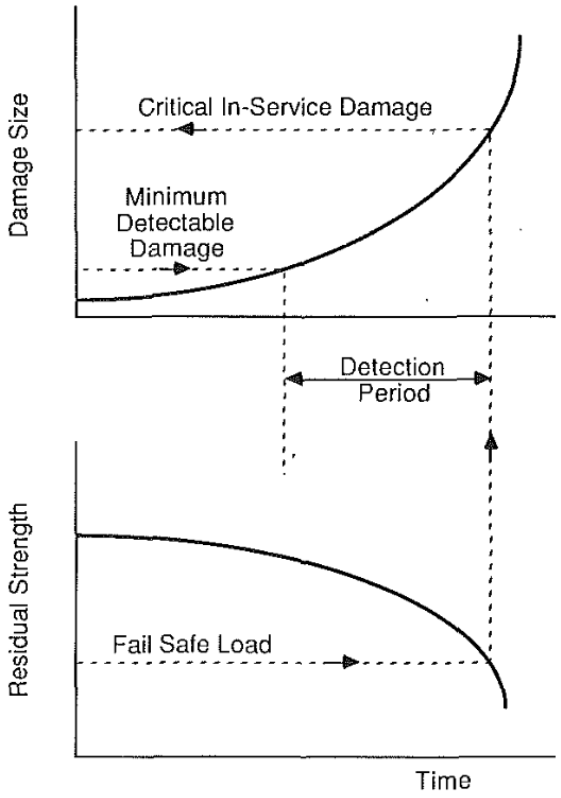


Figure 2.7: Relation between damage size and structural integrity [19]

Although there is much discussion on impact velocities, there can be a wide variety of impactor masses. It turns out that the impact energy relates better to the damage produced than impact velocity or impactor mass alone [21]. The kinetic energy of a projectile is given by the equation (2.2). Davies however shows that impacts with the same energy but with a significant difference in impactor masses (and thus impact velocities) give a different dynamic response [4]. In this example, the difference in impactor mass was a factor of 150, with the smaller mass (10g) causing more damage.

$$E = \frac{1}{2} \cdot m \cdot v^2 \tag{2.2}$$

The relationship between the impactor size and the resulting damage size turns out to be dependent on the specimen boundary conditions. According to Yigit and Christoforou, a fully supported plate is unable to have any bending deformation due to impact, and will have an increasing damage size with increasing impactor size [22]. Shim and Yang however found an inverse relation in the case of no back support [23]. In their work, they show that bending effects cause a specimen to have a larger damage area when it is impacted with a smaller tip radius. In a review paper by Shah et al., it is explained that in most low-velocity impact testing, a hemispherical impactor tip is used [24]. Just as in the research by Shim and Yang, it is shown that a decrease in the tip diameter leads to an increase in damage, as well as an increase in likelihood of perforation. Figure 2.8 shows several typical impactor shapes that are typically used for impact testing. The effects of pre-stress on a sample upon impact is researched by Whittingham et al. [25] and Mitrevski et al. [26]. It was found that for both glass- and carbon-fibre reinforced composites, the effect of both uni-axial and bi-axial preloads is in most cases insignificant. Only in the case of a conical (sharp) impactor, a larger indentation depth can be observed with a larger tensile preload, while the damage area does not increase. Several strain levels up to 1500 $\mu\epsilon$ were used as preload, and impact energies of 4, 6 and 10 J. A study by Schüler proved that in the case of high velocity impacts, there is a relation between tensile static preloads and impact response [27]. Impacts

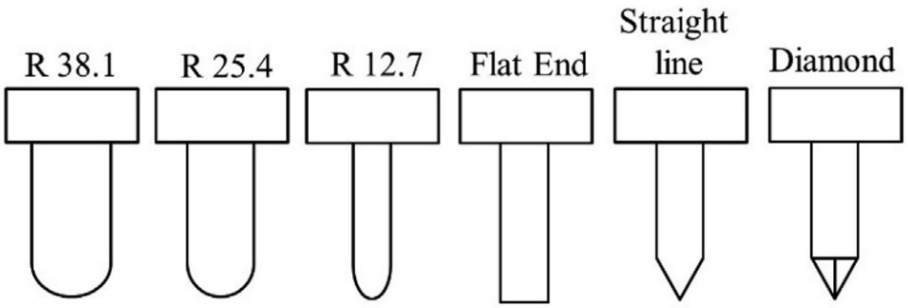


Figure 2.8: Several impactor geometries used in impact testing [24]

with a blunt impactor with a velocity between 70 and 105 m/s were performed on CFRP specimens with and without preloads. It was shown that for a tensile preload at 40% of the design limit load, the intra-ply damage increased while the delamination area decreased, as compared to impacting an unloaded structure. The impact energies were between 55 and 120 J.

Fibre reinforced composite materials are usually brittle by nature, and cannot absorb damage by plastic deformation. Therefore, the only way of the material to absorb energy is through elastic deformation and damage mechanisms. Carbon fibres are especially brittle. In typical Charpy impact tests, S-glass/epoxy and Kevlar/epoxy were able to take up more than five times as much energy as carbon/epoxy laminates [28]. The amount of energy a material can take up before failure relates to the area under its stress-strain curve. Since carbon fibres are very stiff, this is one of the reasons that they are not able to absorb energy as well as, say, glass fibres or most metals. The stiffness and stress-strain curves are not the only factors at play however. Once damage initiates, the damage progression also has a large influence on the ability to absorb energy. It turns out that materials reinforced with E-glass or Kevlar fail in a much more progressive manner as compared to the sudden failure typically seen in carbon reinforced materials [29]. One of the ways that manufacturers have tried to deal with this discrepancy is through hybridization, where various fibre materials are combined. This combining of fibres can be done in an inter-laminar manner where plies of different materials are alternated, or through combining tows of different materials in a single ply (intra-laminar). Through this method, the high strength and stiffness of carbon fibre can for example be combined with the higher damage resistance of Kevlar fibres. Quite some research has been done into techniques like stitching and Z-pinning as well, in a search for higher out of plane fracture toughness. In Z-pinning, short, straight fibres are applied in the z-direction of the laminate (out of plane), essentially holding the different plies together. Techniques like stitching and Z-pinning work well, but are often detrimental do undamaged in-plane properties [4]. Improving the properties of thermoset resins is being done, but the advances are not major. Moreover, thermoplastic matrix materials are often more ductile than thermosets such as epoxy and are able to improve the fracture toughness of a composite material [20]. These materials also have some disadvantages however, in terms of mechanical performance, processing and cost.

Four dominant failure modes are observed when exposing laminated composite materials to impact loading: matrix cracking (intra-laminar), delamination (inter-laminar), fibre-matrix debonding and fibre fracture. Because of the interaction between failure modes, it is hard to predict damage in composites, and there is a significant dependence on experiments aside from numerical and analytical models. Since the damage mechanisms and failure modes are more complex, conventional analytical and numerical models used for metals often do not work. Delaminations tend to occur near the midplane of the laminate, where the transverse shear stress is the highest in the case of an out-of-plane loading. These delaminations are often somewhat peanut-shaped (Figure 2.9), with their direction determined by the fibre directions on both sides of the interface. For the initiation of delaminations in a laminate, mode I fracture is dominant, while mode II fracture is dominant in the propagation of a given delamination [30]. Moreover, directly under the point of impact some compressive stress is present, reducing the tendency for splitting and delaminations at or near the top (impact) surface. Lastly, bending stresses due to impact can cause cracking at the back surface of the material [31]. Together, these effects make hidden damage states a major concern in composite structures. In the case of unidirectional layups,

splitting occurs very easily under impact, meaning these layups are unsuitable for applications where impact might occur. It turns out that having +/- 45 °plies on the surface of a laminate increases the impact resistance because it reduces the tendency for the longitudinal, main load-carrying plies to get damaged [29]. More generally, adding +/-45 °plies creates a more flexible laminate, meaning the material is able to take up more elastic energy before any damage occurs. In addition, the impact resistance can be increased by reducing the stiffness mismatch between individual plies. This is done by keeping the difference in layup angle low between the plies.

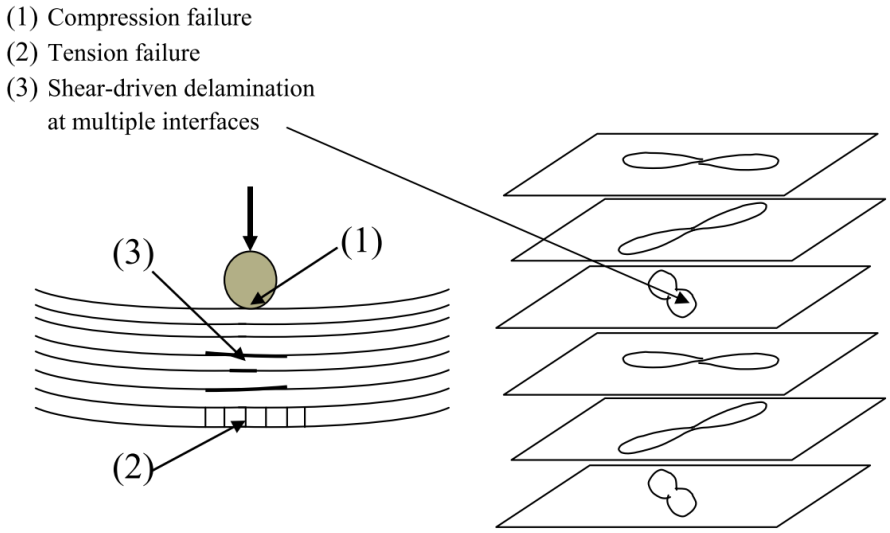


Figure 2.9: Impact damage mechanisms [4]

## 2.3. Combined Loading

The combined effects of impact and other loadings have been studied by tension after impact (TAI), compression after impact (CAI) and fatigue after impact (FAI). Quasistatic CAI and compression-compression or compression-tension FAI have been studied the most, due to the propensity of composite materials to form delaminations during an impact event, which typically reduces the compression strength significantly. While fibre damage is critical for the residual tensile strength of a laminate, matrix toughness is the main driver behind residual compression strength of a quasi-isotropic laminate [20]. According to Vlot, tension-tension fatigue is much less critical than types of fatigue involving compression, and the splitting caused by T-T fatigue tends to remove stress concentrations from the initial damage [3]. This removal of stress concentration may even increase the static tensile stress again. Because of the higher severity of compression loading after impact, tension loading is less researched and therefore less well understood. Researchers like Kang and Kim have shown that impact indeed also has a detrimental effect on tension-tension fatigue [32]. Figure 2.10 shows the results of their experimental campaign.

Symons and Davies performed tension-compression fatigue tests (R=-1) on CFRP specimens with two types of impact loading: a 5J impact creating BVID, and a 10J impact creating visible impact damage [33]. It was shown that doubling this impact energy reduced the fatigue life roughly by an order of magnitude. The coupons were taken out of the testing machines to be C-scanned at certain intervals, showing that the initial damage area due to the impact event does not increase significantly during fatigue testing. This was also observed by Swanson et al. [34]. The severity of the damage however did increase, as was observed visually in the form of cracks and local delamination buckles. In the tests by Symons and Davies, strain measurements were performed on only two specimens, but they indicate an increase in strain - or decrease in stiffness - during testing, as measured using a clip gauge extensometer. This effect is seen in both the tensile and compression sides of the cycles.

In research performed by Koo et al., residual strength characteristics as well as residual fatigue life characteristics were found for specimens with impact damage [35]. Tests were performed with graphite/epoxy

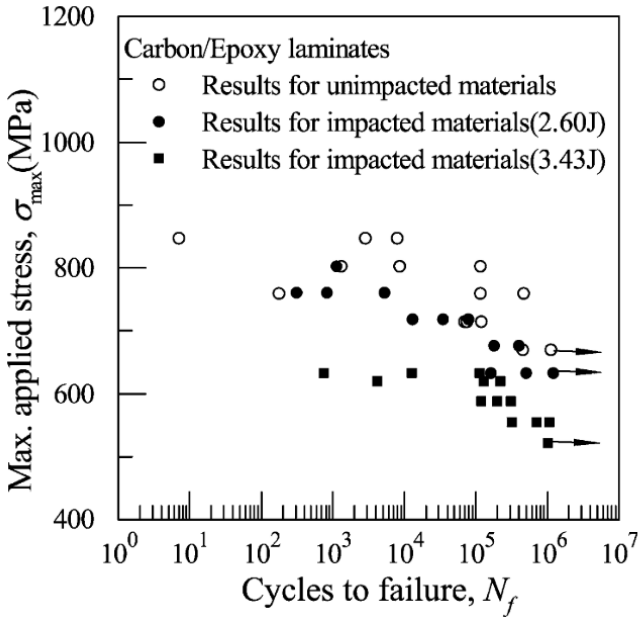


Figure 2.10: Effect of impact energy on tension-tension fatigue performance [32]

specimens with plain-woven prepreg plies. Impact energies of 5 to 23J were used to determine residual static strength values. The fatigue tests were performed on specimens impacted with 5J with a hemispherical impactor, which decreased the tensile strength to about 70% of its virgin state. Cyclic testing was performed with a frequency of 5 Hz and a stress ratio of 0.1. It is concluded that the impact damage decreases the fatigue life of the specimens, while increasing the scattering range. A model is proposed that is able to predict the fatigue life of both intact and impacted specimens well.

In work performed by Tai et al., tension-tension fatigue behaviour after low energy impact of carbon fibre epoxy laminates was investigated using a $[0/45/90/-45]_{2s}$ layup [36]. Ultrasonic C-scanning was used to show that the damaged area increased for larger impact energies, and indeed the damaged area grew during fatigue loading. Fatigue loading was performed at different maximum stress levels with a stress ratio of R=0.1 and a frequency of 3 Hz. It was concluded that the the impacted specimens not only exhibit reduced fatigue life as expected, but also have less scatter than the virgin specimens (see Figure 2.11). Interestingly, the difference is larger for smaller maximum stress levels. This might be explained by the fact that at lower energies, failure is dominated by matrix cracking and delaminations, which are already present due to the impact event. At high stress levels on the other hand, the load is carried more by the fibres, which are largely unaffected by the LVI event. The stiffness change during the fatigue cycling was particularly interesting. During roughly the first $10^3$ cycles the stiffness increased, after which it started decreasing up until failure. The authors explain that the the stiffness is defined as the slope of the tangent of the stress/strain curve, but there is no explanation on how the strain data was measured. The initial increase in stiffness is explained by the possibility that the +/- 45 fibres might change orientation slightly upon loading, essentially straightening out and carrying more load with respect to the matrix. Lastly, the initial stiffness of the impacted specimens was lower than that of the virgin specimens, and the stiffness reduction rate was higher.

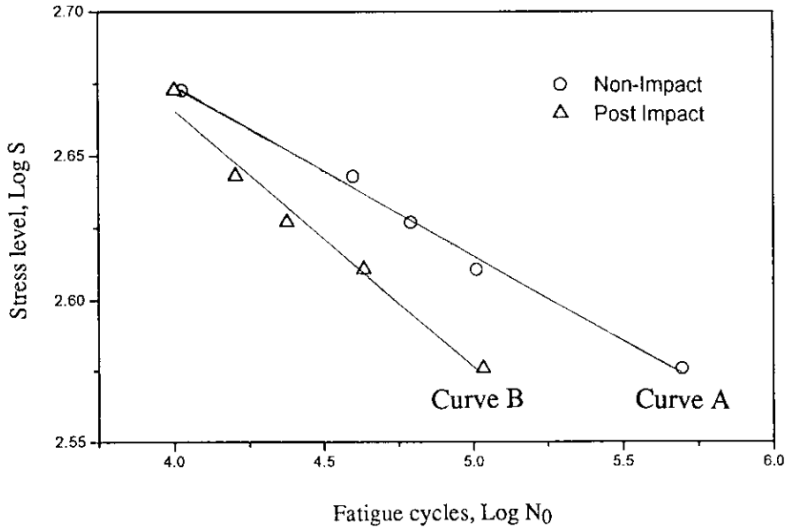


Figure 2.11: S/N curves of non-impacted and damaged CFRP specimens [36]

It is clear that not too much research has been performed on tension-tension fatigue loading of composite samples with impact damage. The studies that have been done so far have shown a reduced fatigue life when impact damage is present, without necessarily a distinct increase in damage area during the fatigue life. No research was found on the effect of an impact occurrence during a fatigue campaign. It is therefore not known if the damage area and severity will be the same for an impact event either on a virgin sample or on a sample with damage present. Since impact damages are often categorized by visibility, it is important to know if the area and severity of a damage are still related in the same way. In the worst case, a damage due to impact may be more severe when some fatigue damage is already present, without showing a larger damaged area.

# 3

# Structural Health Monitoring

Non-destructive inspection (NDI) techniques, in combination with visual inspections, have widespread use in aircraft maintenance operations to check for any structural damage that needs to be repaired. These practices are expensive, since the aircraft needs to be on the ground and the inspections are labour intensive. One way to make this more efficient is by using on-board sensor technology to identify any damage in the structure. This is referred to as structural health monitoring (SHM), and its use may lead to more efficient maintenance practices through condition based maintenance (CBM). This will be discussed further in section 3.1, after which an introduction to several sensing technologies is provided in section 3.2

## 3.1. Towards Condition Based Maintenance

The maintenance cost of aircraft is a significant contributor to the overall operating cost for airline companies. In addition to scheduled inspections, unscheduled repairs will be performed in case certain defects are found during regular operations or in pre-flight inspection. Both maintenance events are expensive for the operator, and reducing the time of any aircraft spent on the ground is of great value. According to Speckmann, maintenance cost has great potential to be reduced, in contrast to cost factors such as fuel and airport fees [37]. This is mainly through the adoption of condition based maintenance, as opposed to time-scheduled maintenance. A simple visualisation of this different maintenance strategy is presented in Figure 3.1.

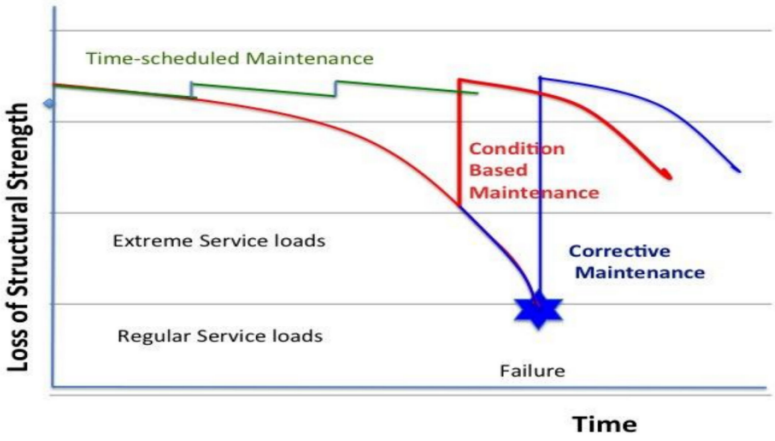


Figure 3.1: Example of optimised maintenance operations using CBM [38]

In addition to the direct maintenance cost, Steinweg and Hornung predict that SHM systems could save structural weight and increase the lifetime of an aircraft [39]. In a case study with an Airbus A320-200, they predict that a lifetime increase of 10'000 to 20'000 flight cycles could be possible. Lower complexity SHM systems have already proven themselves, for instance for damage detection in critical drivetrain components in helicopters [38]. While designing a good SHM system for metallic aircraft is challenging enough, composite materials provide additional complications [40]. For example, their behaviour is anisotropic, they exhibit a combination of different failure modes and they typically demonstrate more scatter in mechanical testing. Even so, the use of composite materials in commercial aircraft has been rising consistently over the past few decades, therefore the potential for these systems gets ever larger.

Damage identification in a structure can be done in numerous ways, with varying amounts of information being gathered depending on the type of sensors and diagnostic tools used. Worden et al. have recognised five hierarchical levels of damage identification with increasing amounts of knowledge about damage in a structure [41].

1. **Detection**: an indication that some damage is present in the structure
2. **Localisation**: an indication of where the damage is likely to be located
3. **Classification**: an indication of the type of damage
4. **Assessment**: an indication of the extent or size of the damage
5. **Prediction**: an indication of the remaining useful life of the structure

Being able to consistently detect and localise damage during aircraft operations could already provide a major improvement over current preventive maintenance practices. That is, of course, as long as the system is reliable and robust enough. Going further and identifying level 3 and 4 features would provide additional benefits by being able to assess the criticality of the structural damage. Finally, the use of prognostic tools could be adopted to estimate the remaining useful life of a structure. An example of experimental research on this is performed by Eleftheroglou et al. [42].

widespread CBM for composite aircraft can only be achieved safely if structural damage during operations can be detected accurately and reliably. In order to achieve this, several aspects will require more investigation:

- Composite material behaviour and damage patterns will need to be investigated further. Specifically, how do these materials respond to various (combined) loading scenarios and how do measurement systems pick this up?
- Reliable sensor systems are needed with high probability of detection. In addition, they need to be lightweight and positioned well in relation to expected damage locations. Acquisition systems and computers are needed either on-board for continuous data analysis or ground-based for intermittent analysis.
- Good diagnostic and optionally prognostic tools need to be developed, for example using physics-based or data driven models. Note that even when black box data driven models are used, it is still necessary to investigate material behaviour and their relation to sensor system outputs.

## 3.2. Sensing Methods

Many different measurement techniques can be utilised to measure the strain and damage response during the mechanical testing of materials. Some of these methods can be used for continuous SHM as well, meaning they can be used to monitor a structure during operation.

While C-scanning is used to assess delamination damage in the testing work that is part of this thesis, it will not be detailed further. Ultrasonic C-scanning is a mature technique and the results are simple to

interpret - at least in this case. The testing work instead relies heavily on a specific implementation of the digital image correlation (DIC) technique, and it is therefore deemed helpful to elaborate upon. Details of the general workings of this are presented in subsection 3.2.1. Note that both of these techniques do not lend themselves for use as part of a continuous SHM system in aircraft, but are excellent tools in experimental laboratory settings. In contrast, the acoustic emission (AE) measurement technique used in this project as well is potentially suited for SHM applications. This method is explained in subsection 3.2.2. A short overview of some of the other measurement techniques that are not used in this project but may be useful in SHM applications is presented in subsection 3.2.3. Be advised that only a general introduction of the relevant measurement techniques is presented in this chapter. Chapter 4 will detail the implementation of DIC and AE in this project specifically.

### 3.2.1. Digital Image Correlation

Digital image correlation is a non-contact strain measurement technique where one or multiple cameras are used to track the translation and deformation of a surface. A speckle pattern is painted on this surface to allow images to be correlated back an original, undeformed image. DIC is a powerful method, with which accurate 2D strain patterns and 3D displacement patterns can be measured. If thin structures are considered in combination with in-plane loading, the strain may be considered equal throughout the thickness.

In a paper by Broughton, GFRP open-hole specimens were tested in both static and cyclic tension [43]. Strain measured using a DIC setup was compared to the strain measurements using fibre Bragg grating (FBG), several strain gauges and an extensometer with a gauge length of 50 mm. The average longitudinal strains as measured over the centreline of the specimen (across the hole) were compared. As shown in Figure 3.2, there is good agreement between the various techniques, until there is some divergence at higher loads due to increasing damage around the hole. Upon further loading the damage became too severe and the DIC setup was not able to capture local strains right next to the hole anymore. Figure 3.3 shows the strain as measured by DIC along the centreline of the specimen, compared to the analytical solution of a composite plate with a hole. The measurements are in good agreement with the theoretical curve. The accuracy of DIC measurements is dependent on, among other things: camera resolution, speckle size, speckle quality, specimen alignment, lighting conditions and settings in the post-processing software [16]. Aside from being sensitive to changes in camera position or vibrations, Pan et al. have reported that a change in camera temperature during measurements can lead to an error of 30-50 microstrain per degree celcius [44]. It can be concluded however that when set up correctly, it is a very powerful method able to capture a detailed surface strain field.

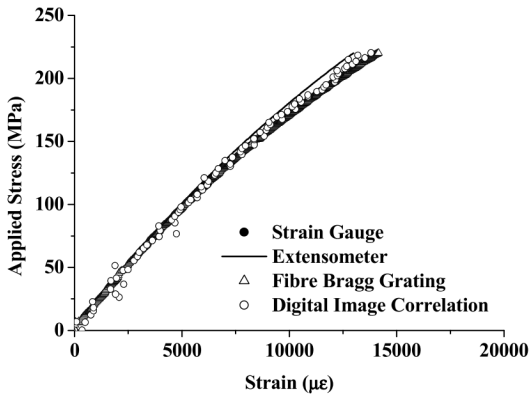


Figure 3.2: Stress-strain curve measured with various techniques [43]

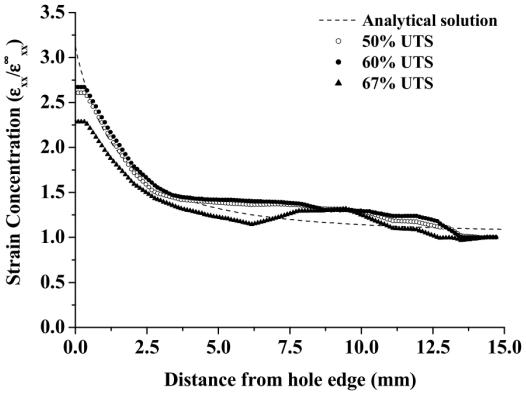


Figure 3.3: Strain concentration next to hole edge measured with DIC [43]

### 3.2.2. Acoustic Emission

When a structure is loaded, elastic energy builds up in the material. When some form of damage occurs, elastic energy is released and a transient elastic wave is formed. This wave can be picked up using sensors, at which point the waveform and its features can be analysed. Bourchak et al. [45] and Saeedifar et al. [46] have shown that this technique is able to capture damage events well. An

AE sensor consists of a housing with a piezoelectric transducer which makes contact with the test specimen through a wear plate. A signal picked up by the sensor is typically pre-amplified before going to a data acquisition device.

A schematic representation of a typical AE signal is taken from Goutianos [47] and shown in Figure 3.4. Various features are distinguished by the acquisition system that can be stored without needing to save the complete waveform. This also makes it easier to quantify the measurements. Features such as the amplitude and energy say something about the intensity of the damage: a larger damage event is likely to emit a stronger acoustic wave. A cumulative sum of the signal energy can be taken for example to get an indication of energy release over time. Moreover, the shape and size of a signal (and thus its features) can say something about the type of damage: a fibre fracture is likely to emit a different signal than a matrix crack. Liu et al. have suggested typical AE amplitude ranges for the different failure modes in carbon fibre/epoxy specimens [48]. Although rough and hard to generalise, suggested ranges are 40-60 dB for matrix cracking, 50-70 dB for for fibre/matrix interface debonding, 60-80 dB for delamination and 80-100 dB for fibre fracture.

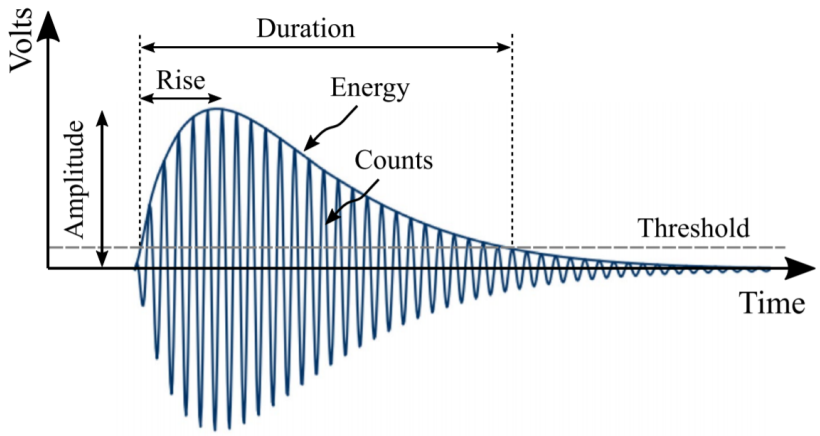


Figure 3.4: Schematic AE signal [47]

Thresholds on for example frequency and amplitude are set to avoid measuring too much noise. Care needs to be taken to choose these, as too strict a threshold may filter out the smaller damage events. Also, a signal may not be related to damage but to for example friction between two delaminated plies [7]. An acoustic wave may also reflect from the edge of a material back into the sensor, measuring the same (albeit weakened) signal twice. To avoid this, a rearm time is set, where a sensor will not pick up a new signal for a certain time period after the previous signal. Furthermore, an algorithm can be used to localise the source of a signal. If a certain area is of interest, any signals originating from outside that area can be filtered out. The wave velocity through a material can be tested using a pencil lead break test, after which the time difference between a signal being picked up by multiple sensors is used to calculate the signal source. Two sensors are enough to achieve 1D localisation on a longitudinal object.

According to Groves, acoustic emission is a particularly powerful measurement technique to be used in integrated SHM systems in aircraft [40]. Smart algorithms are needed to automate signal processing in order to attain reliable data about damage events without being overwhelmed by data.

### 3.2.3. Other Measurement Techniques

Various other measurement techniques may be used in embedded SHM systems in aircraft. An overview is provided below. An introduction of various sensing techniques in SHM may be found in [38], [40] and [37]. Especially Fibre optic and piezoelectric (PZT) sensors as used in acoustic wave detection are well developed and have good potential for widespread use in monitoring systems.

Aside from the passive acoustic emission sensing as described in the previous subsection, active acoustic emission can be used as well. A guided wave such as a lamb wave is sent through a structure which is then picked up by surrounding PZT sensors. An advantage is that the location of these sensors with respect to each other is fixed, therefore any changes to received signals indicate changes to the structure that can be localised. A downside with respective to passive acoustic sensing however is that a signal has while a damage state may be recognised by sending out signals, there is no damage history being recorded as with passive AE sensing. An example of research using both an active and passive method is performed by Saeedifar et al. [49].

Fibre optic sensing (FOS) methods such as FBG rely on the change in optic signals to measure for example strain in a structure. Their advantages include the option for multi-point sensing along a single fibre, high sensitivity, light weight and the option to be embedded in composite structures. A good review paper on various FOS methods is written by Di Sante [50].

Electromagnetic techniques such as Eddy current sensing may be used in structures that are electrically conductive, which means it may be useful for CFRP but not for GFRP structures. While the technique is best known for use during non-destructive inspection, small sensors can be integrated permanently in structures. A large downside of these methods is that they are point-based, they only inspect an area directly near the sensor.

Vibration methods make use of changes in vibrational behavious of a structure to identify damage. While widely used in civil engineering applications, their use in aerospace applications remains limited. The downside of these methods is that they have a low resolution, and are typically able to find small cracks only in simple structures. Fan and Qiao have written a review paper discussing various vibration based methods [51].

Intelligent coatings and smart materials are also under devlopment and may be used in SHM applications in the future. An example of this could be a coating with nanomaterials that responds to a change in shape. This could potentially provide strain information over a distributed area. The technology readiness levels of these technologies however are not as high as with for example fibre optic sensing or acoustic emission.

# 4 Methodology

This chapter details the methodology and corresponding experimental setup that was used to attain the results. A fatigue test machine was used in combination with a gas gun so an impact event could be iniated on the CFRP specimens in-situ. A combination of Digital Image Correlation (DIC) and Acoustic Emission (AE) was used to measure the specimen response to these loading conditions. This test setup is an adapted version of the one used by Eleftheroglou et al. in [52].

This chapter starts by explaining the test specimens in section 4.1. Afterwards, an overview of the test area and the equipment is given in section 4.2. Then, section 4.3 provides more details on the test setup and its test parameters. Finally, the measurement equipment and parameters are explained in section 4.4.

## 4.1. Test Specimens

The specimens used in this testing campaign are made from carbon fibre reinforced epoxy. Eight plies of unidirectional (UD) prepreg were used in a quasi-isotropic pattern, with a ply of plain woven (PW) (0/90) prepreg on either side. The nominal cured thicknessess of the UD plies and the woven plies are 0.190 mm and 0.218 mm respectively. The layup used is [(0/90)F/45/90/-45/0]s, which has a total cured thickness of about 2 mm. Table 4.1 shows the layup configuration more clearly.

Table 4.1: Specimen layup

| Ply | Orientation | Type |
|---|---|---|
| 1 | 0/90 | PW |
| 2 | 45 | UD |
| 3 | 90 | UD |
| 4 | -45 | UD |
| 5 | 0 | UD |
| 6 | 0 | UD |
| 7 | -45 | UD |
| 8 | 90 | UD |
| 9 | 45 | UD |
| 10 | 0/90 | PW |

Ten specimens each were cut from four cured panels of 0.5 x 0.5 m using a diamond saw. Because of the possibility of variation between the four panels, care was taken to use random specimens for each test series. Each specimen has a label containing two digits; the first digit referring to the panel from

which it was cut (1-4), with the second number separating the specimens from within that panel (0-9). For example, sample 26 refers to the 6th specimen taken from the second panel. Because the panels were mixed up, the specimen numbers are deliberately not ordered. See Table 4.2 for an overview of all the specimens used. Note that sample 19 is mentioned twice, since it was C-scanned after impact. Also, the number of distinct specimens is 38, as two samples were already damaged and were not expected to provide repeatable results.

Table 4.2: Specimen overview

| | | |
|---|---|---|
| Static tests | 16 20 33 48 | |
| Fatigue trials | 26 36 | |
| Impact trials | 19 27 | |
| C-scanned samples | 12 15 19 21 28 29 32 37 40 49 | |
| Fatigue tests | Impact | No impact |
| No pause | | 46<br>10<br>18 |
| Pause at 0% | 42<br>30<br>25 | 43<br>14<br>39 |
| Pause at 14% | 24<br>41<br>44 | 22<br>34<br>45 |
| Pause at 20% | 47<br>17<br>38 | 23<br>11<br>31 |

The specimens have a dimension of 400 x 45 mm, with a 10 mm central hole. The dimensions are provided in Table 4.3 for quick review. Because dogbone-style samples often do not work well with composite materials, a hole is chosen as a local weakening point, to enforce a damage initiation area in the middle of the sample. The outer 50 mm on either side of the sample was used to clamp in the hydraulic grips of the fatigue machine, so the distance between the grips that was actually loaded was about 300 mm. Paper end tabs were glued to these end sections to create more friction between the sample and the clamps. A black and white speckle pattern was applied so the DIC system could track surface deformations during testing. This coating was applied on the smooth (mould) side instead of the backside, where the vacuum bag and other production consumables created a rougher surface finish. This way, higher quality DIC images are obtained. The white base layer was applied using a spray can with slightly elastic paint, to avoid cracking of the paint before the material behind it damages. After drying, the black speckle pattern was applied using a special ink stamp from the manufacturer of the DIC system, Correlated Solutions.

Table 4.3: Specimen dimensions

| Length [mm] | Width [mm] | Thickness [mm] | Central hole diameter [mm] |
|---|---|---|---|
| 400 | 45 | 2 | 10 |

## 4.2. Equipment

Before detailing the specifics of the experimental campaign, it is helpful to acquire some familiarity with the test setup as a whole. An overview of the test area is shown in Figure 4.1, with important pieces of equipment numbered and explained.

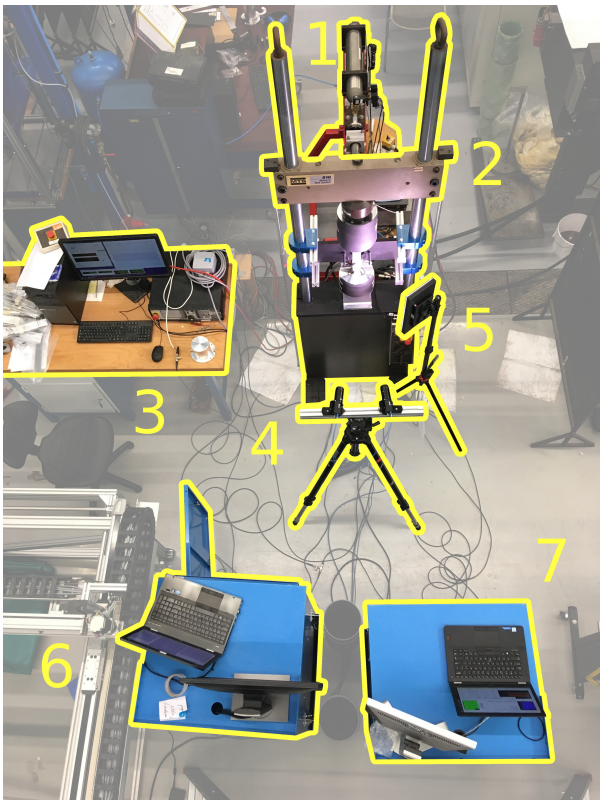


1. Gas gun
2. Servo-hydraulic test machine
3. Test machine controller and interface
4. DIC cameras
5. Light source for cameras
6. DIC data acquisition
7. AE data acquisition

Figure 4.1: Test area overview

Figures 4.2 and 4.3 show the front and rear of the sample when clamped into the testing machine. Note the safety device that is painted black to avoid excessive reflections from the DIC light source entering the cameras. Black screws are used to cover holes which would otherwise reflect light on their inner thread, thus overexposing the cameras. Black paper is taped onto the upper and lower grip heads on the test machine for further glare reduction. More detail on the safety device is provided in subsection 4.2.1

Two clamps can be seen on the sample. These are each situated 100 mm from the central hole and serve to clamp the acoustic emission sensors to the back of the specimen. On the front surface, a fine black and white speckle pattern is painted for the DIC system to be able to track surface deformations.

The gas gun is shown in Figure 4.4, with the various components highlighted and explained. The gas gun was aimed at the rear side of the specimen, to avoid any interference with the DIC setup. Before starting any fatigue test, a bullet was loaded from the front of the barrel, pushing it back until it reached a narrow section. The required air pressure was set on the control unit (6). When the fatigue test was interrupted in order to impact, the tank (3) was filled using a tube from an external compressed air source. The device was then triggered using a switch (7), opening the trigger valve (2), releasing the gas and thus shooting the impactor. The velocity could then be calculated from the time difference measured by two sensors, shown on the display (5).

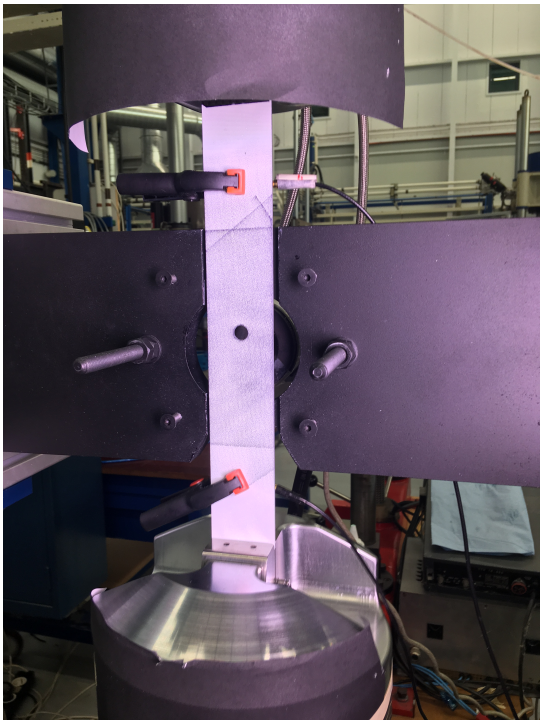

Figure 4.2: Front view of sample in test setup

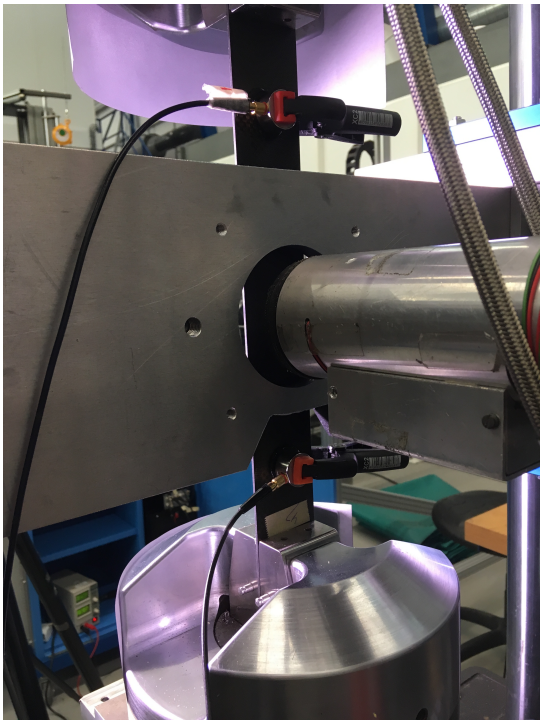

Figure 4.3: Rear view of sample, with gas gun in place

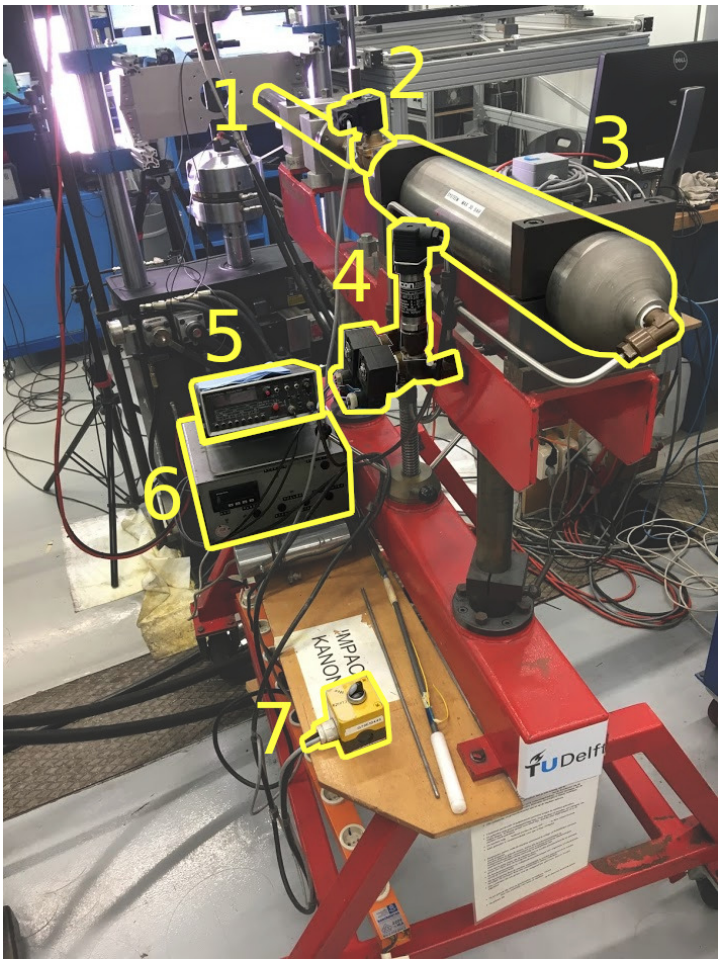


1. Barrel
2. Trigger valve
3. Air pressure tank
4. Pressure sensor, fill valve and empty valve
5. Velocity measurement display
6. Control unit
7. Trigger switch

Figure 4.4: Impact gun

### 4.2.1. Impact safety

For the combined loading tests, the impact event on a specimen has to occur somewhere during the cyclic loading program. It is believed beneficial to leave the sample under tension in the fatigue machine during impact, the reasons for this are explained in subsection 4.3.3

Because the sample is tested in a vertical orientation, it needs to be impacted horizontally to create an out of plane impact scenario. Therefore, a safety device was in place to prevent the impactor from accidentally hitting any people or equipment in the vicinity after a penetration or ricochet. Figure 4.5 shows a schematic drawing of this device. A metal plate is attached between the two vertical columns of the test machine, located slightly behind the test specimen. The plate contains a hole to shoot through in order to hit the rear surface of the specimen. A device is attached to the end of the gas gun barrel that measures the speed of the bullet and prevents it from escaping after a ricochet. The velocity measurement is further explained in section 4.3. An aluminium enclosure is bolted onto the front of the metal plate that catches the bullet in case it penetrates the sample. This catching 'bucket' is shown in Figure 4.6. It blocks the view of the DIC cameras, so it was only attached briefly during the moment of impact. Care was taken to leave a gap between the plate and the enclosure, so the specimen would not hit the enclosure due to impact. This gap was just small enough that the bullet could not pass through.

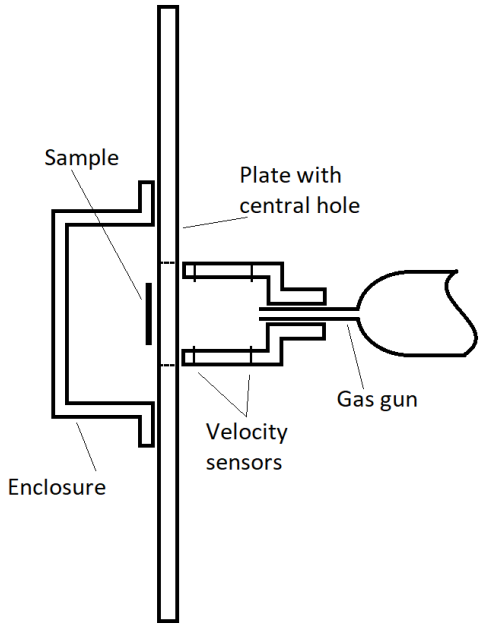


Figure 4.5: Schematic drawing of the safety device

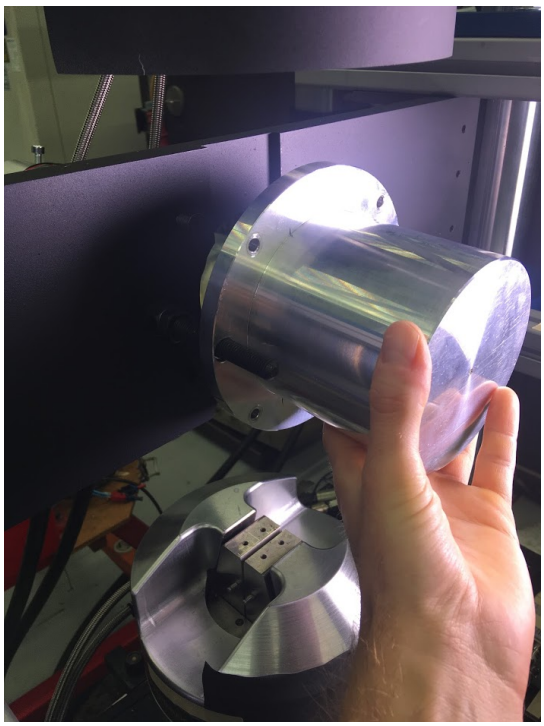

Figure 4.6: Enclosure to catch the impactor

## 4.3. Test Parameters

This section details the test parameters used. In subsection 4.3.1 the static and fatigue test parameters are explained, the pausing procedure is explained in 4.3.2 and subsection 4.3.3 describes the impact setup.

### 4.3.1. Static and Fatigue Testing

All tests were performed on a servo-hydraulic fatigue machine from the company MTS. The machine has a force capacity of 100 kN, which was ample for these tests. First some quasi-static tests were performed on four different samples, with the ultimate tensile strength (UTS) and global failure strains shown in Table 4.4. These tests were displacement controlled, with a speed of 1 mm/min. The force-displacement curves are shown in Figure 4.7. While some non-linearity is observed which is to be expected, there are no significant load drops before final fracture. This is important as it shows that no

significant load carrying plies are likely to fail within the first fatigue loading cycle of the dynamic tests. However, small load drops are seen when zooming in and cracking sounds were heard well before ultimate failure. The black dashed lines indicate the upper and lower force limit of the fatigue tests.

Table 4.4: Static test results

| Sample | UTS [kN] | failure strain [%] |
|---|---|---|
| 16 | 43.6 | 1.22 |
| 20 | 46.5 | 1.25 |
| 33 | 44.8 | 1.22 |
| 48 | 42.0 | 1.17 |
| Mean | 44.2 | 1.21 |

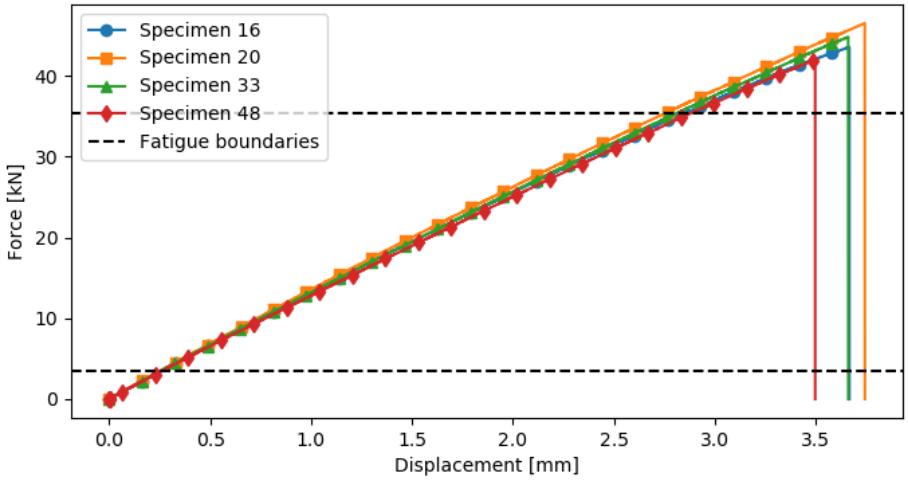


Figure 4.7: Load-displacement curves of the static tests

For cyclic load testing, all tests were performed with the same fatigue parameters. The load was applied with a frequency of 10 Hz and with a peak load of 80% of the failure load, 35.4 kN. With a stress ratio of R=0.1, the minimum load during each cycle was 3.54 kN. The loading cycles were sinusoidal in shape. The test machine was load-controlled, so any damage would not create a drop in load but rather an increase in displacement. Table 4.5 shows a short overview of the fatigue parameters used. Note that for the samples that were c-scanned instead of tested to failure, a frequency of 6 Hz instead of 10 Hz was used. This was due to tuning problems with the fatigue machine.

Table 4.5: Fatigue test parameters

| Failure load [kN] | Max fatigue load [kN] | Stress ratio [-] | Pause load [kN] | Test frequency [Hz] |
|---|---|---|---|---|
| 44.24 | 35.4 | 0.1 | 19.5 | 10 |

It is recognised with such a high maximum fatigue load, some of the plies will already be damaged significantly within the first loading cycle. This became immediately clear due to audible and visible

cracking upon first loading. This is emphasised by Burchak, who states that "...the arbitrary choice of fatigue stress levels at a high percentage of UTS should be re-considered in order to avoid the destruction of relevant damage states in the first cycles of fatigue loading." [45]. However, such high maximum loads were deemed inevitable when testing until failure due to time constraints. A test performed at 70% of the UTS took about 11 hours, whereas none of the tests performed at 80% took longer than 3.5 hours. Even upon loading to 70% of the failure load, the specimen cracked audibly and visibly.

### 4.3.2. Pausing the Fatigue Test

For the combined loading tests, the impact event on a specimen has to occur somewhere during the fatigue program. It is desirable to leave the sample in the machine for this, as taking it out and clamping it back in again will create slight differences in how the specimen is clamped and loaded. Also, it would mean that the specimen will be fully unloaded for a while, and it will take longer before the cyclic loading program can be continued. In order to resemble a situation as close as possible to a true impact during cyclic loading event, the fatigue program was interrupted and the specimens held at a constant load, at which point it was impacted. This constant load was necessary to ensure that every impact occurs at the same preload. A load of 19.5 kN was chosen during the pause, which is the average of the maximum and minimum fatigue loads. Moreover, the AE sensors could be damaged by an aggressive event such as impact, so they had to be removed beforehand.

The interruption of a fatigue program may have an effect on the behaviour and fatigue life of a specimen. In order to take this into account, samples that were not impacted were paused as well, for the same duration. This way, samples that were paused at different thresholds can be compared, as well as specimens that are either impacted or not, while paused at the same threshold.

In the research discussed in section 2.1, it was proven that DIC is an accurate method of measuring the strain response of composite specimens [14] [15] [16]. An increase in strain corresponds to a decrease in stiffness, which directly relates to the extent of damage in the material. In contrast, a fatigue cycle based threshold is only directly linked to testing time. It was therefore expected that the increase of strain during fatigue is a better indicator of the damage state than simply the number of fatigue cycles a specimen has gone through. This, in turn, should result in less scatter between the samples. In order to use such a threshold, the strain needs to be tracked real-time during testing. This is further explained in Subsection 4.4.1. Three different strain thresholds were chosen: 0%, 14% and 20% strain increase. This is based on the strain increase since the first measured point. Note that this does not strictly relate fully to the loss of stiffness since before the test, as the first datapoint is taken at the maximum fatigue load, when already some damage is present (see Subsection 4.3.1).

The duration of the pause was dictated by the time it took to perform the procedures necessary for a safe impact to take place. Based on the first few tests, it was seen that this took about 9.5 minutes, so this was used for the remainder of the tests. Using the same time for every specimen is important, even though the experience gained during testing meant that the procedures could be carried out faster for later tests. Below is a list of the individual steps that were taken from pausing until resuming the fatigue program.

1. Pause fatigue program
2. Wait for the force reading to reach 19.5 kN
3. Start timer
4. Pause AE acquisition
5. Remove AE sensors to avoid damage
6. Take out black bolts in safety device (see Section 4.2)
7. Bolt on bullet 'catcher'
8. Fill pressure tank of impact gun
9. Impact
10. Check that no pressure is left in the pressure tank
11. Roll back gas gun and remove bullet
12. Remove bullet catcher

13. Put back black bolts to avoid overexposing the cameras
14. Put back AE sensors on sample
15. Continue AE acquisition
16. Wait for 9.5 minutes to have passed on timer
17. Resume fatigue program

### 4.3.3. Impact Testing

To serve as impactors, custom bullets were produced with an aluminium tip screwed into a POM (Polyoxymethylene) rear section, see Figure 4.8. The tip is hemisphericalwith a radius of 5 mm. Some more dimensions of the impactor are provided in Table 4.6, and the drawings are available at DEMO (Dienst Elektronische and Mechanische Ontwikkeling) in the Aerospace Engineering faculty at TU Delft. The plastic rear section acts mainly to seal the gap between the barrel and the bullet. A secondary function is to ensure the centre of mass of the impactor lies in front of the centre of pressure, which guarantees stable flight. The mass of a single bullet was 30.7 grams. The variation in mass between the bullets was less than 0.1 gram, not enough to cause significant differences in the impact energy.

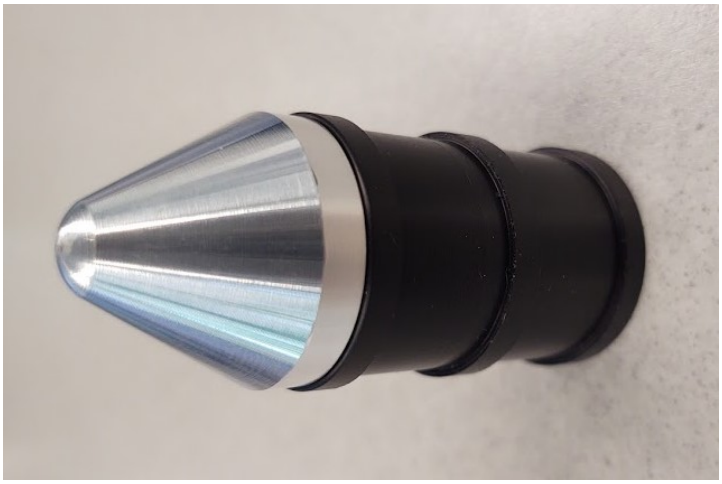

Figure 4.8: Impactor used

Table 4.6: Impactor dimensions

| | |
|---|---|
| Total length | 55 mm |
| Tip length | 20 mm |
| Radius of impact tip | 5 mm |
| Diameter of rear section | 25 mm |
| Diameter of wide tip section | 24 mm |

A device was used to measure the travel time between two sensors as the bullet left the barrel. With this travel time, the bullet velocity was calculated. With the bullet mass and velocity now known, the impact energy can be calculated using equation 4.1. The impact energy was chosen to be 10 J for all samples to be impacted. In order to achieve this, an air pressure of 1.45 bar was used in the gun, giving the bullet a velocity of 25.5 m/s. Table 4.7 provides an overview of the impact parameters used. Since the end of the barrel was positioned very close to the sample to be impacted, deceleration due to aerodynamic drag is neglected.

$$E = \frac{1}{2} \cdot m \cdot v^2 \tag{4.1}$$

Table 4.7: Impact parameters

| Air pressure [$10^5$ Pa] | Bullet mass [gram] | Bullet velocity [m/s] | Bullet energy [J] |
|---|---|---|---|
| 1.45 | 30.7 | 25.5 | 10 |

It was found that the bullet velocity varied in practice, with the resulting impact energies lying between 9.06 J and 10.32 J, with the average being 9.82 J. Since the variation in bullet mass is low, it is likely that the variation in velocity was caused by the variation in the gap size between the inside of the barrel and the plastic bullet rear section. Other factors could include the accuracy of the gas gun pressure sensor, the consistency of the valve opening time or the accuracy of the velocity measurement apparatus.

The impact gun was aimed such that the bullet would hit the specimen 5-10 mm below the hole edge. There was some variation, as there was no way to align the gas gun with the sample precisely. Because of the safety device in place around the impact zone, horizontal aiming was easier, so the impact was never far from the longitudinal centre line of the specimen. The exact location of impact was typically visible, as some of the white paint broke off from the surface, exposing the black CFRP underneath. An example of this is seen in Figure 4.9. Also note the fatigue damage left and right of the hole. On the impacted back side of the specimen, typically a very slight indentation was observed with the naked eye, see Figure 4.10. This perturbation however is small enough to be almost certainly overlooked if the observer is unaware of the impact event and its location. In combination with the cracking seen on the other surface (which is often hidden from view in an aircraft structure) and the delaminated areas measured with C-scans, this damage is a typical example of BVID.

Figure 4.9: Impact damage on front of sample 40

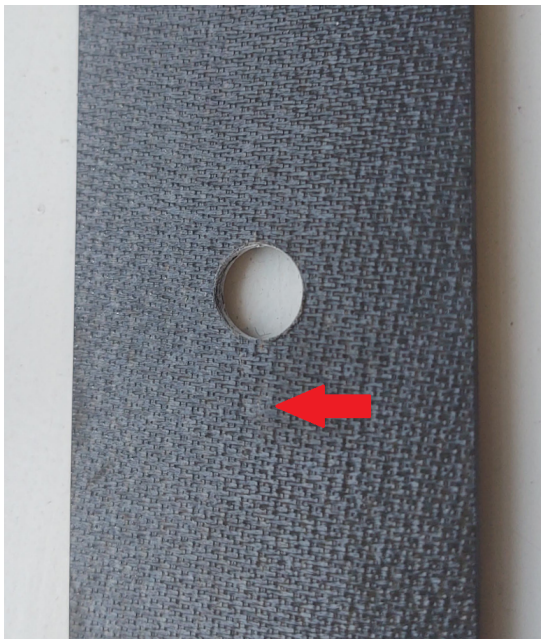

Figure 4.10: Impact damage on rear of sample 40

## 4.4. Measurement Parameters

Different types of measuring equipment were used. The MTS fatigue system measured the test time, displacement, force and number of fatigue cycles. A DIC system measured the surface deformations and strains, and is further explained in subsection 4.4.1. In addition, an acoustic emission measurement setup was used which is elaborated upon in subsection 4.4.2. Lastly, some samples were inspected using ultrasonic C-scan, which is explained in subsection 4.4.3. A general introduction of DIC and AE is provided in the previous chapter, in section 3.2.

### 4.4.1. Digital Image Correlation

A DIC measurement setup was used to track the surface strain of each specimen. Two Flir 5 MP cameras were used with a 50 mm lens, with a distance of about 800 mm from the specimen. Since the samples all had a central 10 mm hole, it was expected that this was the primary area where damage would occur. The field of view of the cameras was about 140 mm along the specimen, with the full sample width within the frame. In order to track the strain response during cyclic loading, VIC-Gauge software from Correlated Solutions was used. By tracking the deformation of the speckle pattern on the surface of the specimen, the software is able to calculate the displacements and strains. Three virtual extensometers were placed across the hole, all in vertical orientation as shown in Figure 4.11. The typical impact location is shown as well, in the form of a red dot below the hole. The central extensometer has a length of 40 mm, with the two outer extensometers having lengths of 25 mm. Care was taken to ensure that the extensometers were positioned parallel to the longitudinal specimen axis, and that the variation in extensometer length was low. This variation was typically below 0.5 mm. By taking the average value of the tensile strains measured by the extensometers, the strain response was tracked during fatigue cycling. With the increase of damage around the hole, the stiffness of the material decreases, thus the longitudinal displacement and strain increase during the load-controlled tests.

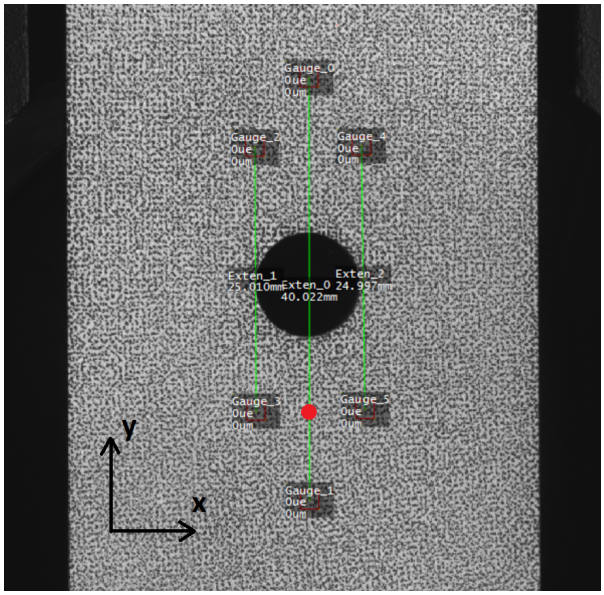


Figure 4.11: Virtual extensometer placement (green lines) and typical impact location (red dot)

The cameras took images with a frequency of 20 Hz, and for each image pair (one image from each camera) the variables including the average extensometer strain were written to a file. With a cyclic testing frequency of 10 Hz however, the system had difficulty keeping up and calculating the correct values for each image. Even if it did, there is the risk of aliasing, as only two image pairs would be taken per fatigue cycle. To avoid this, the fatigue program was paused and held at the maximum force for for an interval of 3 seconds every 500 cycles so that proper measurements could be taken, and a single image was saved during each interval. This method was used by Eleftheroglou [53] and is visualised in Figure 4.12. This interval was kept as short as possible; below 3 seconds the system was not always able to settle quickly enough and make correct strain measurements. At the start of a fatigue program, an imaging interval was initiated immediately, so a baseline measurement was taken before any cyclic loading was performed.

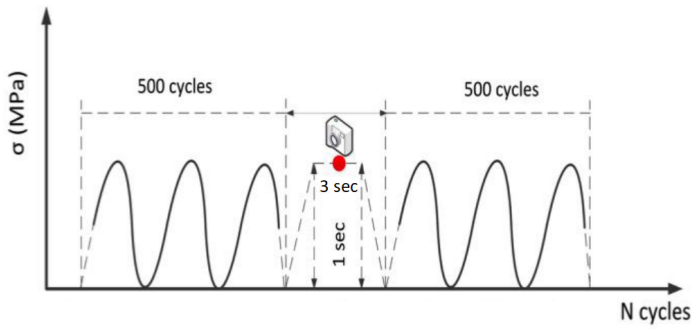


Figure 4.12: Method used to capture DIC images (adapted from Eleftheroglou [53])

When an imaging interval was initiated, a trigger signal was sent from the MTS machine to the VIC-Gauge system, so that the moment of these intervals was saved in the VIC-Gauge data for later post-processing purposes. It should be stressed here that while only one pair of photos is saved to the hard drive during this interval, all twenty images taken during this second are used to calculate the strains. Storing every image would take up excessive data. In total, typically 20-200 image pairs were saved for each specimen, which was sufficient for post-processing.

As mentioned in Subsection 4.3.2, the strain needs to be tracked real-time in order to use strain as a basis for pausing a fatigue test. The VIC-Gauge software can plot the measured data directly, but it is not able to filter out any data. Since the measured strain values outside of the imaging interval are incorrect, a custom program was written to filter out all values except during this interval (using the MTS trigger signal). This Python program continuously checks if new data measured within this imaging interval has been added to the VIC-Gauge file. If it sees new data, it adds the strain values to a plot. See Figure 4.13 for an example of such a strain tracking plot. Every red dot is the average strain measured during one imaging interval. Since measurements are taken with 20 Hz within the one second interval, the average of 20 values is taken. Each of these 20 values is represented by a blue dot. Since these are very close together, no individual dots can be distinguished. Note that each measurement point or blue dot in this case is the average strain in vertical direction of the three virtual strain gauges from Figure 4.11. The blue dots are plotted merely to check for scatter and outliers. Every averaged value (red dot) is divided by the first measured value to check the strain increase since the start. This increase is shown on the right axis as a fraction. Depending on the type of test performed, a horizontal green line was drawn either at 1.14 or 1.20 to indicate when a sample had reached a 14% or 20% strain increase. As soon as the first datapoint crossed this line, the fatigue program was manually paused using the MTS software. In case of 0% increase tests, the fatigue program was automatically paused directly after one image pair was taken.

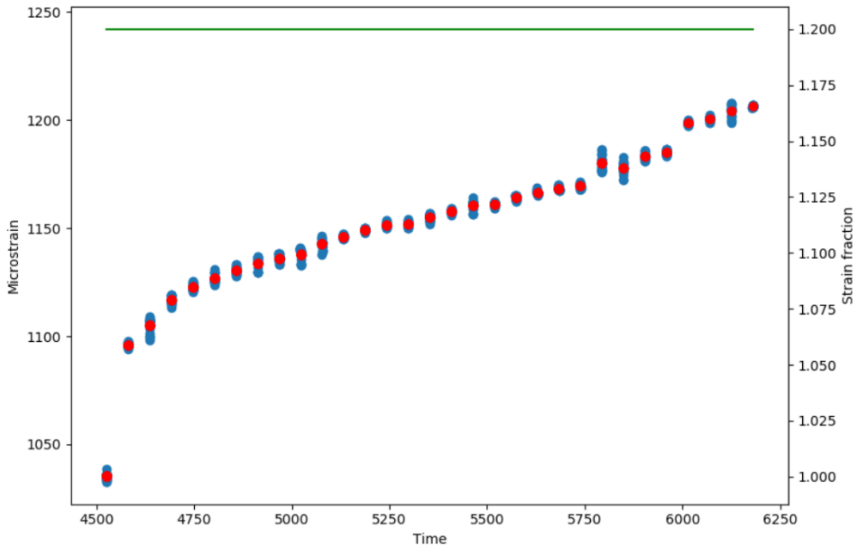


Figure 4.13: Example of the strain increase during testing

The sequence that is activated in the MTS program when the test is paused is shown in Figure 4.14. When this pause is initiated, the current fatigue cycle is completed until it reaches the lower fatigue limit (3.54 kN). Then the regular image capturing interval is initiated, after which the load is reduced to the mean load (19.5 kN). This is then held for about 9.5 minutes, during which time the sample can be impacted if required. This constant load section is displacement controlled instead of force controlled, to avoid the system suddenly changing the displacement as a reaction to a short peak of high tension due to impact. As soon as the test is continued using a button in the MTS software, another image pair is taken and a fatigue block of 500 cycles starts again.

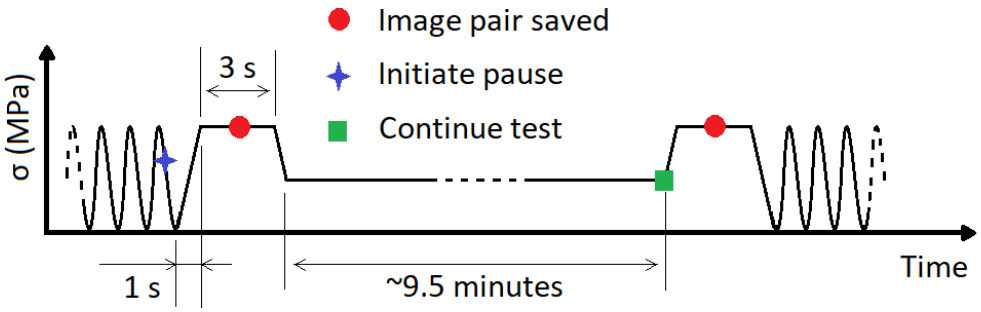


Figure 4.14: Pausing the fatigue test

The accuracy of the DIC setup used was checked for each specimen by taking several images before any load was applied. Comparing these images in post-processing shows the noise of the system. As an example, Figure 4.15 shows the surface strain error in longitudinal direction of sample 23. The noise error is between -93 and 100 $\mu\epsilon$, roughly an error of 200 $\mu\epsilon$ in total. With a first measured strain value typically in the order of 10'000 $\mu\epsilon$, a 2% error is deemed acceptable. The other samples checked for accuracy had very similar error levels.

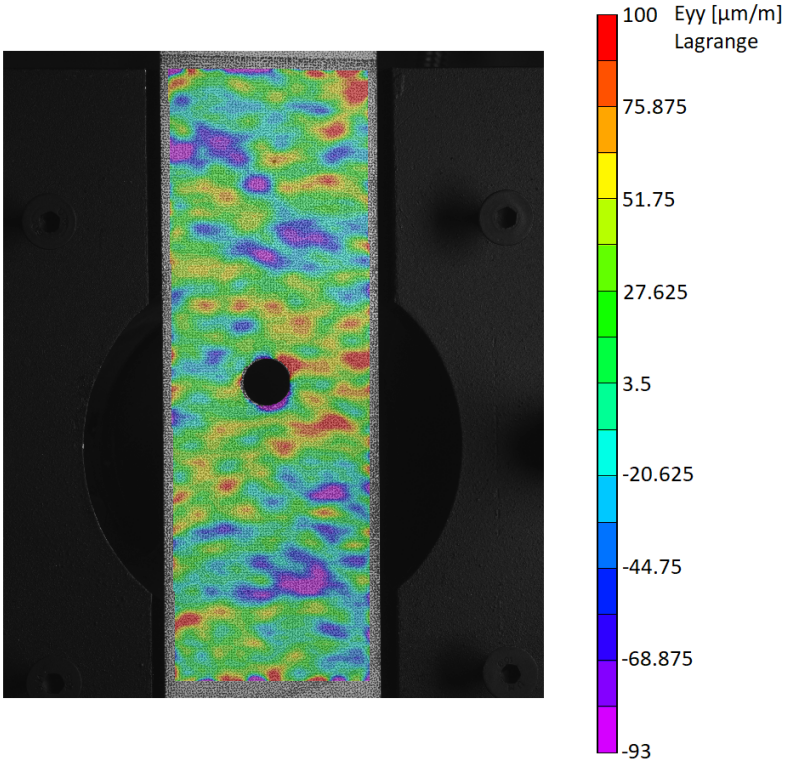


Figure 4.15: DIC error of specimen 23 in microstrain

### 4.4.2. Acoustic Emission

Next to the measurements performed by the DIC system, an AMSY-6 acoustic emission measurement setup from Vallen Systeme GmbH was used. Two Vallen VS900-M passive AE sensors were used with a frequency range of 100-900 kHz. The sensors were clamped onto the sample with coupling fluid to allow for good transmission of acoustic waves. Each sensor was wired to a preamplifier with a gain of 34 dB, before the signals were passed onto a data acquisition device. Instead of saving the complete waveforms, only its features were stored for post-processing to save storage space. The list of features saved is shown in Table 4.8. The system is linked to the MTS machine, so the force and displacement that the machine measures is stored in the AE data as well, in the form of PA0 and PA1.

Table 4.8: Acoustic emission features

| Feaure | Unit | Description |
|---|---|---|
| Channel | | On which channel (sensor) a signal is measured |
| Amplitude | dB | Peak amplitude of a signal (60-100 dB) |
| Rise time | $\mu$s | Signal rise time |
| Duration | $\mu$s | Signal duration |
| Counts | | Number of times the signal changes sign |
| Energy | eu | Signal energy |
| RMS | $\mu$V | Root mean square of background noise |
| PA0 | mV | External parameter 0 - force at time of measurement |
| PA1 | mV | External parameter 1 - displacement at time of measurement |
| Time | s | Measured with a resolution of 100 ns |

Not all the acoustic waves that hit the sensors come from damage events in a specimen. Sounds produced by the fatigue machine may transfer through the hydraulic grips into the sample, or signals

can reflect within the specimen. Since two AE sensors are used and the specimens are longitudinal in shape, a 1-D localisation algorithm is used to check if each signal originated from a location between the two sensors or not. In addition, the hits that were located to be further than 40 mm from the centre of the hole were filtered out as well to focus only on the central area. Figure 4.16 shows a typical hit distribution along the length of a sample. In this example, specimen 17 was used, which was impacted at 20% strain increase. It can be seen that the majority of the hits indeed originate from the central area of the sample, with some slight downward bias, likely because of the impact damage below the hole.

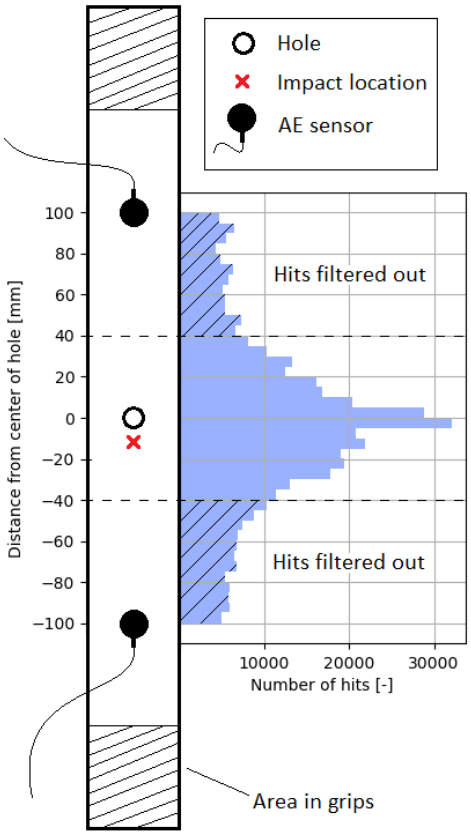


Figure 4.16: Typical AE hit distribution

The localisation works as follows. First, the wave velocity through a specimen is calculated. This can be done because every fatigue test was preceded by a pencil lead break test, whereby a signal is produced by breaking the tip of a mechanical pencil on the surface of the specimen. If this is done either above the top sensor or below the bottom sensor, the time difference between the measured hits can be used to calculate the wave velocity. The velocity in this case was about 5640 m/s. When the velocity is known, an 'area of interest' can be established, in this case 80 mm (40 mm below and above the centre of the hole). Equation 4.2 is then used to calculate the maximum allowed time difference between a signal being picked up by both sensors. For every two signals measured, it is checked if both signals are picked up by a different sensor, and if the measurement times comply with Equation 4.3. Only these hits will then be used for further processing and visualisation. Typically only 30% of the original number of hits were left after applying the localisation filter. In order to create the histogram in Figure 4.16, Equation 4.4 was used to calculate the actual distance from the centre of the sample. Note that in order to plot this histogram, the area of interest was set to 200 mm.

$$\Delta t_{max} = \frac{Area\ of\ interest}{v} \tag{4.2}$$

$$|t_1 - t_2| < \Delta t_{max} \tag{4.3}$$

$$Distance\ from\ center = \frac{1}{2} v(t_1 - t_2) \tag{4.4}$$

A few considerations have to be kept in mind when using the localisation algorithm described above. First of all, it is a 1-D algorithm, whereas the specimen has a more or less 2D shape (thickness is negligible). It is assumed however that the length is sufficiently larger than the width so the error is not too large. Secondly, it is possible to get false positives. When two acoustic waves each enter one sensor from the 'outside' (the hydraulic grip direction) within a short time frame, they will be mistakenly assumed to come from the central area of the specimen instead. However, the system typically measured 500 - 1000 hits per seconds, meaning that on average the time difference between two signals is 1-2 ms. The maximum time difference for two signals to pass the localisation filter is about 0.014 ms. It is therefore not expected that the number of false positives represents a significant fraction of the localised hits. A third consideration is that the wave speed is measured with a pencil lead break test before any damage is present in the material. As soon as damage starts to occur, the structure essentially changes, and the wave speed through this damaged area is likely to change as well. However, characterising acoustic wave velocities through samples with varying degrees of damage would require a study on itself. It is assumed that the approximation suffices. Lastly, it is emphasised again that the acoustic sensors were removed before any impact took place, in order to avoid damaging the sensors. Therefore, the AE data includes only damage due to fatigue while the full damage state of an impacted sample includes damage due to impact as well.

### 4.4.3. Ultrasonic C-scan

In addition to the specimens that were tested to failure, ten samples were tested up to a certain point, after which they were C-scanned. This was perfomed at GTM Advanced Structures in The Hague. The images produces are black and white, without differentiation between the various plies. While the resolution is not great (about 0.55 mm per pixel), the contrast is good, and a clear boundary between the delaminated and intact area is seen.

In addition, a hand scanner was used obtain information about the positions of the delaminated areas through the thickness. An Olympus RollerFORM phased array wheel probe was used in combination with an Olympus OmniScan SX acquisition and display device. While coloured images with depth differentiation were produced, high quality was not achieved after trying a range of settings. An example of the area around the hole as scanned by both methods is provided in Figure 4.17. Section 5.1 further discusses the use and implications of the C-scan results.

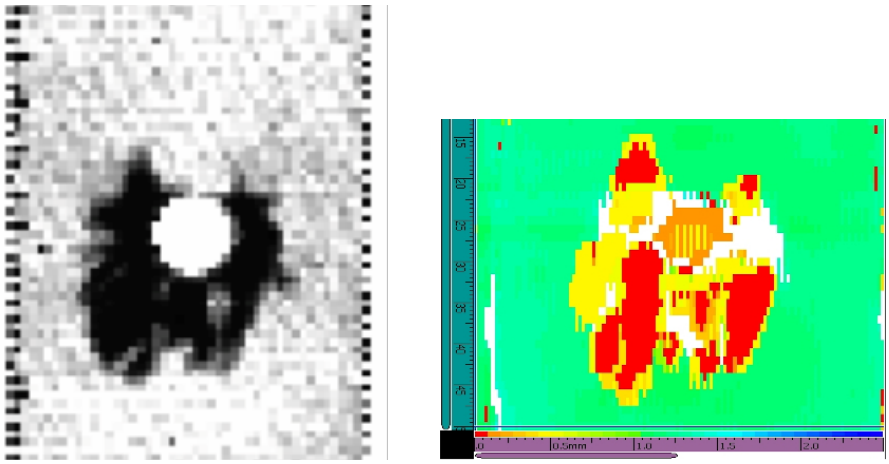

(a) Scanned at GTM

(b) Scanned using hand scanner

Figure 4.17: Examples of C-scans (both specimen 28)

# 5

# Results

This chapter presents the results of the tests performed as explained in chapter 4. This chapter is divided into six sections. First, section 5.1 presents some general observations. Afterwards, the results of the specimens that were fatigue loaded without any impact are shown in section 5.2. The results for the tests paused at the 0%, 14% and 20% strain thresholds are then introduced in sections 5.3, 5.4 and 5.5 respectively. Finally, these results are analysed and compared in section 5.6. Note that the visualisations presented in this chapter are believed to provide all the relevant information on which the conclusions are based. More attempts were made at filtering or visualising the data differently in various ways, but this did not provide relevant extra information.

## 5.1. General Observations

This section details the general observations and results. First of all, an overview of the different test types is presented in Table 5.1, with the average number of cycles it took before the strain threshold was reached, as well as the average fatigue life. For each of the seven test types, three samples were tested.

Table 5.1: Pause moment and mean fatigue life per test type

| **Sample paused at** Strain increase [%] | **Impact** | **Mean cycles to pause** $[10^3]$ | **Mean fatigue life** $[10^3]$ |
|---|---|---|---|
| No pause | No | - | 34.7 |
| 0 | No | 0 | 81.7 |
| 0 | Yes | 0 | 16.0 |
| 14 | No | 13.2 | 66.9 |
| 14 | Yes | 13.5 | 67.2 |
| 20 | No | 22.7 | 41.7 |
| 20 | Yes | 29.2 | 52.2 |

It should be reiterated that when strain percentages are discussed, an increase of longitudinal surface strain with respect to the first measured value of a sample is meant. Throughout this chapter, graphs are shown with the strain increase of samples over their fatigue life. These are always normalised and start at 0%. This normalisation is deemed acceptable since the first measured values were very similar. The average value encountered was 10060 $\mu\epsilon$ (about 0.01 mm/mm) with a standard deviation of 220 $\mu\epsilon$. Note that the estimated measurement error is 200 $\mu\epsilon$, see section 4.4.

All the tested specimens failed in very similar ways. As expected, damage initiated left and right of the central hole which propagated until fracture. Figure 5.1 shows an example of what a static failure looks like. The material fails at a 45 degree angle, with some fibre pull out. Figure 5.2 shows what a typical fatigue specimen looks like after failure. Much more delamination damage and fibre pull out is seen here. The fracture still mostly follows a +/- 45 degree angle, with long 0 degree fibres completely pulled out. The delaminations typically ran along the full length, up to the hydraulic grips in which the sample was clamped.

Figure 5.1: Typical static failure (sample 16)

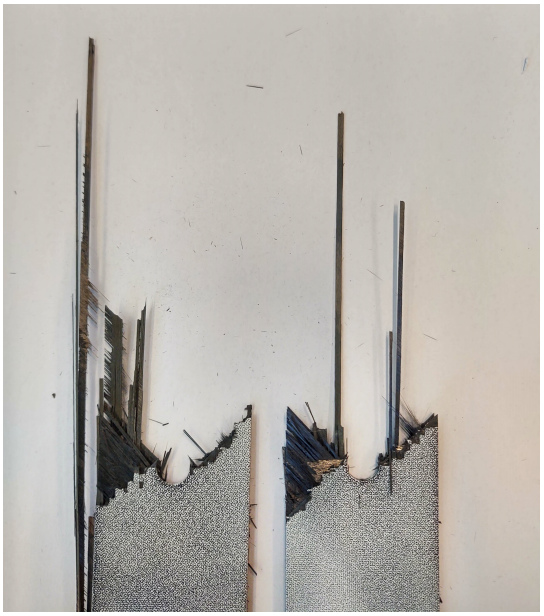

Figure 5.2: Typical fatigue failure (sample 14)

As discussed in Subsection 4.4.3, two methods of ultrasonic C-scanning were used. Figures 5.3 and 5.4 show both scans for specimens 37 and 21 respectively. The first sample was only fatigue loaded, while the latter was impacted as well. Both were stopped at 20% strain increase. It was hoped that the coloured images would provide additional information about the specific ply interfaces that were delaminated. However, the included depth scale indicates the laminate thickness to be roughly 1-1.25 mm, with the yellow areas being at a depth of roughly 0.5 mm and the red areas being near the top surface, at 0.1 mm or less. With an actual specimen thickness of 2 mm, this does not make much sense. In addition, large areas in the image are white, where no data was collected. The hole centre shows a variation of colours, but since no direct contact with the probe is made at that location, an erroneous measurement is expected.

This suggests that the quality is not high enough for these images to be used for further analysis. The only thing that is consistently observed is that the locations at 45 degree angles to the hole typically show red, whereas the other delaminated regions show yellow or orange. Although speculative, this may lead to a conclusion that these areas (which are in compression according to the DIC images) have a delaminations closer to the surface, with the surrounding areas having delaminations closer to the centre of the specimens. Since this is a general observation, the rest of the results will only show the black and white scans, as this data is complete and shows good contrast. For reference, all C-scan results, including the coloured ones, are shown in Appendix A.

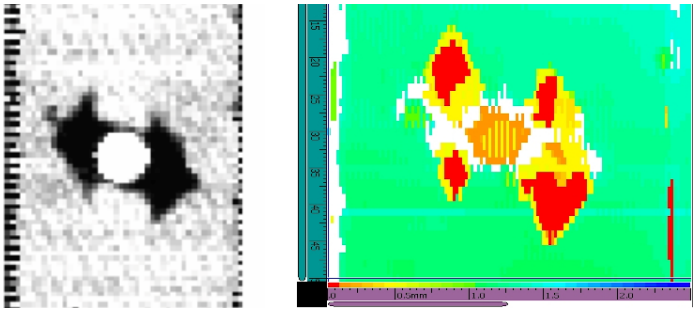

(a) Scanned at GTM (b) Scanned using hand scanner

Figure 5.3: C-scans of specimen 37 (only fatigue)

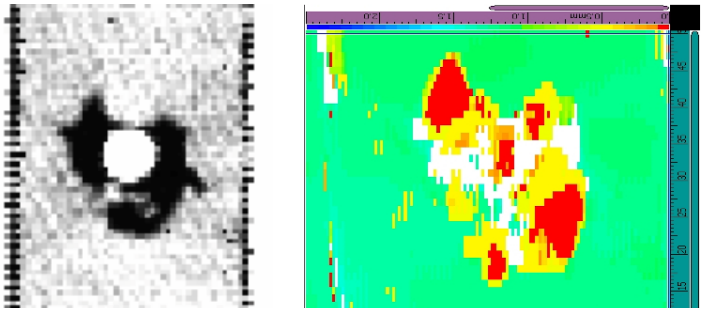

(a) Scanned at GTM (b) Scanned using hand scanner

Figure 5.4: C-scans of specimen 21 (fatigue and impact)

Of the features measured by the acoustic emission (AE) system, only the energy release and number of hits are used for further analysis. The features are often related to each other, for example a signal with a high energy release is also likely to have a long duration. While data-driven models may extract useful information from comparing these individual features, no clear relations were found by manual interpretation of the data. Various visualisation styles were experimented with to find any trends. Note that the channel, amplitude, force and time features were used to localise and filter the data and to display the data versus the number of fatigue cycles instead of time.

Since different damage mechanisms generate different acoustic signals, the data was filtered in an attempt to characterise the damage better. As discussed in subsection 3.2.2 in the SHM chapter, research suggests that fibre fracture typically produces signals above 80 dB, whereas matrix dominated failure modes produce signals with a lower amplitude. Note that with a lower threshold of 60 dB set in the AE settings, some of the smaller matrix-dominated damage events are not captured. Before the unfiltered graphs with the cumulative energy release and number of hits are presented for the individual test types, some data is shown that is filtered at an amplitude of 80 dB. Since the observations regarding this filtering are very similar for the 0%, 14% and 20% test types, only the 14% graphs are shown as an example. An overview of all the filtered and unfiltered graphs for the three test types can be found in Appendix B. Keep in mind that the filtering is something entirely separate from the localisation algorithm, which is used on all data sets.

Figure 5.5 (a) shows the total cumulative energy release of the samples. Figures (b) and (c) show the energy release graphs with all hits in the 60-80 dB amplitude range and 80-100 dB amplitude range respectively. Note that the sum of both graphs equals Figure (a). It is observed that the energy released in both filtered cases are in similar order of magnitude. Figure (b) however is much smoother than Figure (c). Figure 5.6 (a) shows the total number of hits measured over the fatigue lives of the samples. Again, figures (b) and (c) show both filtered data sets. While image (b) is again much smoother than (c), the total number of counted hits is about two orders of magnitude larger as well. As a matter of fact, Figure (b) is almost the same as Figure (a). This shows that the higher amplitude hits occur less frequently, but their energy is much higher, and in the end they make up for about half of the total released energy. This makes intuitive sense in accordance with the ragged jumps seen in Figure 5.5

(c). It is interesting to note that the final failure of a sample consists mostly out of fibre fracture, and the high amplitude hits cause an near vertical increase in the energy release right before failure. Therefore, it is indeed likely that these high amplitude hits typically represent fibre fracture events.

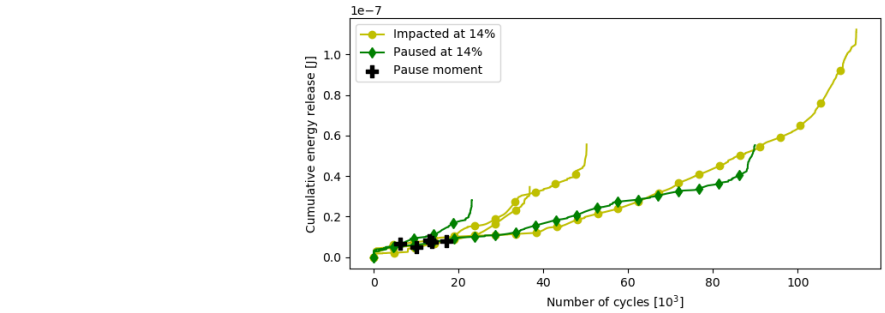


(a) 60-100 dB

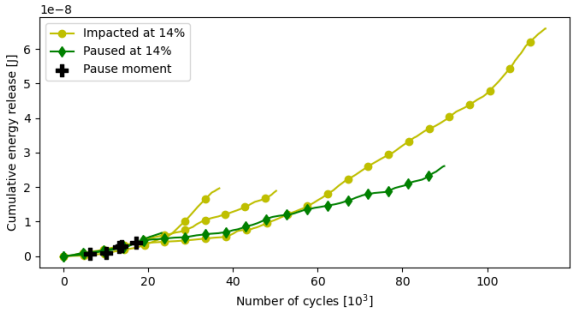


(b) 60-80 dB

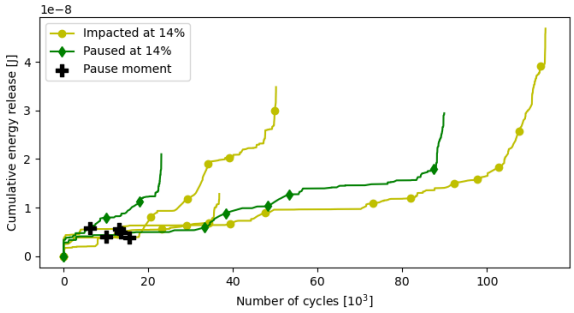


(c) 80-100 dB

Figure 5.5: Filtered cumulative energy release of 14% samples

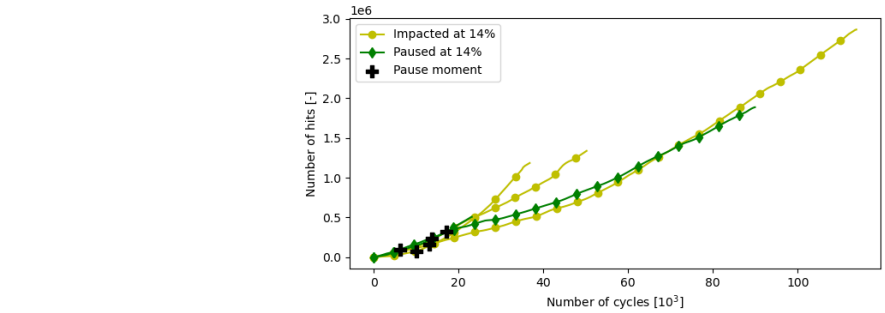


(a) 60-100 dB

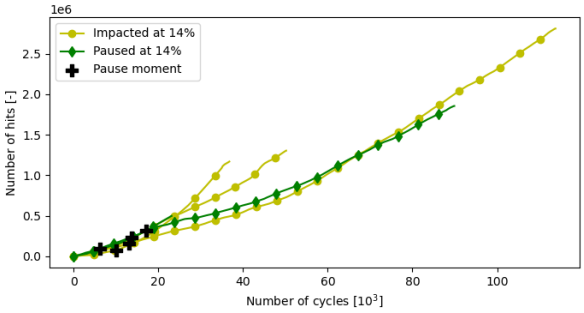


(b) 60-80 dB

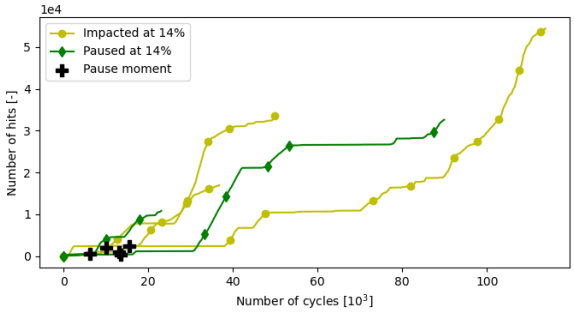


(c) 80-100 dB

Figure 5.6: Filtered hits of 14% samples

## 5.2. Fatigue Only

In order for an impact to take place, the relevant fatigue tests were paused for 9.5 minutes at a load of 19.5 kN, or 0.44% of the UTS. The pause time was chosen because this was the time it took to safely impact the structure before continuing the fatigue test. Because of this interruption of the fatigue program, two independent variables were changed: if and when a fatigue test was paused, and whether or not impact takes place during this pause. In order to say anything meaningful about the effect of an impact, the effect of only pausing the test at various times has to be examined. Three samples were not paused (pure fatigue test), and the other 9 were paused at 0%, 14% and 20% strain thresholds respectively. Table 5.2 shows the fatigue life of every sample that was not impacted. A difference is observed between the mean fatigue lives of each test type. The fatigue life of the samples paused immediately at the start (0% strain increase) is on average more than twice as long as that of the uninterrupted specimens. Performing an ANOVA test on these two sets of samples, a P-value of 0.058 is attained, slightly higher than the often used significance threshold of 0.05. If the interruption indeed has an effect, it is likely that any influence of this pause has less of an effect the later a specimen is paused. This seems to be true, as the mean fatigue life of the 20% samples is shorter than that of the 14% samples, which in turn has a shorter fatigue life than the 0% samples. Due to the nature of fatigue testing, the amount of variation within groups - scatter - is quite large. Also, because testing many more samples would be costly and time consuming, the number of tests per group was limited to three. Therefore, the differences between the 14% and 'no pause' specimens and between the 20% and 'no pause' specimens are far from being statistically significant.

Table 5.2: Thresholds and fatigue lives of all specimens that are not impacted

| **Sample** | **Paused at** Strain increase [%] | **Paused at** Cycles [$10^3$] | **Mean paused** Cycles [$10^3$] | **Fatigue life** Cycles [$10^3$] | **Mean fatigue life** Cycles [$10^3$] |
|---|---|---|---|---|---|
| 46 | No pause | - | - | 29.4 | 34.7 |
| 10 | | - | | 37.7 | |
| 18 | | - | | 37.0 | |
| 43 | 0 | 0 | 0 | 54.3 | 81.7 |
| 14 | | 0 | | 76.3 | |
| 39 | | 0 | | 114.6 | |
| 22 | 14 | 13.7 | 13.2 | 90.2 | 66.9 |
| 34 | | 6.1 | | 23.2 | |
| 45 | | 19.7 | | 87.2 | |
| 23 | 20 | 41.2 | 22.7 | 72.6 | 41.7 |
| 11 | | 16.2 | | 29.5 | |
| 31 | | 10.6 | | 23.0 | |

Figure 5.7 shows the strain increase of the samples. It is immediately clear that there is a lot of random variation. It can be observed however that all specimens follow an S-shape in terms of strain increase. They typically follow a pattern where initial strain increases quickly until about 8-10%, after which the increase slows down to an almost linear path. After about 25-30% increase, it starts to speed up again and critical failure is imminent. Note that a strain increase of 25% means that the local stiffness in the measured area has dropped to 80% with respect to the first measurement.

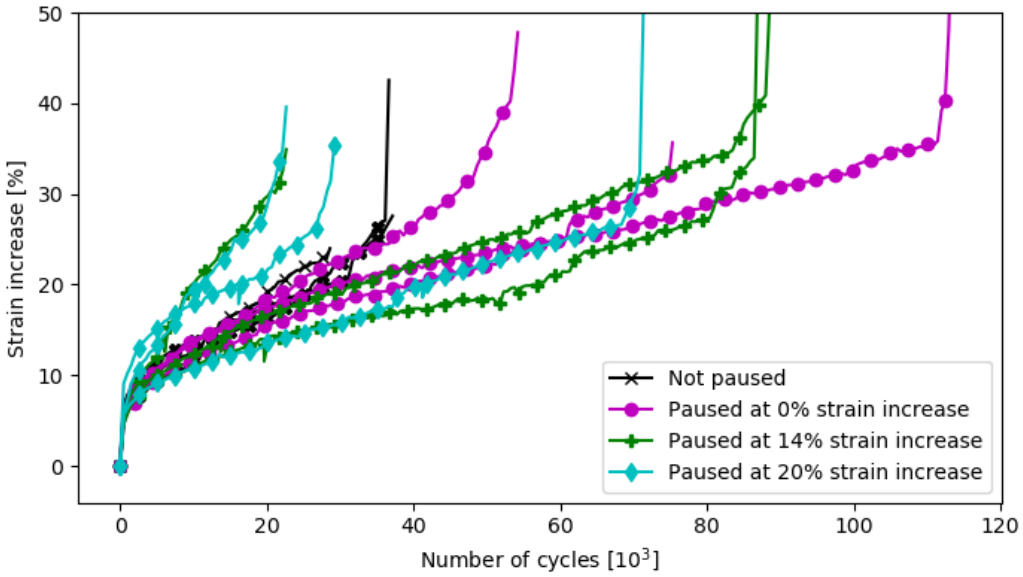


Figure 5.7: Strain plots of samples that are not impacted

Unfortunately, incorrect settings were accidentally used for the AE measurements of the 'not paused' samples. Mainly, a significantly longer rearm time was set. This means that after a hit was registered, it took a longer time before the next hit could be measured. Significantly fewer hits were therefore measured, with a lower total energy release. Showing the data of the paused specimens here was deemed irrelevant, as no interesting trends were seen. The graphs of all the paused samples are shown in the subsequent sections, albeit not in the same figure.

Figure 5.8 shows two samples that were fatigue loaded up to a strain increase of 20%. Specimen (a) was paused at 0% directly at the start, after which it was loaded until the 20% threshold was reached. Specimen (b) was first fatigued until 20%, after which it was paused and stopped. Both images look similar in terms of delamination area and shape, indicating that the moment at which a fatigue program is interrupted does not have an effect on the delamination patterns. The similarity between these images also supports the idea that the damage state corresponds well to the measured strain increase level. Looking at table 5.2, the expected fatigue lives of these specimens may well be very different, with the expected fatigue life of a sample paused at 0% being nearly twice as long as the life of the sample paused at 20%. As stated before however, the spread within these groups weakens that idea.

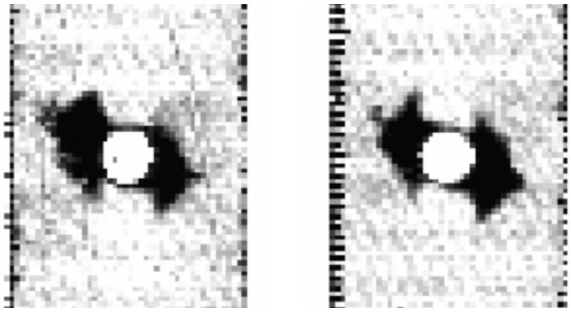

(a) Paused at 0% (specimen 29) (b) Paused at 20% (specimen 37)

Figure 5.8: C-scans of specimens fatigued to 20% without impact

## 5.3. paused at 0% strain increase

The results of the specimens that were paused right at the beginning of the fatigue program show clear differences in fatigue life. Table 5.3 shows that the samples that are impacted have, on average, a more than five times shorter fatigue life. Using an ANOVA test, it was found that this is statistically significant with a P-value of 0.024.

Table 5.3: Fatigue lives of samples paused at the start of the test

| **Sample** | **Impact** | **Fatigue life** cycles $[10^3]$ | **Mean life** Cycles $[10^3]$ |
|---|---|---|---|
| 43 | No | 54.3 | 81.7 |
| 14 | | 76.3 | |
| 39 | | 114.6 | |
| 42 | Yes | 8.8 | 16.0 |
| 30 | | 10.9 | |
| 25 | | 28.3 | |

Figure 5.9 shows the difference in strain increase for the 0% samples. Note that some paint chipped off of specimen 25 during the impact which compromised one of the virtual extensometers. No local strain data was therefore collected, so a dashed line is drawn at the failure point of this sample. It is clear from the graph that the impacted specimens accumulate damage much faster than the samples that are merely paused. There is however not much difference in final failure strain values.

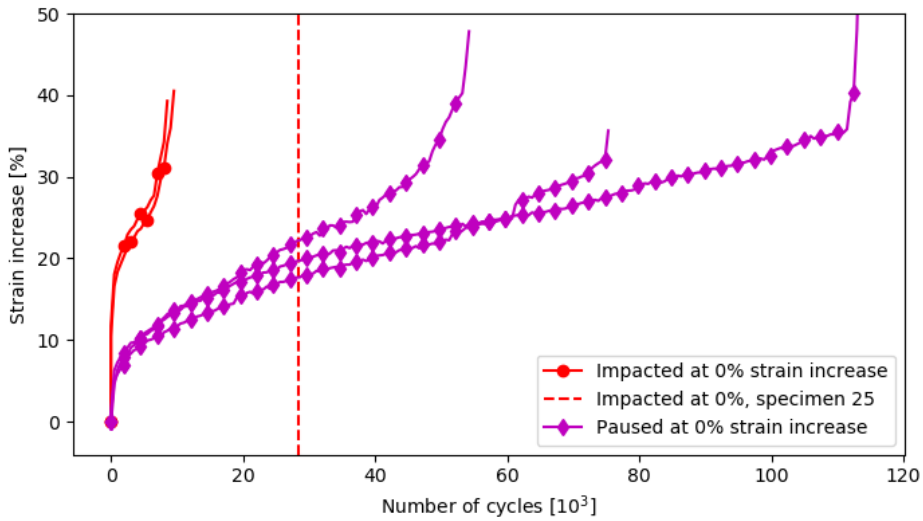


Figure 5.9: Strain plots of samples paused at 0%

Figure 5.10 shows the cumulative AE energy released. Remember that the sensors were removed for the impact, so technically not all of the energy release was measured. The shapes of the graphs are not too different from the strain plots shown in Figure 5.9, albeit a bit less smooth, and they exhibit less of an S-shape. Figure 5.11 shows the progression of the number of AE hits measured. These plots are more or less straight, indicating a roughly constant number of hits measured per fatigue cycle.

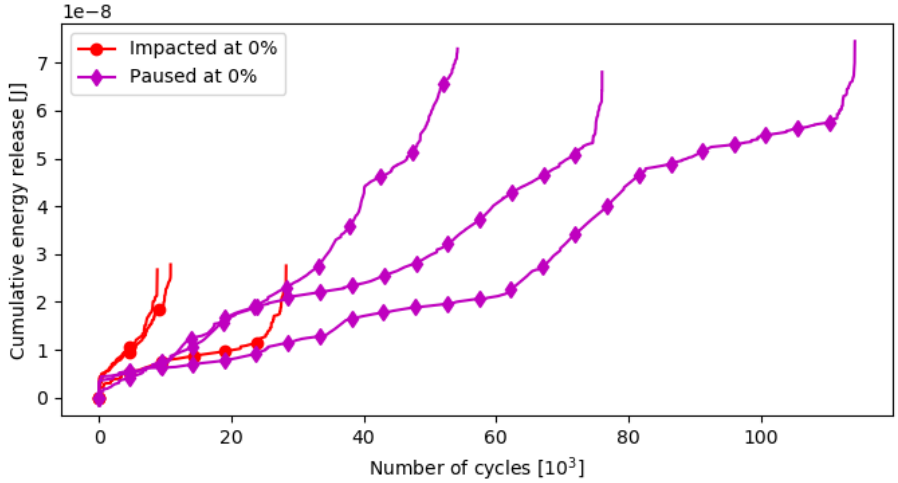


Figure 5.10: Cumulative energy plots of samples paused at 0%

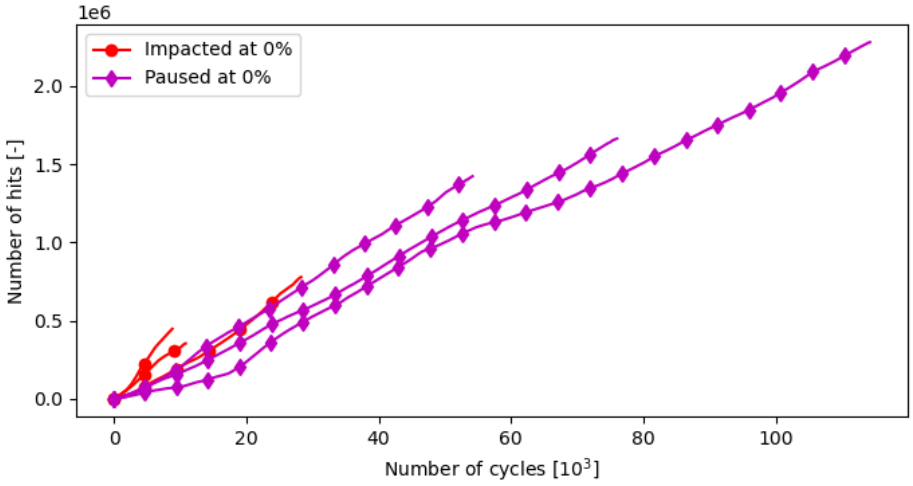


Figure 5.11: Cumulative number of hits of samples paused at 0%

Since the impacted specimens failed so soon, it is useful to zoom into the bottom left corners of Figures 5.10 and 5.11 and see the difference between the specimens right after the pause moment. Figures 5.12 and 5.13 show the cumulative energy release and number of hits respectively for the first 5000 fatigue cycles. This paints a clear picture: both the energy released and the number of hits increase much more rapidly for the impacted samples.

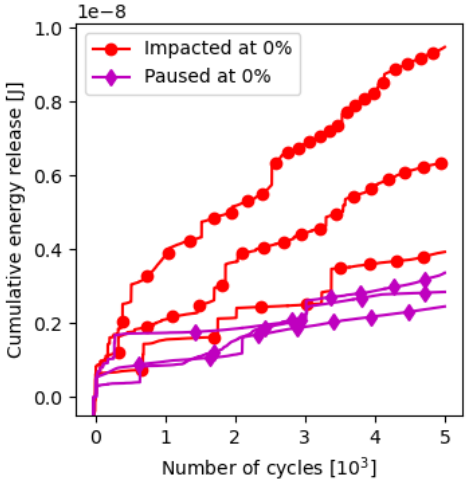


Figure 5.12: Cumulative energy release over first 5000 cycles

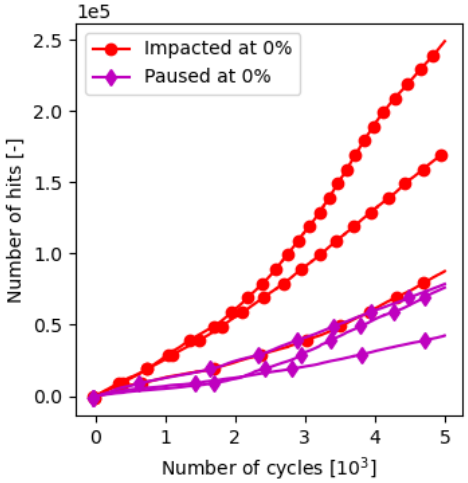


Figure 5.13: Cumulative number of hits over first 5000 cycles

Now that it is clear that there is a significant difference between the paused and impacted samples, taking a look at qualitative data may shed some light on why this is the case. Figure 5.14 shows the longitudinal surface strain field of two samples as measured by the DIC setup. The top two images show a sample right before and after pause (without impact), and the bottom images show a sample right before and after impact. Note that the first images already show some cracking next to the hole. This is because the specimen needs to be loaded to the maximum fatigue load in order to take a DIC image pair. The structure essentially undergoes one fatigue cycle before the pause is initiated. The top specimen does not show much difference, it is actually difficult to see any difference with the naked eye at all. The bottom images clearly show the point of impact: some paint chipped away and a low stress region appears. This makes sense, as damage in this area will make the material locally less stiff, meaning that it attracts less load. More interestingly, an increase in damage is seen next to the hole, primarily on the left side. The visible crack increased in length and the stress distribution changed after impact.

Figure 5.15 shows the transverse surface strain fields of a paused and impacted specimen. Again, the paused specimen on the top does not show any difference. The impacted sample however shows a significantly different strain field. The area on the bottom edge of the hole is relieved of its high compressive strain, and the blue/purple area with high compressive strain to the bottom left of the hole did not only increase after impact, but it changed shape as well. The triangular shape with one edge along the length of the specimen and the other two edges on a +/- 45 degree angle likely indicate a delaminated area underneath. Since this particular specimen was not inspected using C-scan, this is not verified.

For reference, one example of the strain evolution throughout the fatigue life of a specimen is provided in appendix C. The strain is shown of a sample that is impacted at 14% strain increase at intervals of roughly 2’500 cycles.

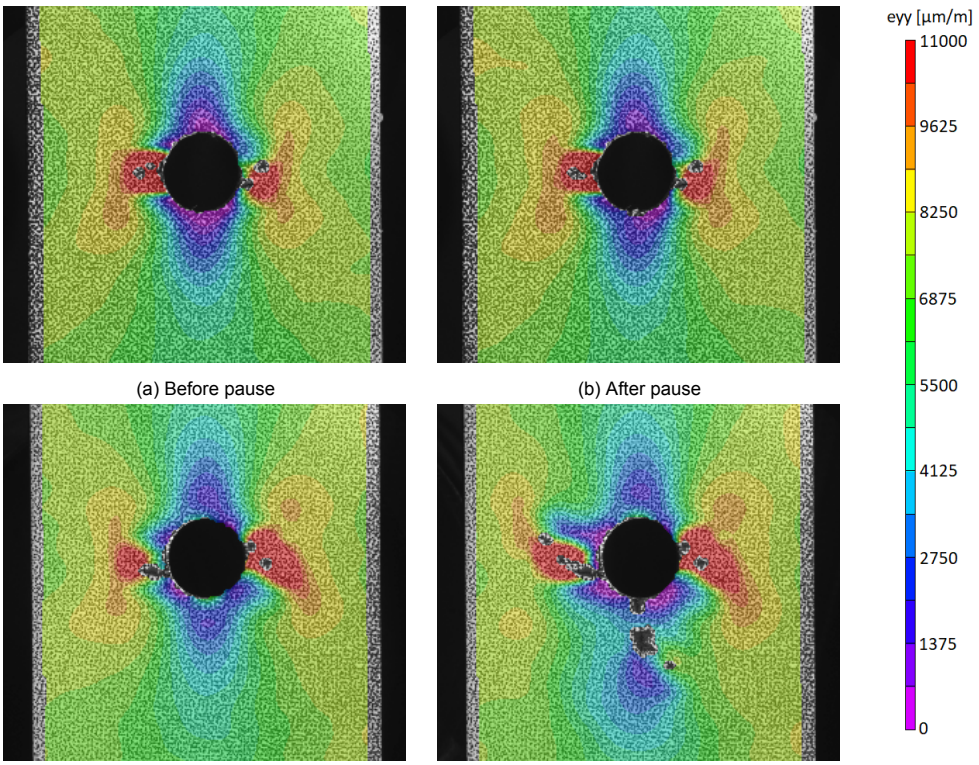


(a) Before pause (b) After pause

(c) Before impact (d) After impact

Figure 5.14: Longitudinal surface strain ($\epsilon_Y$) of samples paused (top, specimen 14) and impacted (bottom, specimen 30) after 0% longitudinal strain increase

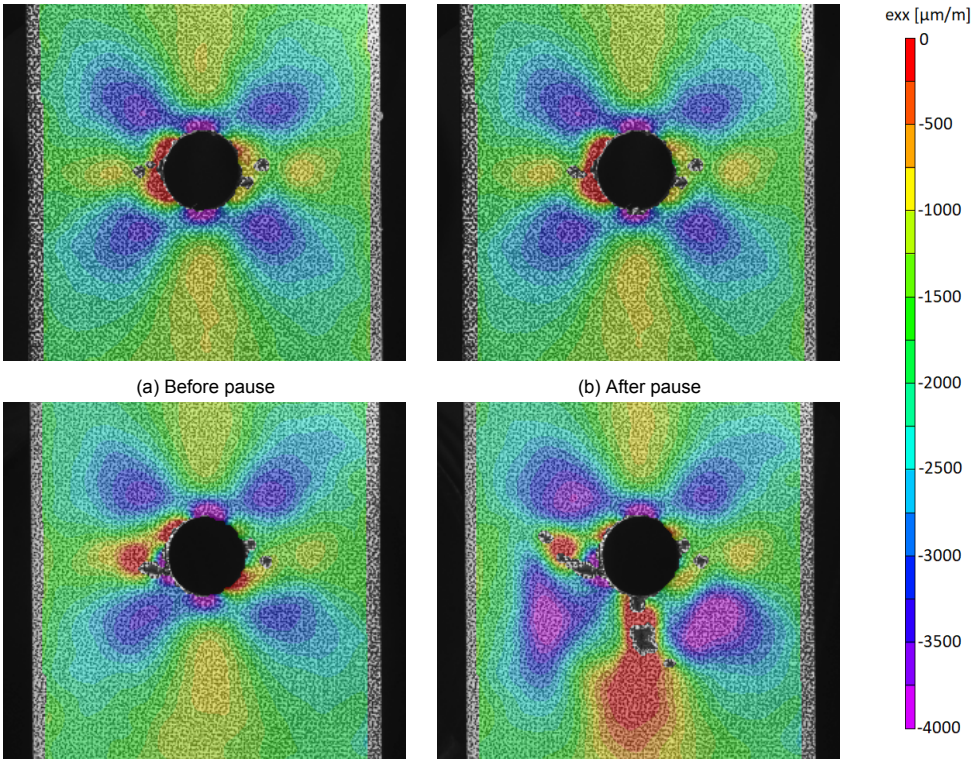


(a) Before pause (b) After pause

(c) Before impact (d) After impact

Figure 5.15: Transverse surface strain ($\epsilon_X$) of samples paused (top, specimen 14) and impacted (bottom, specimen 30) after 0% longitudinal strain increase

The C-scan results of the samples paused at the start of the fatigue test are presented in Figure 5.16. Image (a) shows a specimen after only the pause moment. Only a little bit of damage is observed left and right of the hole, as a result of the single loading cycle that was necessary to take a DIC image pair before the pause. Images (b) and (c) are both impacted during the pause, and then stopped. A clear, more or less triangular delaminated area can be seen directly around the point of impact below the hole. What is interesting here is that the impact also causes significant damage on one side of the hole. This is in line with the observations made in the DIC images. Images (d) and (e) show specimens that were fatigued to 20% after a pause at 0% and an impact at 0% respectively. The delaminated areas left and right of the hole are similar, the main difference is the delaminated area due to the impact below the hole.

(a) Stopped after pause (specimen 12)

(b) Stopped after impact (specimen 49)

(c) Stopped after impact (specimen 19)

(d) Continued to 20% after pause (specimen 29)

(e) Continued to 20% after impact (specimen 21)

Figure 5.16: C-scans of specimens paused at 0% strain increase

## 5.4. Paused at 14% Strain Increase

Table 5.4 shows the number of cycles until the pause moment and until failure for the samples that were paused at 14% strain increase. It is clear that the variation between samples is large, even though the average values for the impacted and 'paused only' specimens are almost the same. Based on these numbers alone, there is no difference between the two test sets.

Table 5.4: Number of cycles to threshold and fatigue life of 14% samples

| Sample | Impact | Paused at Cycles $[10^3]$ | Mean paused Cycles $[10^3]$ | Fatigue life Cycles $[10^3]$ | Mean fatigue life Cycles $[10^3]$ |
|---|---|---|---|---|---|
| 22 | No | 13.7 | 13.2 | 90.2 | 66.9 |
| 34 | | 6.1 | | 23.2 | |
| 45 | | 19.7 | | 87.2 | |
| 24 | Yes | 13.1 | 13.5 | 114.2 | 67.2 |
| 41 | | 10.1 | | 36.9 | |
| 44 | | 17.1 | | 50.4 | |

Figure 5.17 shows the longitudinal strain increase versus the number of fatigue cycles for the specimens paused at 14%. The horizontal dashed line indicates the moment where the samples were paused. One of the paused specimens has a noticeably faster strain increase than the others. Also, it looks like the impacted specimens have a slight jump in strain after impact, after which the strain increase is similar to the other samples again. Aside from this, the strain progression path is similar for all specimens.

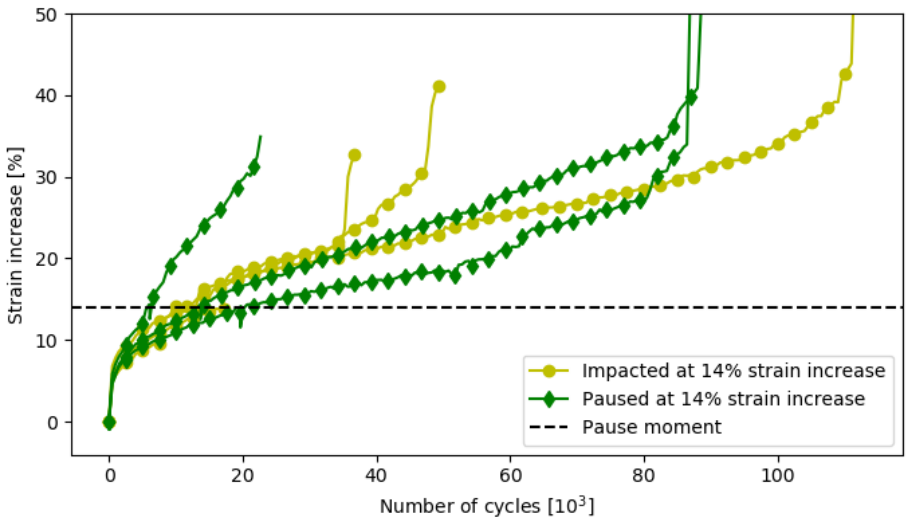


Figure 5.17: Strain plots of samples paused at 14%

The cumulative energy release and number of hits, both measured by the AE system, are shown in Figures 5.18 and 5.19 respectively. Unfortunately the measurement of one of the paused samples stopped for unknown reasons at some point when the test was still running, so that data is left out. It is unclear why that happened. Just as with the strain measurement, these graphs don't seem to show a difference between the paused and impacted specimens. One thing that can be noted is that after the pause moment, the specimens (also the impacted ones) accumulate hits slower than before the hold. It seems the number of hits per fatigue cycle reduces directly after the pause, before it slowly increases again.

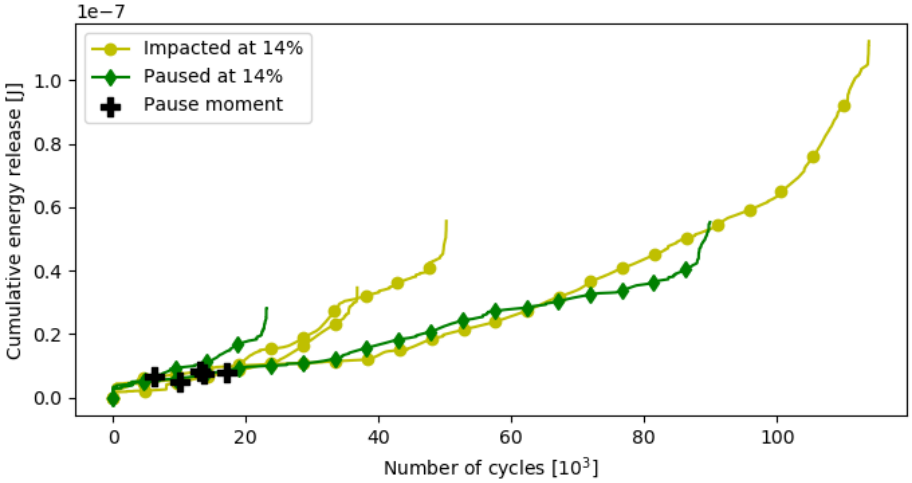


Figure 5.18: Cumulative energy plots of samples paused at 14%

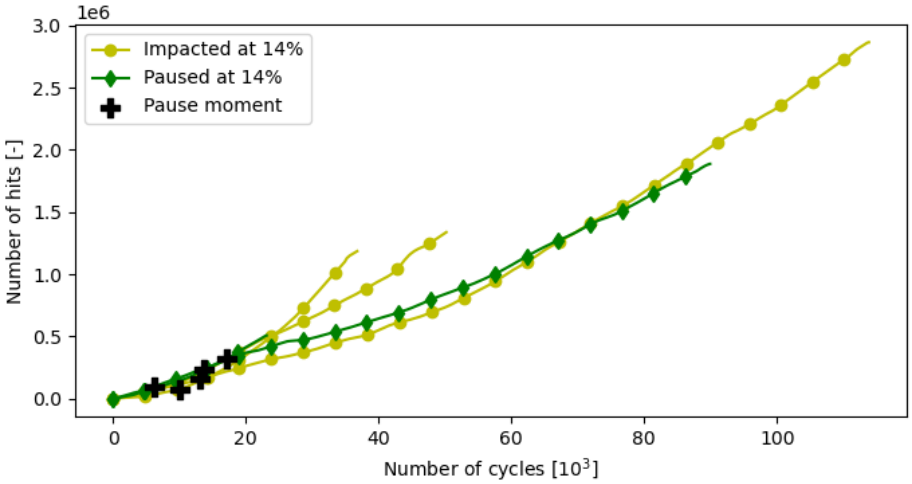


Figure 5.19: Cumulative number of AE hits of samples paused at 14%

The surface strain fields of a paused sample (top) and an impacted sample (bottom) is shown in Figure 5.20. The top two images show a sample right before and after pause (without impact), and the bottom images show a sample right before and after impact. As with the 0% case discussed in the previous section, the last image before and the first image after pause are shown. The top row does not show any differences, as expected. The bottom row clearly shows the impact location where the paint chipped away. However, there seems to be little effect on the strain next to the hole. A tiny speck can be seen where some paint chipped off to the left of the hole, but the actual strain distribution shows, if anything, a slight decrease in strain values.

The transverse surface strains shown in Figure 5.21 tell a similar story. Not much difference is observed, aside from the impact area itself and a decrease in compressive strain on the bottom left edge of the hole. It appears that unlike the 0% case, the impact event does not noticeably influence the damage already present next to the hole due to fatigue. Although the total damaged area has increased due to impact, this new added damage is not within the critical damage path leading up to failure. It therefore seems that the impact does not influence the fatigue life. This is supported by the graphs shown earlier, where no difference between impact and no impact is observed, other than a small jump in strain after impact.

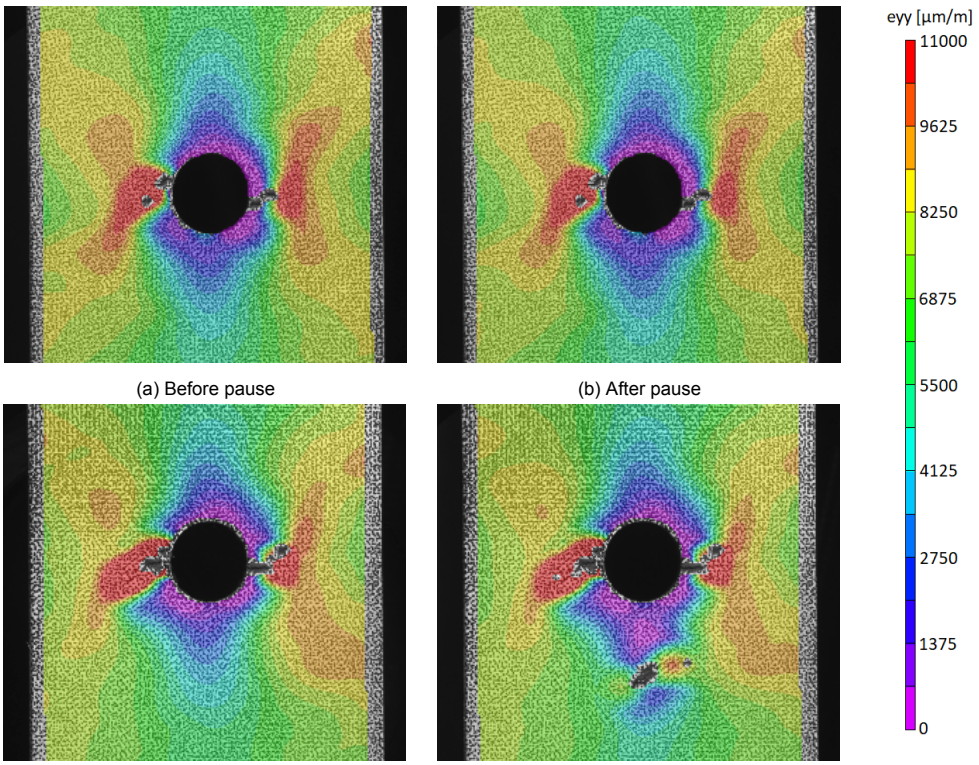


(a) Before pause (b) After pause

(c) Before impact (d) After impact

Figure 5.20: Longitudinal surface strain ($\epsilon_Y$) of samples paused (top, specimen 45) and impacted (bottom, specimen 41) after 14% longitudinal strain increase

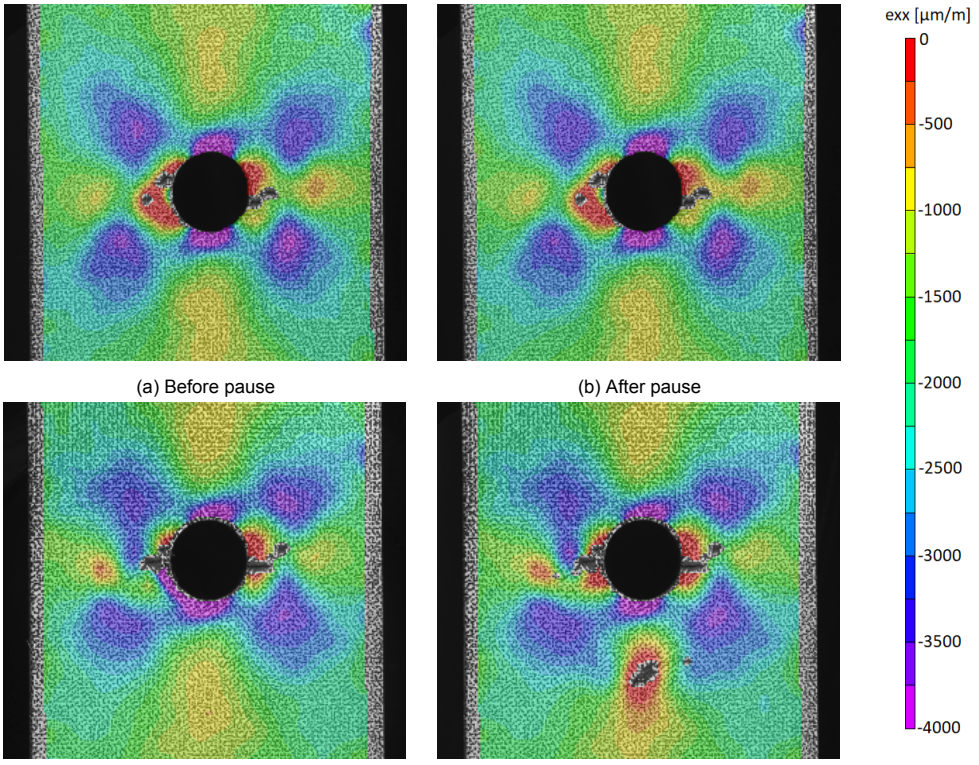


(a) Before pause (b) After pause

(c) Before impact (d) After impact

Figure 5.21: Transverse surface strain ($\epsilon_X$) of samples paused (top, specimen 45) and impacted (bottom, specimen 41) after 14% longitudinal strain increase

The C-scan images of the specimens paused at 14% strain increase are shown in Figure 5.22. Image (a) shows a specimen that is stopped right after the pause. Image (b) presents a sample that is impacted during this pause, then stopped. As expected based on the previous results, a significant increase in damage area is observed with respect to (a), but no obvious differences are found in the critical damage areas directly left and right of the hole. Image (c) presents a specimen that is impacted and then fatigued until the 20% threshold is reached. The damaged area is slightly smaller than in (b). This is a result of random variation between samples, as the damage will not magically repair itself.

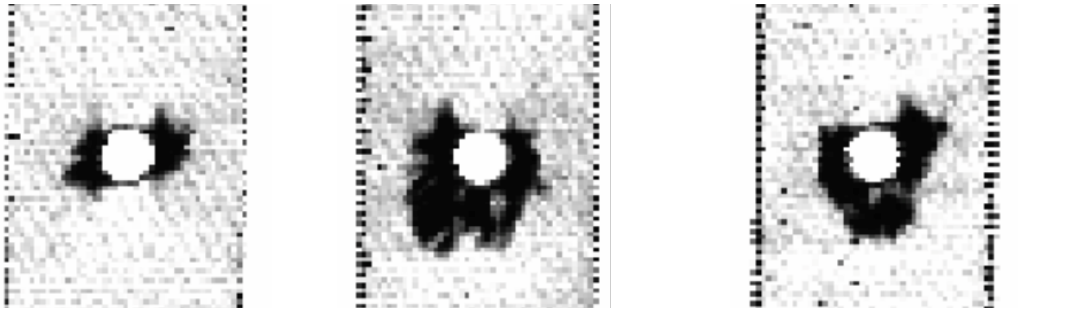

(a) Stopped after pause (specimen 15) (b) Stopped after impact (specimen 28) (c) Continued to 20% after impact (specimen 40)

Figure 5.22: C-scans of specimens paused at 14% strain increase

## 5.5. Paused at 20% Strain Increase

The number of cycles to the pause moment and the fatigue lives of the specimens paused at 20% are shown in Table 5.5. A slight difference can be seen, but taking into account the scatter this difference is not meaningful. Also, the specimens with longer fatigue lives also typically took longer to reach the strain threshold level, which further demonstrates that the impact had no effect on fatigue life.

Table 5.5: Number of cycles to threshold and fatigue life of 20% samples

| Sample | Impact | Paused at Cycles [$10^3$] | Mean paused Cycles [$10^3$] | Fatigue life Cycles [$10^3$] | Mean fatigue life Cycles [$10^3$] |
|---|---|---|---|---|---|
| 23 | | 41.2 | | 72.6 | |
| 11 | No | 16.2 | 22.7 | 29.5 | 41.7 |
| 31 | | 10.6 | | 23.0 | |
| 47 | | 34.7 | | 81.4 | |
| 17 | Yes | 36.3 | 29.2 | 49.4 | 52.2 |
| 38 | | 16.7 | | 25.9 | |

Figure 5.23 shows the strain increase plots of the 20% samples. Since there is no difference between the tests before the threshold is reached, no difference aside from random variation is seen below the dashed line. Directly after the pause moment however, the impacted samples make a large jump upwards within a short time span. Although the fatigue lives are not necessarily shortened by impact, the strain values are typically about 10% higher before failure.

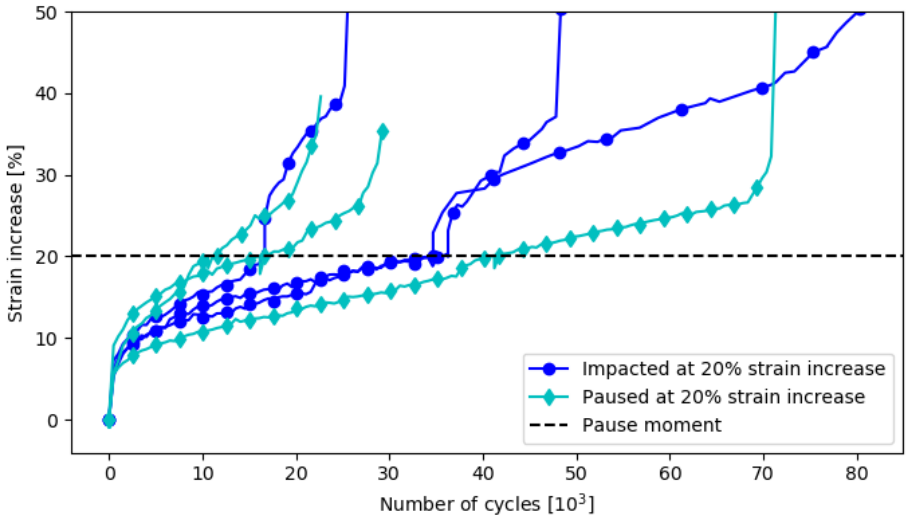


Figure 5.23: Strain plots of samples paused at 20%

The cumulative AE energy release and number of hits are shown in Figures 5.24 and 5.25 respectively. Two of the impacted specimens were not measured correctly using the AE system, so unfortunately only one such sample is shown. A longer rearm time was set accidentally, meaning that fewer hits were measured. The graphs are therefore not comparable. The jump in strain seen in the previous figure would suggest a similar increase in the energy release, number of hits or both right after the pause. The slope of the energy release curve of the impacted sample is indeed higher than that of the other samples, but it looks like the slope started to increase before the pause already. Nothing can really be said about the cumulative number of hits registered, the impacted sample follows the path of two of the paused samples exactly. No difference between either side of the pause moment is observed.

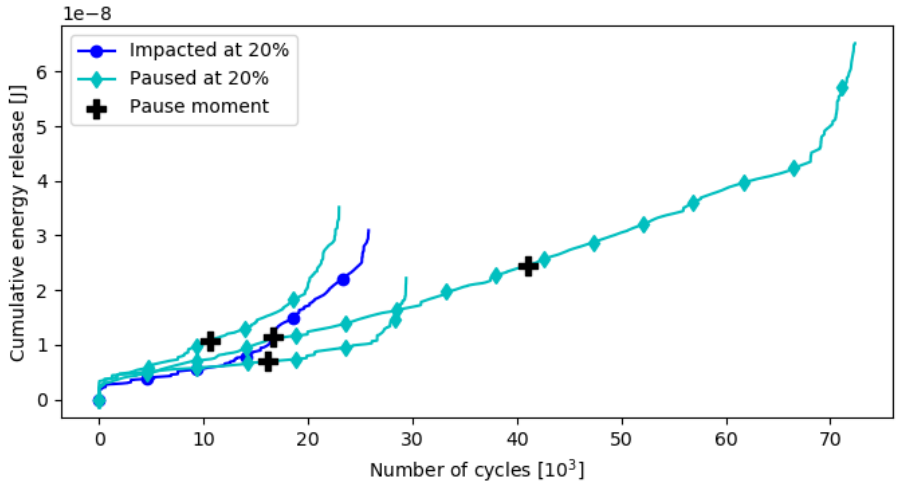


Figure 5.24: Cumulative energy plots of samples paused at 20%

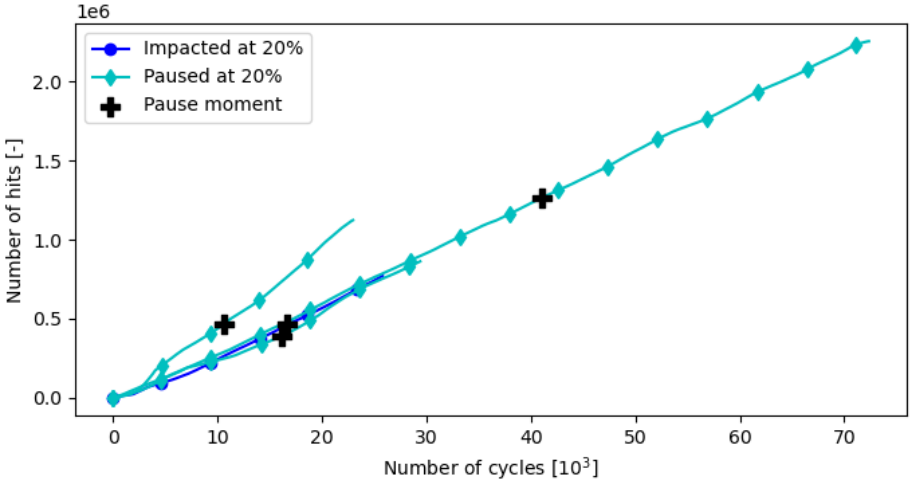


Figure 5.25: Cumulative number of AE hits of samples paused at 20%

The longitudinal surface strains are shown in Figure 5.27. A similar pattern is observed as in the 14% case: no difference is seen in the sample that is only paused, and aside from the actual impact location, no difference is observed for the impacted specimen either.

Looking at the transverse strains in Figure 5.28, again the top two images don't show a difference as expected. The impacted specimen however does show some difference. Directly at the lower hole edge, a small compression zone disappeared and some cracking is seen. Also, the areas showing compressive strain to the top right, bottom left and bottom right all show an increase in area after impact.

Figure 5.26 shows the C-scans of two samples paused at 20% strain increase. The areas left and right of the hole look quite similar, with the addition of the large delaminated area due to impact seen in image (b).

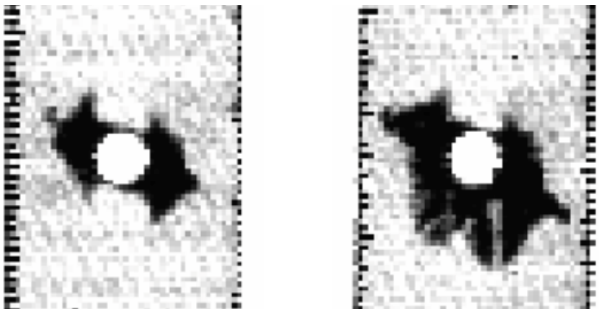

(d) Stopped after pause (specimen 37) (e) Stopped after impact (specimen 32)

Figure 5.26: C-scans of specimens paused at 20%

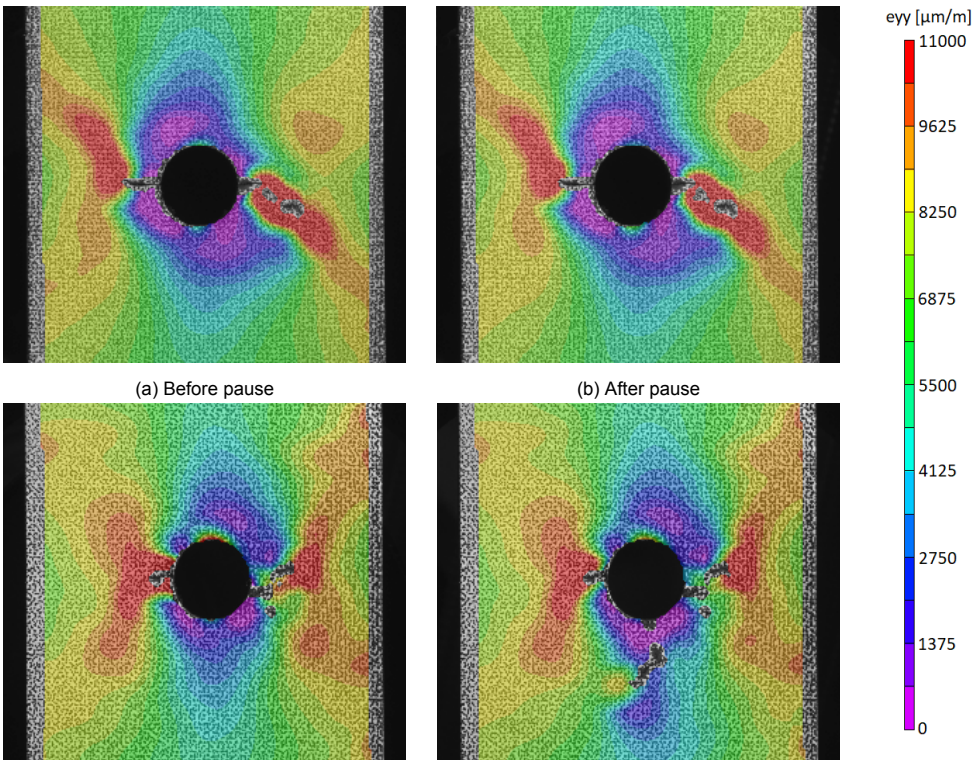


(a) Before pause (b) After pause

(c) Before impact (d) After impact

Figure 5.27: Longitudinal surface strain ($\epsilon_Y$) of samples paused (top, specimen 23) and impacted (bottom, specimen 47) after 20% longitudinal strain increase

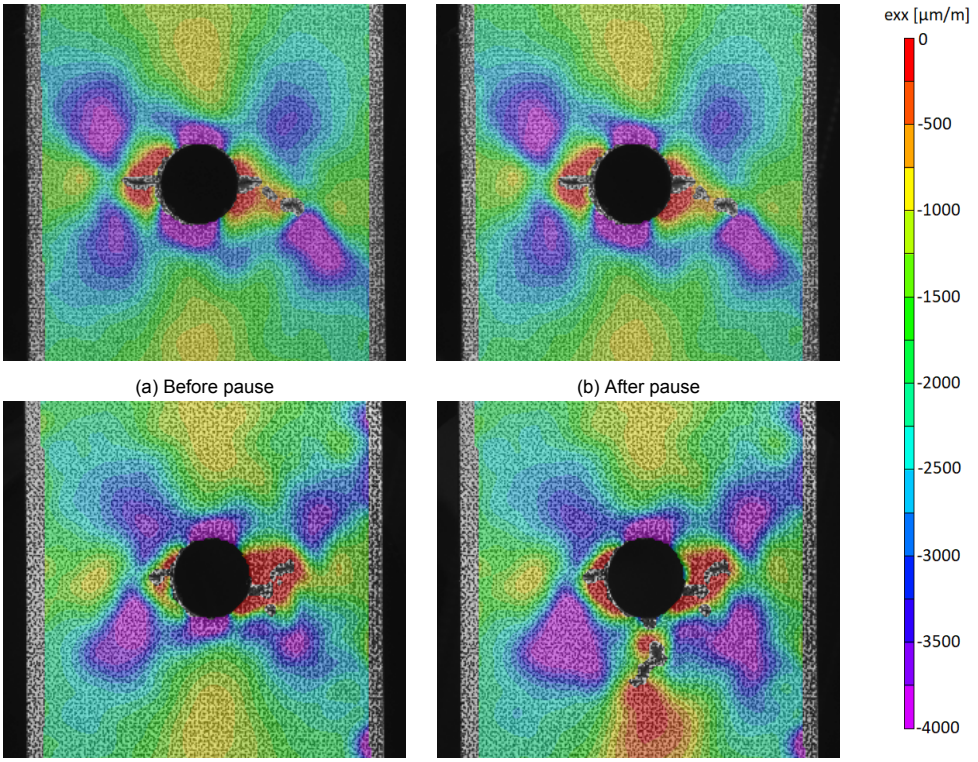


(a) Before pause (b) After pause

(c) Before impact (d) After impact

Figure 5.28: Transverse surface strain ($\epsilon_X$) of samples paused (top, specimen 23) and impacted (bottom, specimen 47) after 20% longitudinal strain increase

## 5.6. Discussion

This section discusses and compares the various different tests and the data gathered in order to derive patterns from which conclusions can be drawn. The observations regarding fatigue loading and impact loading are discussed in subsections 5.6.1 and 5.6.2 respectively. Afterwards, combined fatigue and impact loading is discussed in subsection 5.6.3. It should be reiterated that a larger variety of visualisations were made based on the gathered data. For example, kernal density estimation (KDE) graphs, and graphs that were zoomed in around the impact moment were made from the AE data, but these did not provide any new information that is not observed from the plots provided in this chapter.

### 5.6.1. Fatigue

Various things were observed regarding the damage accumulation of the samples that were cyclically loaded without impact. First of all, it should be emphasised again that high fatigue load values were used. With the maximum load of each cycle reaching 80% of the ultimate load, a lot of damage is already done within the first few cycles. Visible (in the woven outer plies) and audible cracking upon first loading confirmed this. The C-scans have shown that there is no significant delaminated area at this point, so the damage is primarily intralaminar. While there is no question that the off-axis plies have severe matrix cracking at this point, it is likely that some fibre fracture in the UD plies occurred as well. No inspection method was used that can inspect for any cracking within the specimen, so the extent of it cannot be confirmed. The matrix cracking is however likely to initiate delaminations early on in the fatigue program.

During the fatigue loading, an S-shaped strain increase is measured, which reflects an S-shape stiffness reduction as was also discussed by for example Broughton et al. [14]. The acoustic emission data shows a more steady increase in terms of energy release and cumulative number of hits. The strain field images as produced by the DIC setup as well as the C-scans show the same steady increase in damage. Because the 0° plies are the last to fail and the 90° plies hardly contribute to the longitudinal stiffness to begin with, the stiffness decrease over time must be caused primarily by damage in the ±45° and outer 0/90° plies. This increase in intralaminar damage is likely to go hand in hand with the delamination growth between the various layers. Figure 5.29 shows specimen 30 shortly before failure, where the crack in the top ply extends along most of the width of the sample, with the longitudinal strain near the crack still very high. This crack originating from the hole always tends to follow a +45 or -45° direction. Furthermore, a sharp increase in energy release due to high amplitude (>80 dB) AE hits was observed near the end of a specimen life. High amplitude signals are typically associated with fibre fracture, as opposed to matrix damage mechanisms characterised by lower-amplitude hits. These observations supplement the idea that the centrally located 0° are the only remaining plies that significantly contribute to the stiffness at this point.

Figure 5.30 shows an overlay of the C-scan and DIC image of specimen 29. This shows that the crack tips coincide with the edges of the delaminated zones. From this point, the delaminations run along +45 and -45° angles which probably coincide with splits in the respective +45 and -45° plies. The vertical edges of the delamination area probably indicate splits in the central 0°plies. The shapes of the delaminations between the individual layers and how they link up remains unknown.

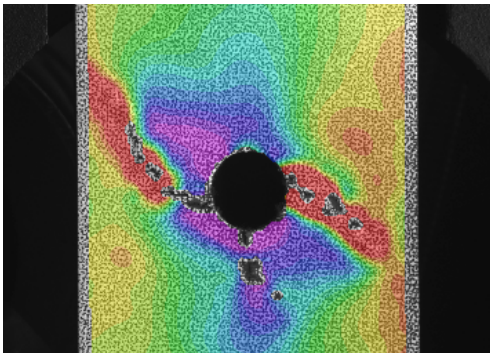

Figure 5.29: Crack seen in sample 30 shortly before failure

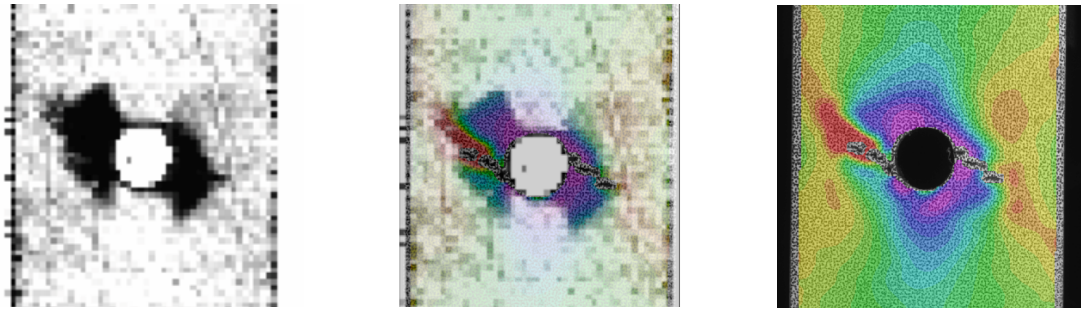

(a) C-scan (b) Overlay (c) DIC image

Figure 5.30: Overlay of C-scan and DIC image of specimen 29

A difference in fatigue life was observed between the specimens that were continuously loaded and the samples paused at various strain thresholds. However, the large scatter in the data and the low number of specimens per test type mean that the differences are not statistically significant. The measurements do not provide much information, with no AE signals being released during the pause. Also, both the AE data and strain data do not show much difference before and after the pause. This is further substantiated by the DIC strain fields that show virtually the same image before and after. Lastly, C-scans of two samples at the same strain increase level (20%) show no difference whether paused or not. In spite of all this, there is a clear trend; pausing lengthens the fatigue life, and this effect is stronger the earlier the pause occurs. One explanation is that creep or viscoelastic effects are at play that slow down the subsequent fatigue damage accumulation.

### 5.6.2. Impact

The 10J impact events used in the tests induced damage which was clearly visible from the back side (the side from which the DIC images are taken). In addition, C-scans showed a significant delamination area at the impact location. On the impacted side however, hardly any sign of the impact event could be observed with the naked eye, which means the damage created falls well within any definition of BVID. See Figures 4.9 and 4.10 in the previous chapter for an example.

Figure 5.31 shows a C-scan, DIC image and an overlay of both, showing the cracks in relation to the delaminated area in sample 40. This specimen was impacted at 14% strain increase, after which it was fatigue loaded until 20% and then stopped. It clearly shows the delamination area and crack as a result of the impact. Both the delaminated areas due to prior fatigue damage and due to impact are large enough to overlap. Out of plane impact events typically create an array of delaminations between different plies, as shown for example by Bouvet et al. using both experimental and computational work [54]. Without a method to accurately distinguish individual plies, not much can be said about individual ply separation in the tests performed for this thesis. In general, delaminations normally occur mainly near the middle of a laminate, where the shear stresses are highest in case of an out of plane loading. In such thin laminates however, this effect may not be so significant.

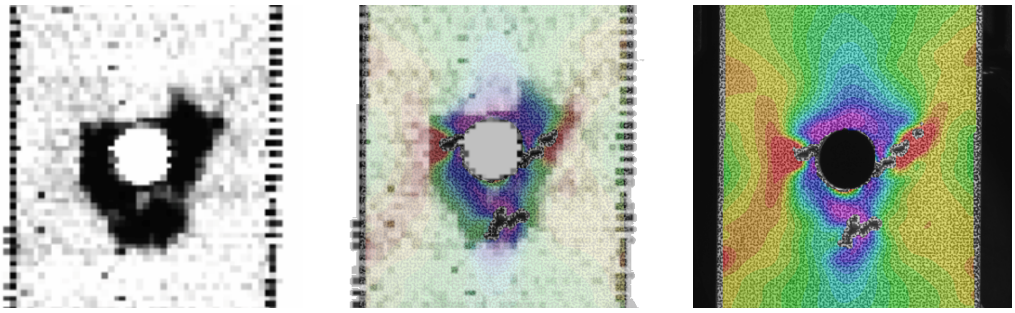

(a) C-scan (b) Overlay (c) DIC image

Figure 5.31: Overlay of C-scan and DIC image of specimen 40

### 5.6.3. Combined Loading

Between the specimens that are paused or impacted at 0% strain increase (before fatigue), a statistically significant difference in fatigue life is observed. The life of an impacted sample is on average a factor five shorter than that of a specimen that is merely paused. This difference is substantiated by the various measurements performed. The strain graphs and the graphs showing cumulative AE energy release and number of AE hits all show a faster damage accumulation after being hit versus being paused. The strain field images as measured using DIC show - in addition to the damage formed at the location of impact - crack growth at the side of the hole. This crack then continues to grow under subsequent fatigue loading, until specimen failure. The C-scan results show delamination formation to one side of the hole due to impact, likely on the same side as the crack formation. This delamination is triangular in shape, going outwards from the hole under ±45° angles. The earlier discussion about the difference in fatigue life observed between the specimens continuously tested or paused (without impact) at different thresholds should be considered here. It could be that the long fatigue lives observed with the specimens paused at 0% are a coincidence. If the samples that are impacted at 0% are however compared to the uninterrupted fatigue specimens, there is still a difference in fatigue life with a statistical significance of P=0.050. While the accuracy of this value is questionable with such small group sizes, the conclusion is still credible in combination with the differences observed in the measurements. In fact, the lives of the specimens impacted at 0% are similar to the remaining fatigue lives of the specimens paused at 20%. The fatigue life of the 0% impacted samples is on average 16'000 cycles, while for the specimens paused at 20%, the remaining life after the pause is 19'000 cycles. It seems that the impact raises the damage level along the critical fatigue damage path to a similar extent as when a specimen is fatigue loaded towards a 20% strain increase. This is reflected by the graphs shown in Figure 5.9, where the strain of the impacted samples go up almost vertically towards 20% strain increase at the start of the test. In other words, by impacting at the start, the specimen 'skips' the first 20% of strain increase that would otherwise be caused by fatigue loading.

In contrast, these differences in fatigue life are not observed between the paused in impacted specimens at 14% and 20%. This is reflected in the measurements as well. No large dissimilarity is observed between the AE measurements. Also, while the DIC strain fields and C-scans show the damage caused by impact below the hole, either no or only very small changes to to the strain field, crack size or delaminated area to the sides of the hole are seen. The strain graphs show a jump in strain after impact, but the final failure strain is also higher. This makes sense as the total damaged area is unquestionably larger. Apparently, it does not influence the damage size and severity along the critical damage path along which final fracture occurs. Damage in the form of delaminations and cracks are present next to the hole right before impact, which has caused a significant stiffness reduction in this area. The energy of the impact is evidently not enough to overpass this damaged area and have an effect on the propagation of this damage. The lower stiffness of the material due to damage means that the impact forces will be transmitted through the material less easily.

Figure 5.32 shows C-scans of the samples impacted at 0%, 14% and 20% respectively, after which all of them were cyclically loaded up to 20% strain increase. Image (c) stands out as it has the largest delaminated area, but note that this sample was impacted only after reaching a 20% strain increase, thus the strain after impact is likely larger. Images (a) and (b) show very similar damage patterns. Also, the AE and DIC data both show that the damage accumulation patterns for specimens that are either paused at 0% or later are similar. This supports the reasoning that the type and shape of damage that is accumulated up to final fracture is equivalent whenever the impact occurs, but is accelerated when impacted immediately at the start of fatigue testing.

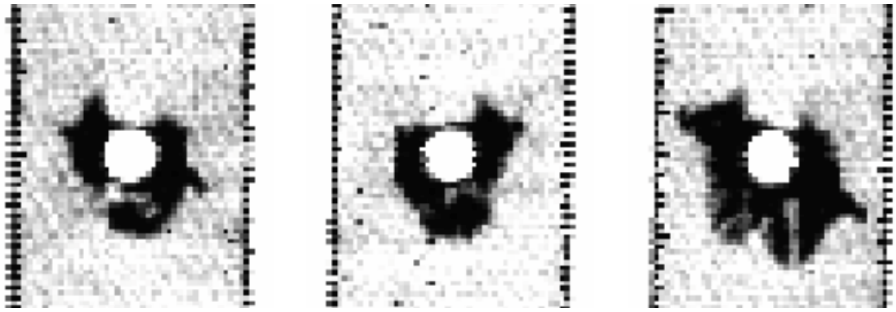

(a) Impacted at 0% (specimen 21) (b) Impacted at 14% (specimen 40) (c) Impacted at 20% (specimen 32)

Figure 5.32: C-scans of impacted specimens, stopped at 20% strain increase

# 6

# Conclusions

In this thesis project, the effects of combined fatigue and impact loading in carbon fibre reinforced composite (CFRP) specimens were investigated. Composite materials are widely used in modern commercial aircraft, but are known to have complex damage mechanisms and are especially prone to foreign object impact damage. While research has been performed on compression, tension and fatigue loading after impact, there is a lack of knowledge on what happens when these loading scenarios are not discretely separated. There is a direct implication of the interaction of such loading situations on structural integrity and the remaining useful life after damage. Moreover, better comprehension can have indirect implications for example on improving damage models or the design of structural health monitoring (SHM) systems in aircraft. In order to fill a part of this knowledge gap, the problem description is narrowed down to one specific scenario, with the following research question:

**What are the effects of the timing of an impact event on the fatigue life and damage patterns in a CFRP structure?**

In order to answer this question, an experimental testing campaign was set up where samples were impacted in-situ during a short interruption of a tension-tension fatigue program. Open-hole CFRP samples were used with a combination of unidirectional plies in quasi-isotropic orientation in the centre and a plain woven ply on each side. The specimens were impacted directly below the central hole using a gas gun with aluminium tipped bullets. The impact energy used was about 10 J. Measurements were performed using a combination of digital image correlation (DIC), acoustic emission (AE) and ultrasonic C-scanning. Before the main research question can be answered, several subquestions were defined which are answered below. The main research question as well as the subquestions only relate directly to the structure and testing parameters used in this thesis, and cannot be generalised per se.

1. **How does the structure respond to pure cyclic loading?**
   The response to fatigue loading was as expected based on the literature research. Because of the high maximum loads, the specimen is damaged upon first loading, with a more gradual damage accumulation afterwards. The performed DIC, AE and C-scan measurements all provided information on the damage accumulation process. The decrease of local stiffness was accurately tracked using the strain measurements. In addition, the DIC data showed a distinctive butterfly-shaped strain field around the central hole, and it shows visible surface cracks extending from the hole outwards until failure.

2. **How does the structure respond to pure impact?**
   The impacts consistently caused barely visible impact damage (BVID), with visible cracking on the back side and a delaminated area around the impact location shown by C-scan. Without prior fatigue damage, an impact also caused damage to the side of the central hole. This was shown both by C-scan in the form of a delamination zone, as well as using DIC, showing an increase in

crack length and strain levels. Note that a small crack is already present because the specimen reaches the maximum fatigue load once before impact.

3. **What is the effect of interrupting a fatigue test?**
   The damage patterns in the paused and continuously tested samples are very similar. A difference in the pace of damage accumulation was seen however, which on average is slower when a specimen is paused. The earlier the pause in the fatigue program, the stronger this effect. During the pause, no AE hits are measured, so it is reasonable to assume no damage occurs during this time. One possibility is that the pause causes some sort of viscoelastic or creep effect in the matrix, which suppresses damage growth. Despite the spread in the data and the low number of specimens per test type, a trend is seen which could be investigated further.

4. **What is the effect of pre-existing fatigue damage on the damage caused by impact?**
   When fatigue damage is already present, an impact event does not cause additional damage next to the hole. This differs from the pure impact case described at subquestion 2. The damage caused directly around the point of impact is however very similar. Although the damage areas overlap, they do not seem to influence each other much. The lowered stiffness around the hole due to the fatigue damage possibly reduces the transmission of impact forces through the material. The impact occurs outside of the critical damage path in this case, and it is likely that a different conclusion would be drawn if the impact was aimed right along this fatigue damage path. In this case, that would be directly left or right of the hole.

5. **How does the structure respond differently with and without impact damage?**
   Although some variation is observed for individual specimens, in general it can be concluded that the fatigue damage patterns due to fatigue are similar before and after an impact. There are differences however in terms of the remaining fatigue life and how the critical damage path develops. When impacted before fatigue (at 0% strain increase), the damage level along the critical path gets a head start, and the subsequent fatigue damage increases as if serious fatigue damage was already present before. When impacted later at 14% strain increase, a slight jump in strain is seen after impact due to a decreased stiffness in the central area. Also, there is sometimes as light decrease in the number of hits and energy measured using AE after impact, but that is also observed after a pause. Finally, after a 20% strain increase, an impact causes a large jump in strain, but again the damage patterns due to fatigue are the same afterwards. This critical damage accumulates at a similar rate as after a pause at 20%.

By combining the answers to these questions, the main research question is answered as follows.

**By impacting the structure before any fatigue loading is applied, damage is done to the highly loaded areas next to the hole which then grows under the subsequent cyclic loading, leading to a shortened fatigue life. The damage along the critical fatigue damage path essentially gets a head start. If the impact occurs when fatigue damage is already present, there is no significant effect on the critical damage path and fatigue life. Since the impacts were aimed outside of this fatigue damage path, the results could be very different when the impact is aimed directly at this critical zone instead.**

# 7

# Recommendations

Based on the conclusions presented in the previous chapter, several recommendations are made. The recommendations are ordered from specific ideas to solidify the conclusions of this report, towards suggestions regarding a more general understanding of combined loading conditions in composite structures.

1. First and foremost, it would be helpful to repeat similar tests, perhaps with different interruption thresholds, in order to solidify the conclusions that were found. Testing a larger number of specimens increases the statistical significance of the quantitative data. Specifically, the effects of fatigue test interruptions could be investigated.

2. Focusing on different non-destructive inspection (NDI) techniques will shed more light on the damage patterns. This research has blind spots regarding the individual damage mechanisms, and more data will tie the observations presented in this document together with more general knowledge of damage in composites. For example, X-ray technology can be used to assess matrix cracking within samples. In addition, a characterisation study of the different acoustic emission (AE) signals released with different damage mechanisms could be performed. This could be combined with data-driven algorithms to check for any effects that are overlooked when manually interpreting the data.

3. The findings can be generalised if a wider array of materials, layups, geometries and loading scenarios are tested. To start with, tests could be performed where the structure is impacted directly along the path of critical fatigue damage accumulation.

4. A numerical model could be built that recreates the testing circumstances of this thesis. If the results are replicated, it could pave the way towards more universal conclusions by simulating a wider array of scenarios.

If strong, universal conclusions are found, they could be applied in a broader context. For example, their implications on qualification, inspection and repair protocols of aircraft structures should be investigated. In addition, such knowledge can be used in combination with the data gathered during the required tests to assess the the way that novel SHM systems react to combined loading scenarios.

# A

# C-scan Images

This appendix provides an overview of all the specimens that are C-scanned. Table A.1 gives a list of the samples, with their corresponding strain threshold where they were paused, whether or not they were impacted and at what strain threshold the test was stopped. The specimens were scanned two times. The GTM Advanced Structures company in The Hague scanned the black and white images, which provided good contrast but did not differentiate between the different plies. Afterwards, the samples were inspected at the faculty by Dr. M. Saeedifar using an Olympus RollerFORM wheel probe in combination with an Olympus OmniScan SX acquisition and display device. While this machine is able to measure the depth location of a delamination, accurately scanning thin samples has proven difficult. This is supported by the manufacturer, who states that a thickness of 2 mm is the lower boundary of the scanning range, and a thicker laminate gives better results. The black and white images were mainly used throughout this document, but an overview of all the images is provided in Figure A.1 for reference. Note that some of the coloured scans are rotated 180 degrees to be in the same orientation as the black and white images.

Table A.1: Overview of tests performed on C-scanned samples

| **Specimen** | **Paused at** % strain increase | **Impacted** | **Stopped at** % strain increase |
|---|---|---|---|
| 12 | 0 | No | 0 |
| 19 | 0 | Yes | 0 |
| 49 | 0 | Yes | 0 |
| 29 | 0 | No | 20 |
| 21 | 0 | Yes | 20 |
| 15 | 14 | No | 14 |
| 28 | 14 | Yes | 14 |
| 40 | 14 | Yes | 20 |
| 37 | 20 | No | 20 |
| 32 | 20 | Yes | 20 |

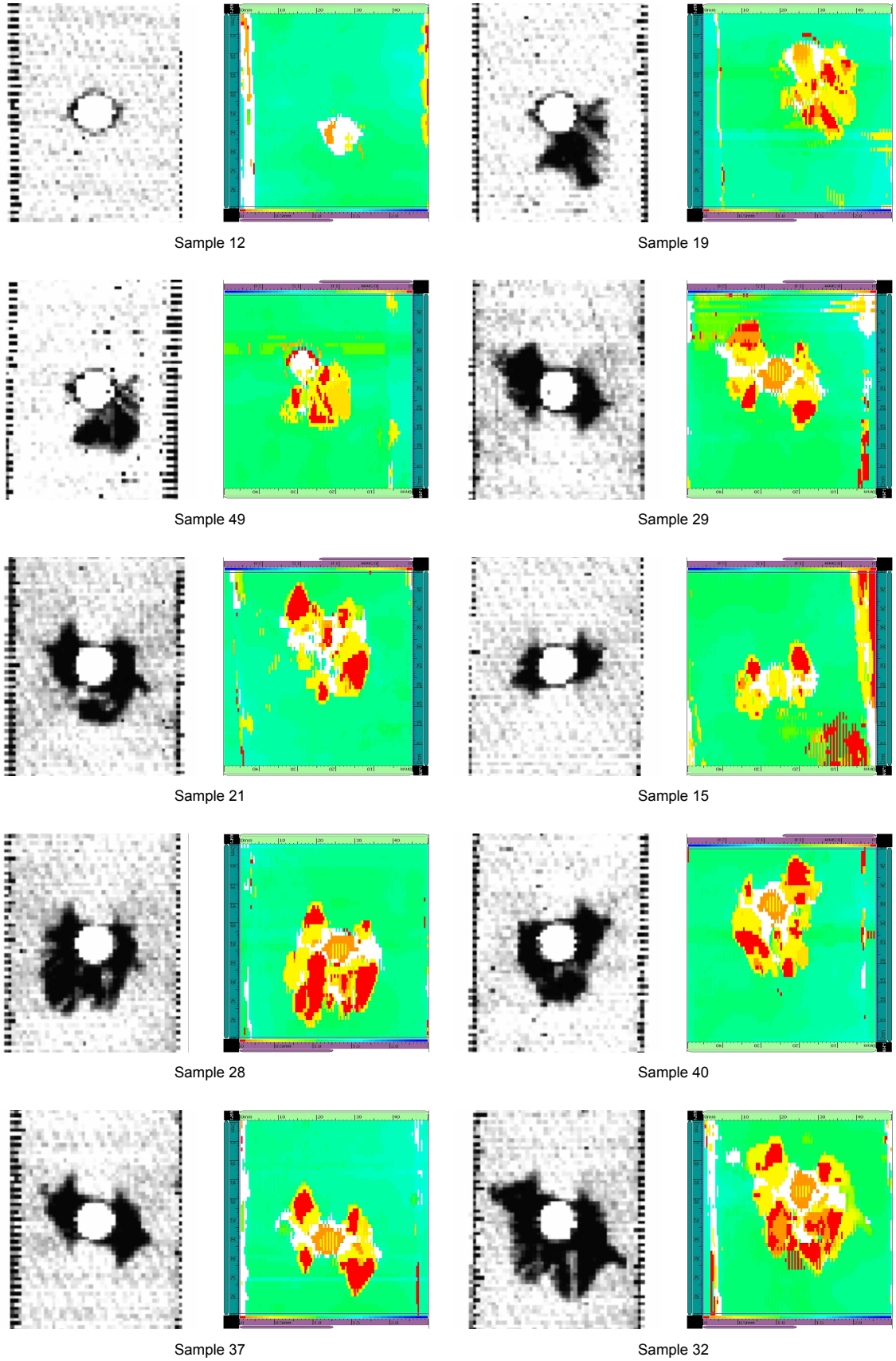


Figure A.1: Overview of all the C-scanned samples

# B

# Filtered Acoustic Emission Data

This appendix presents additional acoustic emission data. Plots are shown both with the cumulative energy release and the cumulative number of hits against the number of fatigue cycles. These plots show the complete measured range of signals between 60 and 100 dB. For every graph shown, two filtered plots are presented, one showing only hits with amplitudes between 60 and 80 dB, and the other showing hits between 80 and 100 dB. This is shown for the specimens paused at 0%, 14% and 20% respectively.

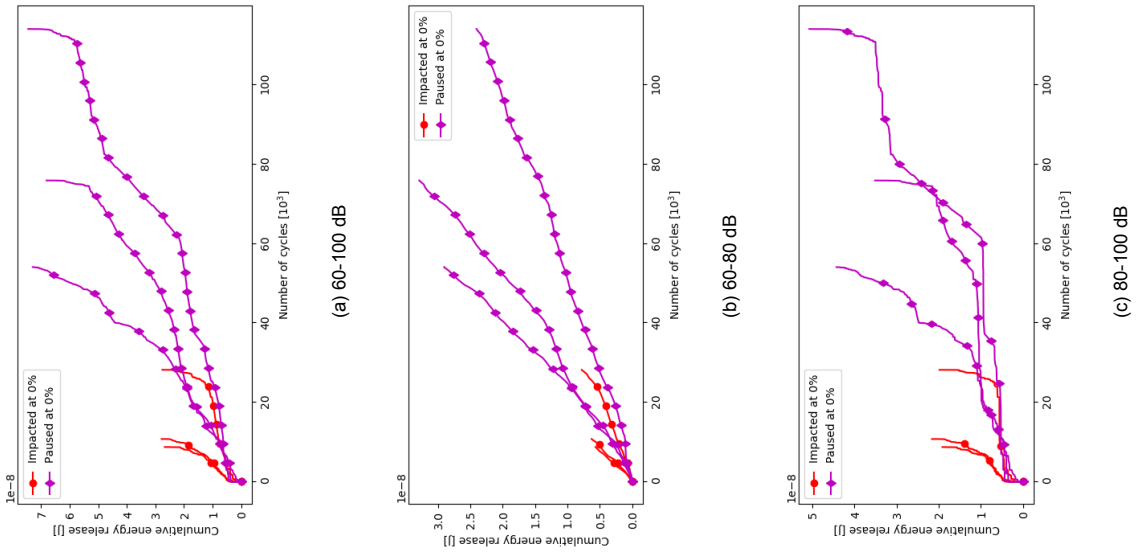


Figure B.1: Cumulative energy release of 0% samples

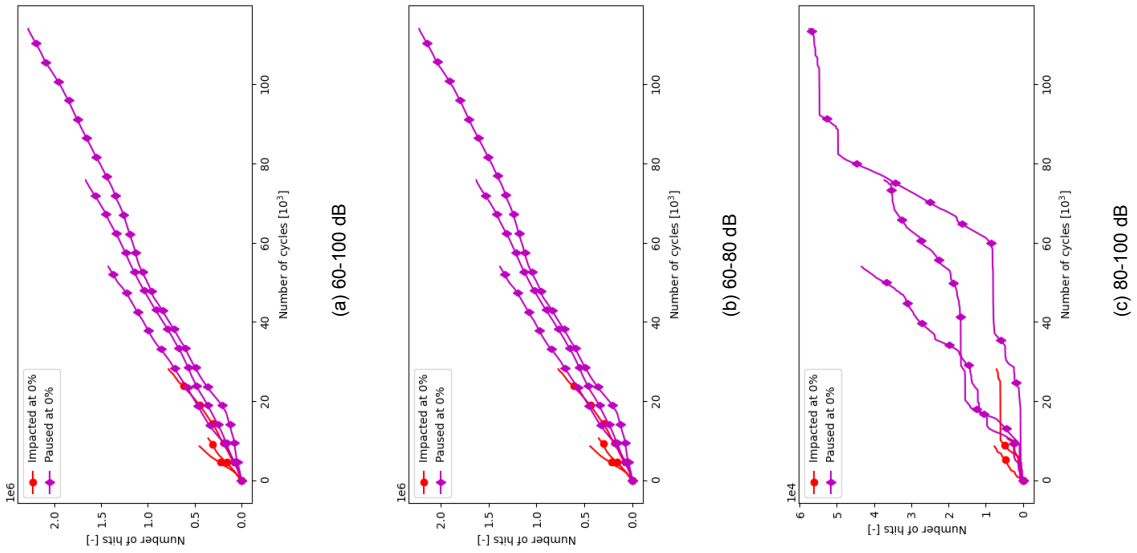


Figure B.2: Cumulative number of hits of 0% samples

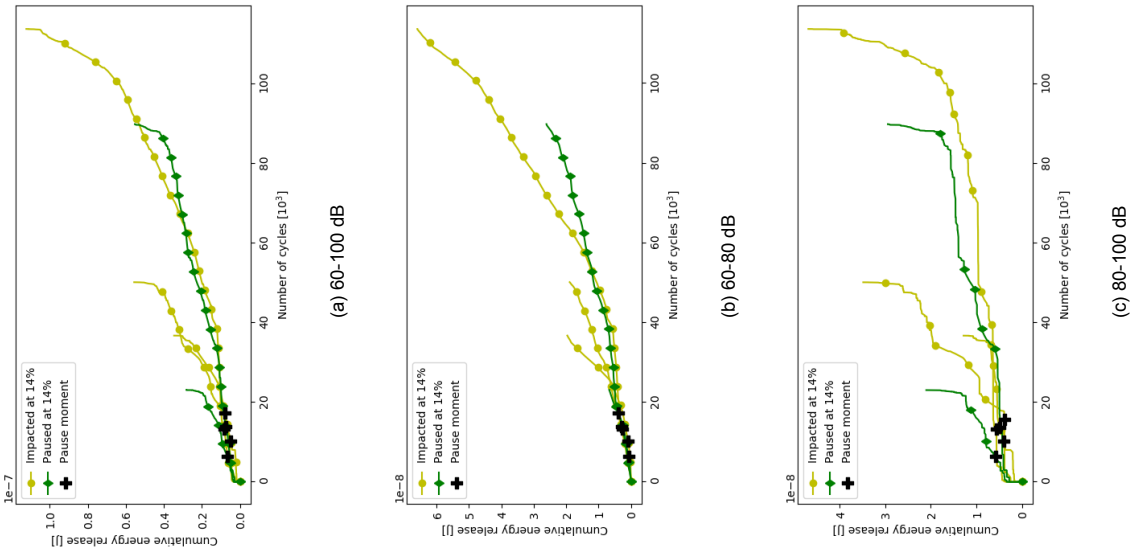


Figure B.3: Cumulative energy release of 14% samples

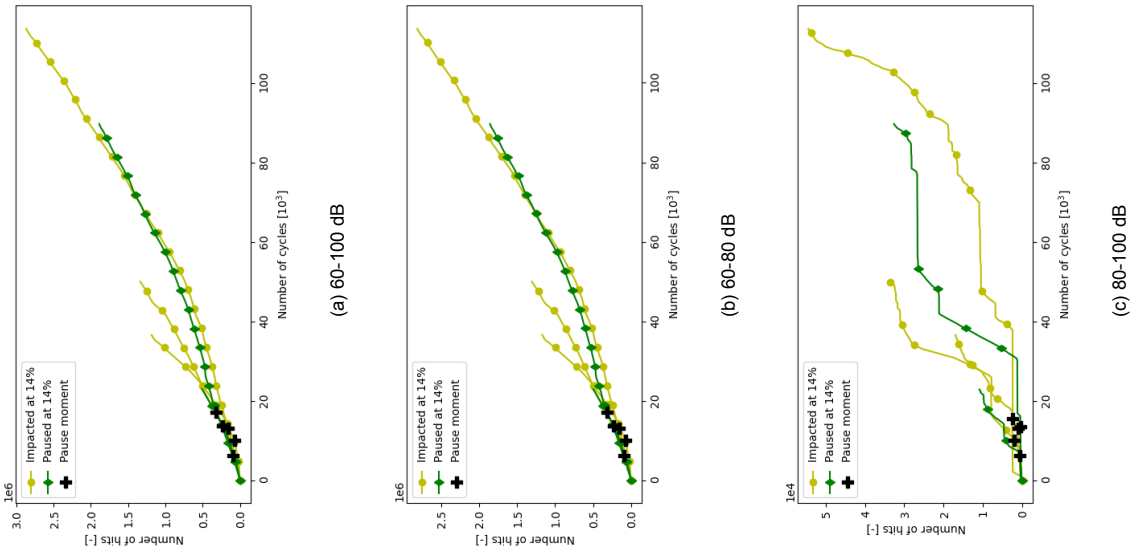


Figure B.4: Cumulative number of hits of 14% samples

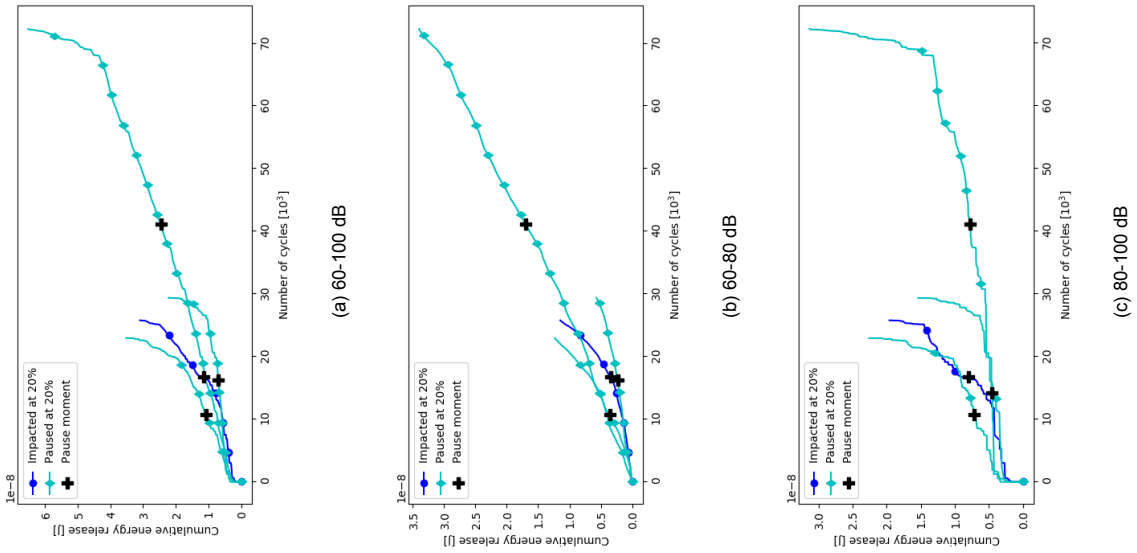


Figure B.5: Cumulative energy release of 20% samples

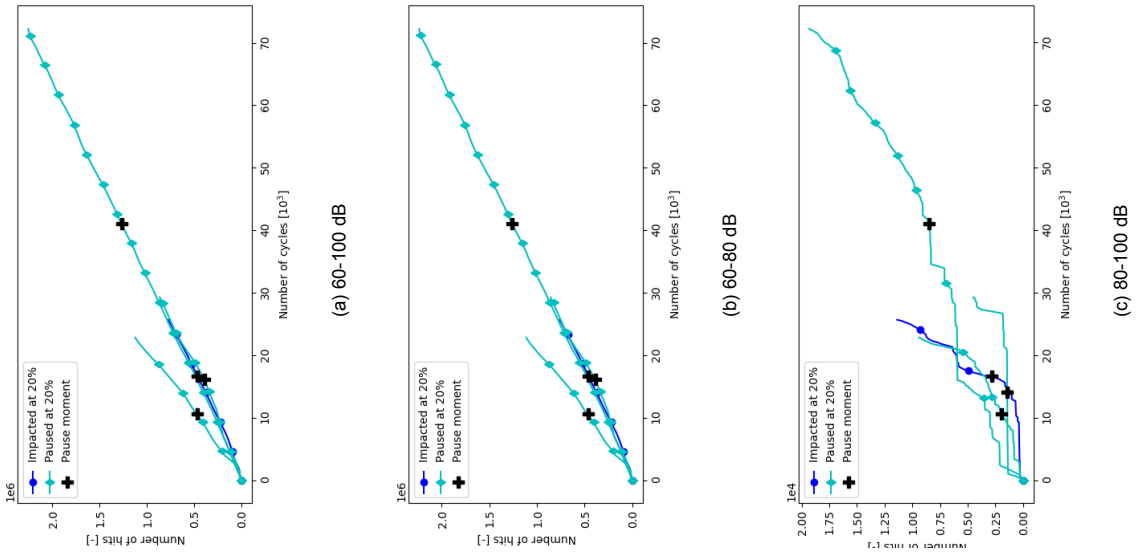


Figure B.6: Cumulative number of hits of 20% samples

# C

# Strain field throughout specimen life

To get some insight into the progression of strain over the life of a specimen, Figure C.2 shows a series of surface strain fields as measured using digital image correlation (DIC). Sample 41 is shown, which is impacted at 14% strain increase. The images are shown with intervals of 2'500 cycles, except for one interval which was about 2'000 cycles. The sample was impacted at around 10'100 cycles and failed after 36'900 cycles. In order to leave more space for the images themselves, the colour legend is shown in Figure C.1 instead.

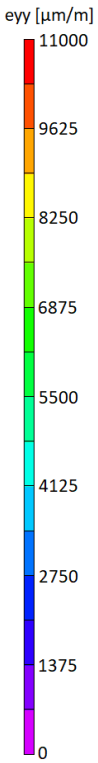


Figure C.1: Colour bar

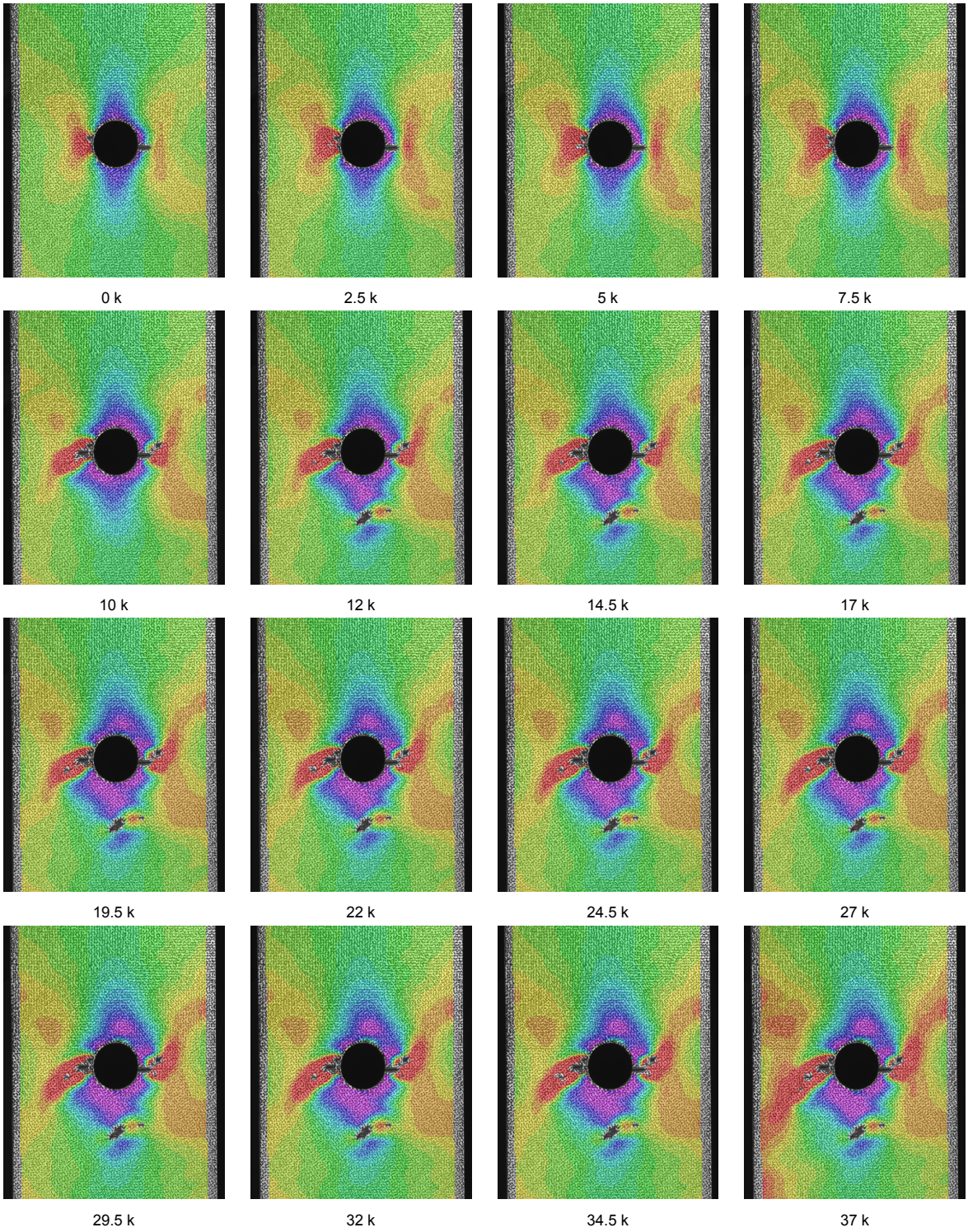


Figure C.2: Longitudinal surface strain fields ($\epsilon_y$) of sample 41, with the rough number of fatigue cycles at every instance in thousands.

# Bibliography


[1] M. R. Woodward and R. Stover, “Damage Tolerance,” in *ASM Handbook Volume 21: Composites* (D. B. Miracle and S. L. Donaldson, eds.), p. 298, ASM International, 1st ed., 2001.

[2] EASA, “Annex II - AMC 20-29 to ED Decision 2010/003/R,” tech. rep., EASA, 2010.

[3] A. Vlot, *Low-velocity impact loading on fibre reinforced aluminium laminates (ARALL) and other aircraft sheet metals*. PhD thesis, Delft University of Technology, 1991.

[4] G. Davies and P. Irving, “Impact, post-impact strength and post-impact fatigue behaviour of polymer composites,” in *Polymer Composites in the Aerospace Industry*, pp. 231–259, Elsevier Inc., 9 2014.

[5] R. J. H. Wanhill, L. Molent, S. A. Barter, and E. Amsterdam, “”Milestone Case Histories in Aircraft Structural Integrity”,” tech. rep., NLR, Amsterdam, 2015.

[6] O. J. Nixon-Pearson, S. R. Hallett, P. J. Withers, and J. Rouse, “Damage development in open-hole composite specimens in fatigue. Part 1: Experimental investigation,” *Composite Structures*, vol. 106, pp. 882–889, 12 2013.

[7] R. C. Alderliesten, A. J. Brunner, and J. A. Pascoe, “Cyclic fatigue fracture of composites: What has testing revealed about the physics of the processes so far?,” *Engineering Fracture Mechanics*, vol. 203, pp. 186–196, 11 2018.

[8] Z. Hashin and A. Rotem, “A Fatigue Failure Criterion for Fiber Reinforced Materials,” *Journal of Composite Materials*, vol. 7, pp. 448–464, 10 1973.

[9] M. Kortschot and P. Beaumont, “Damage mechanics of composite materials: II— a damaged-based notched strength model,” *Composites Science and Technology*, vol. 39, no. 4, pp. 303–326, 1990.

[10] M. T. Kortschot and P. W. Beaumont, “Damage mechanics of composite materials. IV: The effect of lay-up on damage growth and notched strength,” *Composites Science and Technology*, vol. 40, no. 2, pp. 167–179, 1991.

[11] S. M. Spearing and P. W. Beaumont, “Fatigue damage mechanics of composite materials. I: Experimental measurement of damage and post-fatigue properties,” *Composites Science and Technology*, vol. 44, no. 2, pp. 159–168, 1992.

[12] B. G. Green, M. R. Wisnom, and S. R. Hallett, “An experimental investigation into the tensile strength scaling of notched composites,” *Composites Part A: Applied Science and Manufacturing*, vol. 38, no. 3, pp. 867–878, 2006.

[13] S. Hallett, B. Green, W. Jiang, and M. Wisnom, “An experimental and numerical investigation into the damage mechanisms in notched composites,” *Composites Part A: Applied Science and Manufacturing*, vol. 40, pp. 613–624, 5 2009.

[14] W. R. Broughton, M. R. L. Gower, M. J. Lodeiro, G. D. Pilkington, and R. M. Shaw, “An experimental assessment of open-hole tension–tension fatigue behaviour of a GFRP laminate,” *Composites Part A: Applied Science and Manufacturing*, vol. 42, pp. 1310–1320, 10 2011.

[15] D. Kalyanasundaram, S. Gururaja, P. Prabhune, and D. Singh, “Open hole fatigue testing of laser machined MD-CFRPs,” *Composites Part A: Applied Science and Manufacturing*, vol. 111, pp. 33–41, 8 2018.

[16] B. Aidi, M. K. Philen, and S. W. Case, “Progressive damage assessment of centrally notched composite specimens in fatigue,” *Composites Part A: Applied Science and Manufacturing*, vol. 74, pp. 47–59, 2015.

[17] L. Amaral, L. Yao, R. Alderliesten, and R. Benedictus, “The relation between the strain energy release in fatigue and quasi-static crack growth,” *Engineering Fracture Mechanics*, vol. 145, pp. 86–97, 2015.

[18] N. Eleftheroglou, D. Zarouchas, T. Loutas, R. C. Alderliesten, and R. Benedictus, “Online Remaining Fatigue Life Prognosis for Composite Materials Based on Strain Data and Stochastic Modeling,” *Key Engineering Materials*, vol. 713, pp. 34–37, 9 2016.

[19] J. W. Gillespie, “Damage Tolerance of Composite Structures: The Role of Interlaminar Fracture Mechanics,” *Journal of Offshore Mechanics and Arctic*, vol. 113, pp. 247–252, 1991.

[20] M. Ali, S. C. Joshi, and M. T. H. Sultan, “Palliatives for Low Velocity Impact Damage in Composite Laminates,” *Advances in Materials Science and Engineering*, vol. 2017, pp. 1–16, 2017.

[21] P. Robinson and G. A. O. Davies, “Impactor mass and specimen geometry effects in low velocity impact of laminated composites,” *Int. J. Impact Engng*, vol. 12, no. 2, pp. 189–207, 1992.

[22] A. Yigit and A. Christoforou, “On the impact between a rigid sphere and a thin composite laminate supported by a rigid substrate,” *Composite Structures*, vol. 30, pp. 169–177, 1 1995.

[23] V. P. W. Shim and L. M. Yang, “Characterization of the residual mechanical properties of woven fabric reinforced composites after low-velocity impact,” *International Journal of Mechanical Sciences*, vol. 47, pp. 647–665, 2005.

[24] S. Z. Shah, S. Karuppanan, P. S. Megat-Yusoff, and Z. Sajid, “Impact resistance and damage tolerance of fiber reinforced composites: A review,” *Composite Structures*, vol. 217, no. February, pp. 100–121, 2019.

[25] B. Whittingham, I. Marshall, T. Mitrevski, and R. Jones, “The response of composite structures with pre-stress subject to low velocity impact damage,” *Composite Structures*, vol. 66, pp. 685–698, 10 2004.

[26] T. Mitrevski, I. Marshall, R. Thomson, and R. Jones, “Low-velocity impacts on preloaded GFRP specimens with various impactor shapes,” *Composite Structures*, vol. 76, pp. 209–217, 11 2006.

[27] D. Schüler, “Effects of static preloads on the high velocity impact response of composite structures,” *DLR Deutsches Zentrum fur Luft- und Raumfahrt e.V. - Forschungsberichte*, vol. 2017-Janua, no. 40, pp. 1–127, 2017.

[28] D. Adams and A. K. Miller, “An analysis of the impact behavior of hybrid composite materials,” *Materials Science and Engineering*, vol. 19, pp. 245–260, 6 1975.

[29] W. Cantwell and J. Morton, “The impact resistance of composite materials — a review,” *Composites*, vol. 22, pp. 347–362, 9 1991.

[30] S. Abrate, *Impact Engineering of Composite Structures*, vol. 526 of *CISM International Centre for Mechanical Sciences*. Vienna: Springer Vienna, 2011.

[31] M. R. Wisnom, “The role of delamination in failure of fibre-reinforced composites,” *Philosophical Transactions of the Royal Society A: Mathematical, Physical and Engineering Sciences*, vol. 370, no. 1965, pp. 1850–1870, 2012.

[32] K.-W. Kang and J.-K. Kim, “Fatigue life prediction of impacted carbon/epoxy laminates under constant amplitude loading,” *Composites Part A: Applied Science and Manufacturing*, vol. 35, pp. 529–535, 5 2004.

[33] D. D. Symons and G. Davis, “Fatigue testing of impact-damaged T300/914 carbon-fibre-reinforced plastic,” *Composites Science and Technology*, vol. 60, pp. 379–389, 2 2000.

[34] S. R. Swanson, D. S. Cairns, M. E. Guyll, and D. Johnson, “Compression fatigue response for carbon fiber with conventional and toughened epoxy matrices with damage,” *Journal of Engineering Materials and Technology, Transactions of the ASME*, vol. 115, no. 1, pp. 116–121, 1993.

[35] J.-M. Koo, J.-H. Choi, and C.-S. Seok, “Evaluation for residual strength and fatigue characteristics after impact in CFRP composites,” *Composite Structures*, vol. 105, pp. 58–65, 2013.

[36] N. H. Tai, M. C. Yip, and J. L. Lin, “Effects of low-energy impact on the fatigue behavior of carbon/epoxy composites,” *Composites Science and Technology*, vol. 58, no. 1, pp. 1–8, 1998.

[37] H. Speckmann and R. Henrich, “Structural health monitoring (SHM) - overview on technologies under development,” in *16th world conference on NDT*, 2004.

[38] A. Güemes, A. Fernandez-Lopez, A. R. Pozo, and J. Sierra-Pérez, “Structural Health Monitoring for Advanced Composite Structures: A Review,” *Journal of Composites Science*, vol. 4, p. 13, 1 2020.

[39] D. M. Steinweg and M. Hornung, “Evaluating the Influence of SHM on Damage Tolerant Aircraft Structures Considering Fatigue,” in *ICAF 2019 – Structural Integrity in the Age of Additive Manufacturing*, vol. 2 of *Lecture Notes in Mechanical Engineering*, pp. 976–993, Cham: Springer International Publishing, 2020.

[40] R. M. Groves, *Inspection and monitoring of composite aircraft structures*, vol. 3. Elsevier Ltd., 2017.

[41] K. Worden, E. J. Cross, N. Dervilis, E. Papatheou, and I. Antoniadou, “Structural Health Monitoring: from Structures to Systems-of-Systems,” *IFAC-PapersOnLine*, vol. 48, pp. 1–17, 9 2015.

[42] N. Eleftheroglou, D. Zarouchas, T. Loutas, R. Alderliesten, and R. Benedictus, “Structural health monitoring data fusion for in-situ life prognosis of composite structures,” *Reliability Engineering & System Safety*, vol. 178, pp. 40–54, 10 2018.

[43] W. R. Broughton, M. R. Gower, M. J. Lodeiro, G. D. Pilkington, and R. M. Shaw, “Assessment of quasi-static and fatigue loaded notched GRP laminates using digital image correlation,” *Applied Mechanics and Materials*, vol. 24-25, pp. 407–412, 2010.

[44] B. Pan, “Digital image correlation for surface deformation measurement: historical developments, recent advances and future goals,” *Measurement Science and Technology*, vol. 29, p. 082001, 8 2018.

[45] M. Bourchak, I. Farrow, I. Bond, C. Rowland, and F. Menan, “Acoustic emission energy as a fatigue damage parameter for CFRP composites,” *International Journal of Fatigue*, vol. 29, pp. 457–470, 3 2007.

[46] M. Saeedifar, M. Ahmadi Najafabadi, K. Mohammadi, M. Fotouhi, H. Hosseini Toudeshky, and R. Mohammadi, “Acoustic Emission-Based Methodology to Evaluate Delamination Crack Growth Under Quasi-static and Fatigue Loading Conditions,” *Journal of Nondestructive Evaluation*, vol. 37, no. 1, pp. 1–13, 2018.

[47] S. Goutianos, “Acoustic emission characteristics of unidirectional glass/epoxy composites under mixed-mode fracture,” *SN Applied Sciences*, vol. 1, no. 5, p. 474, 2019.

[48] P. F. Liu, J. K. Chu, Y. L. Liu, and J. Y. Zheng, “A study on the failure mechanisms of carbon fiber/epoxy composite laminates using acoustic emission,” *Materials and Design*, vol. 37, pp. 228–235, 2012.

[49] M. Saeedifar, J. Mansvelder, R. Mohammadi, and D. Zarouchas, “Using passive and active acoustic methods for impact damage assessment of composite structures,” *Composite Structures*, vol. 226, 10 2019.

[50] R. Di Sante, “Fibre optic sensors for structural health monitoring of aircraft composite structures: Recent advances and applications,” 7 2015.

[51] W. Fan and P. Qiao, “Vibration-based damage identification methods: A review and comparative study,” 2011.

[52] N. Eleftheroglou, D. Zarouchas, and R. Benedictus, “An adaptive probabilistic data-driven methodology for prognosis of the fatigue life of composite structures,” *Composite Structures*, vol. 245, 2020.

[53] E. Eleftheroglou, D. S. Zarouchas, T. H. Loutas, and N. Eleftheroglou, “In-Situ Fatigue Damage Assessment of Carbon-Fibre Reinforced Polymer Structures Using Advanced Experimental Techniques,” in *ECCM17 - 17th European Conference on Composite Materials*, (Munich, Germany), 2016.

[54] C. Bouvet, B. Castanié, M. Bizeul, and J. J. Barrau, “Low velocity impact modelling in laminate composite panels with discrete interface elements,” *International Journal of Solids and Structures*, vol. 46, no. 14-15, pp. 2809–2821, 2009.